UNIVERSITY OF CAPE TOWN
IYUNIVESITHI YASEKAPA • UNIVERSITEIT VAN KAAPSTAD

Crushing Characteristics of Axially Stacked Square Tubes

Fabio Federico Piraino Ronchietto

November 2008

Thesis submitted in partial fulfilment of the requirements for
Master's Degree in Engineering

Blast Impact and Survivability Research Unit
Department of Mechanical Engineering
University of Cape Town

DECLARATION

I, Fabio Federico Ronchietto, declare that this dissertation is essentially my own work. It is being submitted in partial fulfillment of the requirements for Master of Science in Engineering degree at the University of Cape Town and has not been submitted in this or any other form for a degree at any other university.

Fabio Federico Ronchietto

November 2008

ABSTRACT

The crushing and energy absorption characteristics of thin-walled specimens consisting of single, welded and two axially stacked plate-divided mild steel square tubes were investigated by the performance of numerous quasi-static and dynamic axial crushing tests and FEM (finite element modeling). The simulation was carried out using the finite element package ABAQUS/*Explicit* 6.7.1. Lengths of the specimens ranged from 300mm to 1700mm encompassing the three main modes of buckling of square tube specimens; namely progressive, global bending and transition between the buckling modes.

Welded specimens comprised of two tubes of equal length axially stacked on each other and welded together around all four sides. Plate divided specimens consisted of two tubes of equal length axially stacked with a mild steel plate in between them. The rigid plate, which was assumed to be rigid, had a thickness of 10mm and acted as an elastic medium for energy to be transferred from the top tube to the bottom tube during quasi-static and dynamic axial loading. All tubes had square cross-sections of 50mm×50mm and wall thicknesses of 1.6mm.

The aims of this investigation were to analyse the buckling modes of welded and plate-divided specimens and to determine whether they were as efficient as geometrically similar single tubes are as energy absorbers.

Quasi-static results showed that for single tubes global bending first occurred in single tubes at 800mm (critical length-to-width aspect ratio of 16) while for welded and plate-divided tube specimens, global bending occurred at 750mm (critical length-to-width aspect ratio of 15). No transition buckling was observed. Force-displacement curves revealed that welded tubes behaved very similarly to single tubes in that they exhibited one peak load. In plate-divided specimens, however, two peak loads were observed and in turn this slightly increased the mean load experienced by the specimens compared to single and welded tube specimens.

Dynamic tests were performed with a drop mass of 340kg and a drop height of 3.26m, corresponding to an impact velocity of 8m/s. Transition buckling occurred in single and welded tube specimens but not in plate-divided specimens. Only one welded tube exhibited global bending. Plate-divided specimens performed the best as they all buckled in a progressive manner. However, two plate-divided specimens displayed fly out failure after initial progressive buckling. Fly-out failures are characterised by the top tube and plate slipping off the bottom tube during impact and were common occurrences in prior tests on short plate-divided specimens.

Crushed distances were similar in all three configurations but geometric efficiency and specific energy decreased linearly with increasing specimen length. This was expected since geometric efficiency and specific energy are inversely proportional to specimen length and specimen mass, respectively.

A numerical analysis that simulated dynamic testing was carried out using the finite element package ABAQUS/*Explicit* 6.7.1 which incorporated tube geometry, material properties and material effects such as strain hardening and strain rate sensitivity. The predicted time responses and buckling modes from finite element simulations were very accurate as they closely matched the behaviour of experimental tests and results obtained from high-speed footage of dynamic crush tests. The simulations succeeded in predicting symmetric and extensional progressive buckling as well as transition buckling in longer tubes. Furthermore it also predicted fly-out failures in short plate-divided specimens.

Conclusions drawn were that welded specimens displayed very similar crushing behaviour to single tubes but that the weld created geometric instability in some cases which led to undesirable buckling modes. In plate-divided specimens the frictional forces at the tubes and plate contact interfaces were not enough to overcome slight lateral movement of the plate and upper tube. This lateral degree of freedom in plate-divided specimens hindered the onset of transition or global bending and allowed progressive buckling to take place.

It is recommended, therefore, that further experiments should be carried out with tubes of different width-to-thickness ratios to confirm or disprove existing empirical formulas describing transition buckling behaviour in square tubes. Furthermore, replacing single tubes that buckle in the global bending region with two axially stacked plate-divided tube specimens should be investigated. The finite element model should be altered for welded tube simulations to take into account the slightly different material properties associated with the HAZ (Heat Affected Zone) and weld metal. Transition and global bending should be further investigated in finite element simulations to ascertain whether these buckling modes emerge on their own accord without the assistance of thermal or geometric triggers.

ACKNOWLEDGEMENTS

I would like to thank the following people that contributed throughout the course of my thesis:

My supervisor, Professor G.N. Nurick, for giving me the opportunity to do my thesis at BISRU and for his sincere concern and regular checking up on my progress.

Dr. S. Chung Kim Yuen for devoting many hours of his time in assisting me with testing and for his advice with regards to my thesis.

G. Newins and the UCT Mechanical Engineering Workshop staff for their patience and hard work in producing my specimens from many metres of tubing.

Mrs. P. Park-Ross for allowing me to use the Zwick testing machine in UCT's Materials Engineering Laboratory.

Mr. V. Balden and Dr. D. Karagiozova for their advice with regards to finite element modeling.

My family, friends and colleagues at BISRU for their support, motivation and advice.

.

TABLE OF CONTENTS

LIST OF FIGURES

Chapter 2

Chapter 3

Chapter 4

Chapter 5

Chapter 6

Chapter 7

LIST OF TABLES

Chapter 3

Chapter 4

Chapter 5

Chapter 6

Chapter 7

LIST OF SYMBOLS

Symbol	Description
A_g	Cross-sectional area of gauge in tensile test specimen
C	Mean width of square tube
D	Cowper Symonds coefficient
E	Young's modulus or Modulus of elasticity
E_{pd}	Plastic deformation energy (Internal energy)
$E_{potential}$	Potential energy
$E_{kinetic}$	Kinetic energy
H	Mean wall thickness of square tube
L_{bottom}	Unclamped length of bottom tube in two-tube specimen
L_g	Gauge length of tensile test specimen
L_{top}	Length of top tube in two-tube specimen
L	Total length of two-tube specimen
M	Drop mass in dynamic tests
M_0	Plastic moment
P	Axial load in tensile tests
P_m	Theoretical prediction of mean crushing load
P^d_m	Average value of dynamic crushing load
P^s_m	Average value of static crushing load
S_e	Specific energy
V	Impact velocity of striking mass
chs	Cross-head speed
e_G	Geometric efficiency
h	Drop height in dynamic tests
m	Mass of specimen
q	Cowper-Symonds exponent
t	Time
t_g	Gauge thickness of tensile test specimen
w_g	Gauge width of tensile test specimen

Symbol	Description
δ	Total axial displacement of a specimen
ε	Engineering strain
ε_{true}	True strain
$\dot{\varepsilon}$	Mean strain rate during crushing
σ_f	Stress at fracture of tensile test specimen
σ^d_y	Dynamic tensile yield stress
σ_y	Static tensile stress or Engineering stress
σ_0	Mean value of plastic flow stress
σ_{uts}	Ultimate tensile stress
σ_{true}	True stress

1. INTRODUCTION

Thousands of lives are lost every year around the world as a result of vehicle collisions [1]. By designing lighter and better energy absorbing devices for various transportation systems, many lives can be saved. Such devices are very important in increasing vehicle crashworthiness without increasing the weight of the vehicle. The focus of structural crashworthiness seeks to improve the collision resistance of transportation systems by sacrificing the vehicle structure and protecting its passengers. This limits the deceleration, absorbs the impact forces and maintains structural integrity thereby protecting passengers and cargo [2, 3].

The subject of crushing of square tubes has been investigated thoroughly by numerous authors over the past few years [2-10]. A particular point of interest regarding tube crushing is the transition from initial global bending to progressive buckling in tubes. Progressive buckling is the most efficient mode of collapse and is associated with the formation of lobes which usually develop from one end of the tube. Global bending, on the other hand, is an inefficient mode of collapse and is characterised by deformation which usually occurs half-way along the length of a tube during crushing. Only a few authors have investigated the transition from initial global bending to progressive buckling [11-15]. Abramowicz and Jones [12] explored the critical parameters which govern the transition from global bending to progressive collapse for square mild steel tubes. Jensen *et al.* [13] used LS-DYNA to perform numerical simulations on order to investigate the transition between progressive and global buckling in square aluminium tubes.

An extensive review of literature revealed that much work has been published on the axial crushing of steel and aluminium sections, particularly in the case of square and circular cross sections. Prior tests have been performed on two thin-walled square tubes stacked axially in series with lengths in the progressive buckling region to research the potential energy absorption and peak force minimising effect. These tubes were balanced on each other with a mild steel plate in between them. The plate was assumed to be rigid and acted as a medium for energy to be transferred from the

one tube to the other during axial crushing. However, while some work has been carried out on multiple tube energy absorbers, no work has been published on the crushing of two axially stacked thin-walled square tubes.

This dissertation reports on the results of an experimental and numerical investigation into the response of square mild-steel tube specimens subjected to quasi-static and dynamic axial loads. The specimens consist of single tubes, two tubes welded in series and two axially stacked tubes whose individual lengths are in the progressive or transition buckling region and whose combined equivalent lengths are in the transition or global bending buckling regions. Furthermore, this research aims to compare energy absorption devices of this nature with single tubes to determine which configuration is more efficient as an energy absorber. The finite element package ABAQUS/*Explicit* 6.7.1 is used to simulate the buckling modes and deformation of the specimens and the numerical simulations are compared with the experimental results.

A number of objectives have been set for this dissertation, namely to:

- perform a literature review on work that has been published concerning the axial crushing of square tubes.
- create different tube configurations using single tubes, two tubes welded in series and two axially stacked tubes.
- perform quasi-static and dynamic axial crushing tests on the above-mentioned configurations, so as to investigate their energy absorption and crushing characteristics.
- analyse the results and compare the different configurations to each other.
- perform finite element modelling to the response of specimens and compare the simulations to experimental results.
- draw conclusions and make recommendations based on the results and findings.

The dissertation is structured as follows:

- Chapter 2 summarises pertinent information gathered from current literature.
- Chapter 3 describes the experimental procedure used in the tests.
- Chapter 4 presents the results from the tensile, quasi-static and dynamic tests.
- Chapter 5 analyses the results and discusses interesting points.
- Chapter 6 presents the numerical modelling process.
- Chapter 7 analyses numerical modelling results and compares them to experimental results.
- Chapter 8 presents conclusions and,
- Chapter 9 presents recommendations.

2. LITERATURE REVIEW

Road incidents result in the deaths of an estimated 1.2 million people worldwide each year, and injure about forty times this number [1]. In South Africa there are over 500000 motor vehicle crashes a year.

Of these, 28000 are fatal or lead to serious injury. In 2006 in South Africa there were 15396 fatalities, costing the South African economy billions of Rands per year. In the USA there were 42884 fatalities in 2003 [1]. These figures are rising every year. There are a number of factors that lead to vehicle crashes including pedestrian fatalities which is the biggest contributor to road deaths in South Africa [1]. Many vehicles involved in accidents are old and their structural crashworthiness is inferior compared to modern day vehicles. Unfortunately, fatalities due to crashes will always occur but good crashworthiness design can significantly decrease the loss of life on our roads.

2.1 Structural Crashworthiness and Vehicle Safety

Jones [2] defines *structural crashworthiness* as "an investigation into the impact performance of a structure when it collides with another object." Structural crashworthiness characteristics of a system need to be studied in order to determine the forces during a collision. This is needed to assess the damage to structures and the survivability of passengers in vehicles. Structural crashworthiness aims to improve the collision resistance of transportation vehicles such as cars, trains and aircraft, by sacrificing the structure to absorb the collision energy thereby protecting the passengers and/ or cargo within the vehicle [3]. For passenger safety it is required to limit the deceleration and forces so that they may survive specific accident scenarios. It is also required in some cases that structural systems absorb the energy but maintain integrity in order to prevent any loss of hazardous materials. In almost all cases the impact energy involved in accidents are very much larger than the maximum amount of elastic energy that could possibly be absorbed by the structure.

Jones [3] comments that "over the past few years, the field of structural crashworthiness has received much attention because of the increased public awareness of safety and environmental issues, leading to increased pressure on designers of energy absorption systems." Obviously, it is important to understand the various phenomena involved in these highly non-linear dynamic structural problems, and for these reasons investigations have been reported over the years on simplified models that capture the essential behavioural characteristics. Even with the highly sophisticated numerical schemes used today, such as FEM, simple models are extremely important for the interpretation of data and for preliminary design purposes.

The new R56 MINI Cooper as shown in Figure 2.1a has recently gone through the Euro NCAP crash test and managed to score a 5 Star crash test rating, scoring 13 out of 16 points for deformation behaviour in a head-on collision, and 16 from 18 points in the side-on and pillar collision [9]. In 2006, a full scale test was conducted by the US Department of Transportation on a passenger rail train retrofitted with newly developed cab and coach car crush zone designs [17]. This train-to-train crash test was conducted as part of a larger testing program to establish the degree of enhanced performance of alternative design strategies for passenger rail crashworthiness. The alternative design strategy is characterised by collision energy being absorbed in defined unoccupied locations throughout the train in a controlled progressive manner. The energy absorbing mechanism included reusable and expendable energy absorbing devices as illustrated in Figure 2.1b. These two tests substantiate the key role that structural crashworthiness plays in the consideration of the final design of vehicles, especially in the transportation industry.

(a)

(b)

Figure 2.1: (a) Mini-Cooper crash test [9] (b) Train cab car crush zone [17].

Shin *et al.* [4] report that in the front structure of vehicles, upper and lower side rails are the main energy absorbers when a vehicle crashes. Figure 2.2 shows the composite front structure suggested by GM, Ford and Chrysler. The front structure that supports engine mount and suspension is composed of upper and lower side rails and apron. Generally, the cross-section shape of the side rail is square, rectangular, or hourglass tube. The four side rails can absorb 70% of the impact energy through the progressive plastic deformation of metals when the vehicle crashes.

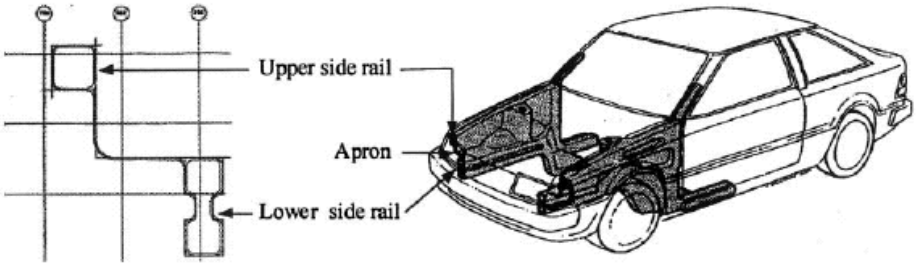

Figure 2.2: Composite front structure of a vehicle [4].

2.2 Energy Absorption Systems

2.2.1 Introduction

Alghamdi [18] defines an energy absorber as "a system that converts, totally or partially, kinetic energy into another form of energy." Metallic energy absorbers dissipate energy irreversibly through plastic deformation. When designing a collapsible energy absorber, one aims at absorbing the majority of the kinetic energy of impact within the device itself in an irreversible manner, thus ensuring that human injuries and equipment damages are minimal. The conversion of the kinetic energy into plastic deformation depends, among other factors, on the magnitude and method of application of loads, transmission rates, deformation or displacement patterns and material properties.

Jones [3] comments that energy absorption systems are an important part of many practical engineering systems. They are used extensively during impact events to absorb and dissipate energy due to friction, fracture, shear, bending, tension, torsion,

crushing etc. These energy absorption systems are primarily made of metals although wood, plastic and other materials are also used. They are classified as reusable, rechargeable or expendable. An example of a reusable device would be a hydraulic damper while a rechargeable device would be one in which the energy- absorbing component is replaced in a fixed container. An expendable device is one such as a vehicles body being crushed during a collision.

2.2.2 Metallic Energy Absorbers

Many energy-absorbing devices have been tried and tested by various researchers. There is a large variety of these devices in terms of materials and geometry. Shin *et al.* [4] investigated the absorption capability of axial crush and bending collapse of aluminium/GFRP. Kim *et al.* [5] investigated the compressive deformation behaviour under dynamic loading to evaluate experimentally impact-absorption energies of extruded aluminium tubes for space frame design. Space frame has recently been developed and widely used in designing the structure of car bodies. The production of space frame is based on plastic deformation processing, such as extrusion, bending, and die-casting and involves the use of aluminium alloys. Space frame design is characterised by weight saving, fuel consumption and impact durability. Starbuck et al. [19] analysed and designed adhesively bonded automotive composite structures to sustain axial, off-axis, and lateral crash/impact loads.

Numerous papers have been published on the axial crushing of steel sections. Tarigopula et al. [6] report that there is an increased interest in thin-walled high-strength steel sections in the ongoing search for lighter and more efficient energy absorbing components. The energy absorption characteristics of such components are very important in improving the vehicle crashworthiness without increasing the body weight. One of the aims of research is the desire to design cross-sections that deform in a regular controlled manner, and also cost-to-weight effectiveness. One of their observations is that steel top-hat sections absorb more energy than square sections. White and Jones [20, 21] explored the collapse characteristics for top-hat and double-hat sections made of mild steel sections when subjected to axial crushing. They found that top-hat structures allow a more regular, progressive collapse compared with the

double-hat structures, and are thus considered better crashworthy devices. Authors such as Kim et. al [22] and Morris et. al. [23] investigated the ability of steel tubular structures with rectangular [22] and circular and oval [23] cross-sections to absorb energy when subjected to lateral loading. Such structures may find applications when subjected to compressive loads under impact with the aim of bringing a moving mass to a controlled stop, such as in the case of crash barriers.

2.2.3 Performance of Energy Absorbers

There are many ways of specifying an impact energy absorber through a number of dimensionless collapse efficiency parameters. Jones [2] and Arnold et al. [15] define **Specific Energy (S_e)** as the energy absorbed per unit mass:

$$S_e = \frac{E_p}{m} \tag{2.1}$$

where E_p is the total energy absorbed and m is the total mass of the energy-absorbing device.

Another measure is the **Volumetric Efficiency (V_e)** [2]**,**

$$V_e = \frac{V_u}{V_T} \tag{2.2}$$

where V_u is the volume of the energy absorbing part of a device and V_T is the total volume.

Load Efficiency (e_L) or force efficiency [2 and 15] is a measure of load fluctuations that occur during the crushing of a structure and is given by:

$$e_L = \frac{P_m}{P_{\max}} \tag{2.3}$$

where P_m is the mean load applied to the absorber and P_{max} is the maximum load applied to the absorber.

Geometric Efficiency (e_G) [15] or stroke efficiency [2] is a measure of how well an absorber is compressed. It is the ratio of crushed distance to original length. The geometric efficiency parameter is dependent on the initial kinetic energy. Geometric efficiency is given by:

$$e_G = \frac{\delta}{L} \tag{2.4}$$

where δ is the total amount of axial crushing and L is the original length of the absorber.

An ideal absorber is defined as one that maintains the maximum allowable retarding force throughout the stroke, apart from elastic loading and unloading effects. However, a designer must often decide between factors such as cost, volume, stroke, weight and deceleration. Most importantly, an absorber must be reliable and adaptable to be able to absorb a dynamic load that strikes at a random position [2].

The energy absorbed by a thin-walled tube with a square cross-section, which is subjected to either static or dynamic axial crushing forces, is given by

$$E_p = P_m \times \delta \tag{2.5}$$

where δ is the total amount of axial crushing and P_m is the mean axial static or dynamic crushing force. Thus the specific energy according to equation (2.1) is

$$S_e = \frac{P_m \delta}{4CHL\rho} \tag{2.6}$$

where C is the width of one of the four sides of a square tube, H is the wall thickness, L is the length of the tube and ρ is the density of the material as shown in Figure 2.3.

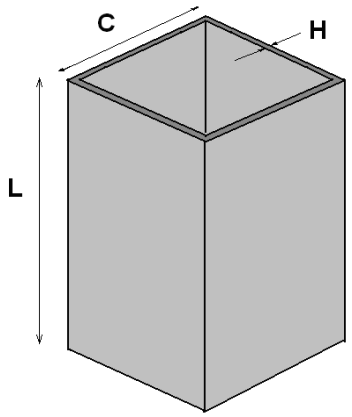

Figure 2.3: Dimensions of a square tube.

2.3 Buckling Modes of Thin-Walled Tubes

Experiments conducted on the axial collapse of thin-walled tubes under static and dynamic axial loading have resulted in the characterisation of three main buckling modes. The mode in which a tube buckles under axial load depends on a variety of factors such as cross-sectional geometry, tube length, material properties and loading conditions.

2.3.1 Global Bending

Global bending occurs in relatively long, slender tubes and is characterised by large inelastic global bending. Global bending is distinct in that it is typified by the formation of a single plastic hinge in the tube, usually occurring half-way along the length of a tube as shown in Figure 2.4a. The force-displacement curve of the tube will resemble that in Figure 2.4b. The area under the curve is the energy dissipated. This buckling mode is highly undesirable since it is associated with low plastic deformation and inefficient energy dissipation.

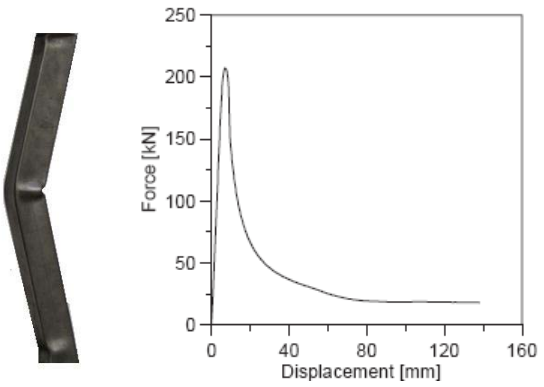

(a) **(b)**

Figure 2.4: (a) Mild steel tube after global bending and (b) typical force-displacement graph for global bending [9].

2.3.2 Progressive Buckling

Progressive buckling is typically associated with the formation of lobes during crushing of relatively short tubes as shown in Figure 2.5a. The progressive buckling mode is the most efficient energy absorbing form of collapse in tubes because most of the material is utilised in energy absorption through plastic work [17]. Under progressive buckling, the load decreases to a local minimum and then begins to increase again until the creation of another fold. This process repeats itself as the load oscillates about the mean crush load. A typical force-displacement curve for a progressive buckling tube is shown in Figure 2.5b. Each pair of peaks and valleys of the force-displacement curve is associated with a lobe in the deformed tube.

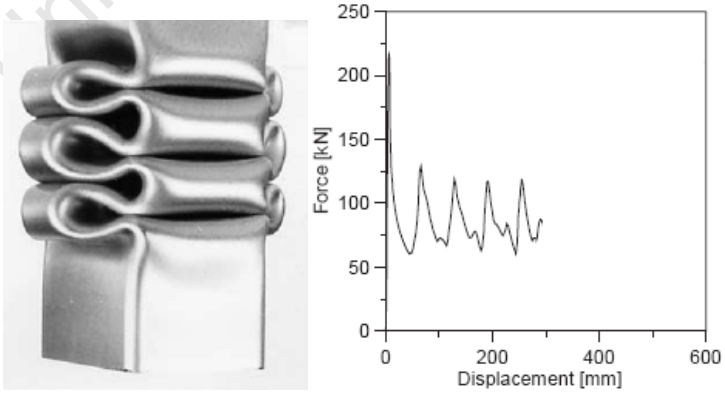

(a) **(b)**

Figure 2.5: (a) Aluminium tube after progressive buckling [24] and (b) typical force-displacement graph for progressive buckling [9].

Progressive buckling of thin-walled tubes is an uncomplicated yet practical energy absorber for engineering systems. Comprehensive theoretical descriptions of the buckling process have been published by Jones [2] and Abramowicz and Jones [7]. Two basic collapse elements as shown in Figure 2.6a and b may be used to examine the static progressive buckling of square tubes with a mean width *C* and a mean wall thickness *H*. These basic collapse elements have also been used to study the dynamic progressive buckling of square tubes. Abramowicz and Jones [7] predicted four different progressive buckling modes. The modes are:

1. **Symmetric crushing mode** is idealised with four type I collapse elements in Figure 2.6a for each layer of lobes. This crushing mode is predicted to form in thin square tubes with C/H > 40.8, approximately.

2. **Asymmetric mixed mode A** consists of six type I and two type II collapse elements shown in Figure 2.6. In other words it is a combination of symmetric layers and layers with three lobes moving outwards and one inwards.

3. **Asymmetric mixed mode B** progressive buckling is idealised as two adjacent layers of lobes having seven of the basic elements of Type I and one of the elements in Type II. This type of crushing is predicted to form within the range $7.5 \leq C/H \leq 40.8$. The difference between the theoretical crushing force associated with a symmetric mode and an asymmetric mode B is small so that either may develop in an actual square tube specimen that has slight imperfections.

4. **Extensional mode** of crushing is idealised with four type II collapse elements in Figure 2.6b. This type of progressive buckling is predicted to form in thick square tubes with C/H < 7.5, approximately. All the lobes within a layer move outwards.

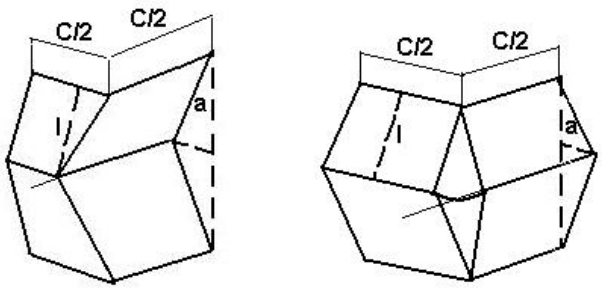

(a) **(b)**

Figure 2.6: Basic collapse elements (a) Type I. (b) Type II [7]

2.3.2.1 Static axial crushing [2]

The theoretical analysis for symmetric crushing is sufficient to predict the behaviour for most thin-walled tubes and is also acceptable for those with thick walls. The internal energy consumed by four of the basic collapse elements of Type 1 in forming one complete layer of lobes (symmetric collapse mode) is equated to the external work done by the mean axial crushing force and minimised to predict

$$P_m / M_0 = 38.12\left(C/H\right)^{1/3} \tag{2.7}$$

with

$$l/H = 0.99\left(C/H\right)^{2/3} \tag{2.8}$$

where

$$M_0 = \sigma_0 H^2/4 \tag{2.9}$$

where *2l* is the initial axial separation between the locations of the plastic hinges at the top and the bottom edges of a basic folding element as indicated in Figure 2.6a. Historically, the Tresca yield condition is used for M_0 in equation 2.9.

However, the lobes do not flatten completely during crushing as indicated in the theoretical approach leading to equation (2.7), which uses the basic collapse elements. The effective crushing distance for the symmetric crushing of a square tube is

$$\delta_e / 2l = 0.73 \tag{2.10a}$$

while for the asymmetric collapse modes it is

$$\delta_e / 2l = 0.77 \tag{2.10b}$$

Equations 2.7 and 2.10a can be combined to get

$$P_m / M_0 = 52.22 \left(C / H \right)^{1/3} \tag{2.11a}$$

This is known as the dimensionless mean crushing load. For square tubes with C = 50mm and H = 1.6mm, the dimensionless mean crushing load has a value of 164.5. For a yield stress of 328MPa, a value for the mean load P_m of 33.7kN would be obtained. Similarly for asymmetric mixed collapse modes A and B, respectively, the equivalent equations are:

$$P_m / M_0 = 42.92 \left(C / H \right)^{1/3} + 3.17 \left(C / H \right)^{2/3} + 2.04 \tag{2.11b}$$

and

$$P_m / M_0 = 45.90 \left(C / H \right)^{1/3} + 1.75 \left(C / H \right)^{2/3} + 1.02 \tag{2.11c}$$

2.3.2.2 Dynamic axial crushing

The dynamic progressive buckling of a square tube is idealised as a quasi-static response [2]. Equations 2.11a, b and c predict the dynamic axial force of a square tube made from strain-rate-insensitive material. If a square tube is made of a strain-rate-sensitive material, then

$$P_m / M_0 = 52.22 \left(C/H\right)^{1/3} \left\{1 + \left(\dot{\varepsilon}/D\right)^{1/q}\right\} \tag{2.12}$$

for the symmetric mode of collapse.

Material strain rate sensitivity is important in the theoretical analysis for mild steel tubes impacted axially [7]. The Cowper-Symonds uniaxial constitutive equation is given by:

$$\sigma_y^d / \sigma_y = 1 + \left(\dot{\varepsilon}/D\right)^{1/q} \tag{2.13}$$

Until recently there has been a lack of adequate experimental data on the dynamic plastic behaviour of materials with large strains which are found in the dynamic progressive crushing of square tubes. Various authors have obtained different values for D and q but the values obtained by Marais et al. [25] were deemed suitable for this investigation. Marais et al. [25] obtained constants of $D = 844\text{s}^{-1}$ and $q = 2.207$ for mild steel in their experimental observations. Because of the complex deformation patterns of a square tube, it is difficult to accurately estimate the strain rate [2]. However, it can be estimated by:

$$\dot{\varepsilon} = 0.33 \times V/C \tag{2.14a}$$

for the symmetric collapse mode,

$$\dot{\varepsilon} = 0.44 \times V/C \tag{2.14b}$$

for the asymmetric mixed collapse mode A and

$$\dot{\varepsilon} = 0.39 \times V/C \tag{2.14b}$$

for the asymmetric mixed collapse mode B [7].

This gives the mean strain rate in the toroidal corner regions of the idealised deformation pattern. Equation (2.12) can be rewritten as

$$P_m/M_0 = 52.22\left(C/H\right)^{1/3}\left\{1+\left(0.33\,V/CD\right)^{1/q}\right\} \tag{2.15a}$$

Similarly, for the asymmetric collapse modes A and B, respectively, the equivalent equations are:

$$P_m/M_0 = \left\{42.92\left(C/H\right)^{1/3} + 3.17\left(C/H\right)^{2/3} + 2.04\right\}\left\{1+\left(0.44\,V/CD\right)^{1/q}\right\} \tag{2.15b}$$

and

$$P_m/M_0 = \left\{45.90\left(C/H\right)^{1/3} + 1.75\left(C/H\right)^{2/3} + 1.02\right\}\left\{1+\left(0.39\,V/CD\right)^{1/q}\right\} \tag{2.15c}$$

The theoretical predictions of equations 2.11a, b, c and 2.15a, b, c give the axial crushing force ratio for symmetric collapse mode and asymmetric mixed collapse modes A and B, respectively:

$$P_m^d/P_m^s = 1+\left(0.33\,V/CD\right)^{1/q} \tag{2.16a}$$

$$P_m^d/P_m^s = 1+\left(0.44\,V/CD\right)^{1/q} \tag{2.16b}$$

and

$$P_m^d/P_m^s = 1+\left(0.39\,V/CD\right)^{1/q} \tag{2.16c}$$

where P^d_m and P^s_m are the dynamic and static progressive buckling forces respectively. For an impact velocity V of 8m/s, the axial crushing force ratio has a

value of 1.28 for the symmetric collapse mode, 1.32 for the asymmetric mixed collapse mode A and 1.3 for the asymmetric mixed collapse mode B.

2.3.3 Transition Buckling

In the context of tube crushing, an area of particular interest which is currently being researched is the transition from Euler or global bending to Progressive buckling. Andrews *et al.* [11] pioneered the study of transition buckling. In their study they performed experimental tests and were able to create a classification chart that describes the relationship between tube length and thickness to the buckling modes for cylindrical aluminium tubes. They established that global bending is more likely to occur in thick tubes with large slenderness ratios. Abramowicz and Jones [12] also investigated this topic with their experimental study on static and dynamic axial crushing of square and circular steel tubes which buckled mostly in the plastic range. Their results varied considerably from those of Andrews et al. [11] since they used steel instead of aluminium. Steel is strain-rate sensitive and experiences strain hardening while aluminium is not strain-rate sensitive. Figure 2.7 shows the transition classification graph for square tubes under quasi-static loading. The transition classification graphs obtained for square tubes under quasi-static and dynamic axial loading are compared in Figure 2.8a and b, respectively.

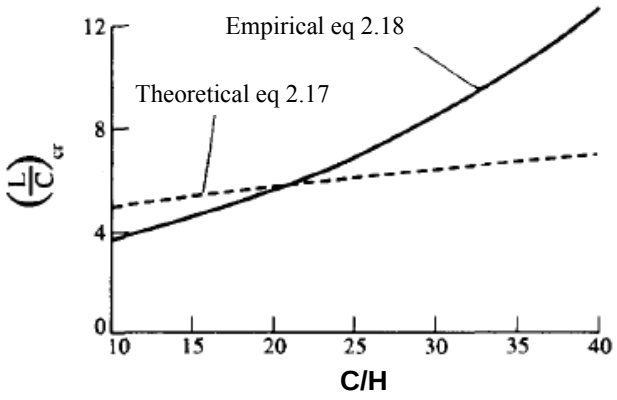

Figure 2.7: Lines separating the global plastic bending and local buckling modes in square columns subjected to quasi-static axial loading [12].

Eq. (2.17) and (2.18) in Figure 2.7 refer to the theoretical and empirically derived formulae, respectively, for the critical lengths under quasi-static loading and are given by

$$\left(\frac{L}{C}\right)_{cr} = 2\frac{\left(\frac{C}{H}\right)^{1/3}}{1-2.88\left(\frac{H}{C}\right)^{4/3}} \qquad [12] \qquad (2.17)$$

and

$$\left(\frac{L}{C}\right)_{cr} = 2.482e^{\left(0.0409\frac{C}{H}\right)} \qquad [12] \qquad (2.18)$$

where L and C are the length and width of the tube respectively, and H is the wall thickness of the tube.

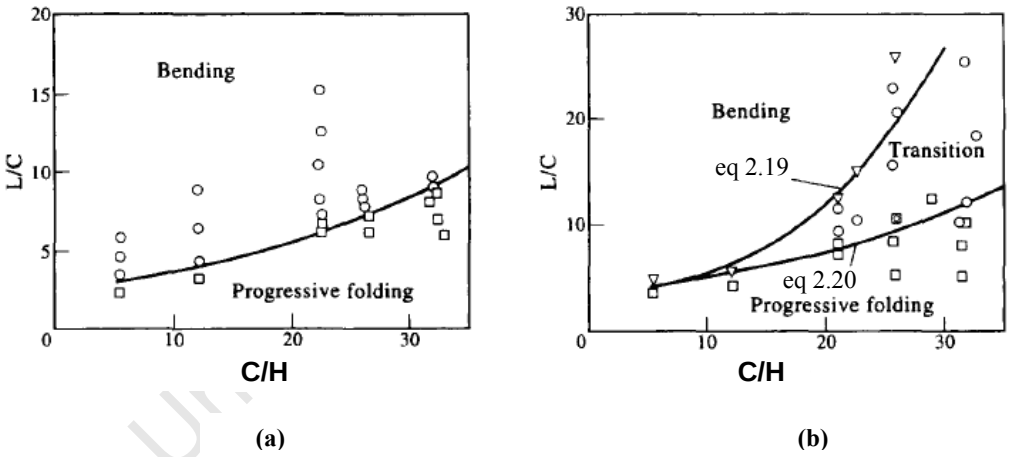

(a) (b)

Figure 2.8: Deformation maps for square columns subjected to (a) quasi-static axial loading with data points for □ Progressive buckling; ○ global bending and (b) dynamic axial loading with data points for: □ Progressive buckling; ○ Transition from progressive to global bending; ▽ global bending. [12].

Eq. (2.19) and (2.20) in Figure 2.8b refer to empirically derived formulae for the critical lengths under dynamic loading and are given by

$$\left(\frac{L}{C}\right)_{cr} = 2.453e^{\left(0.08\frac{C}{H}\right)} \qquad [12] \qquad (2.19)$$

and

$$\left(\frac{L}{C}\right)_{cr} = 3.423e^{\left(0.04\frac{C}{H}\right)} \qquad [12] \qquad (2.20)$$

Abramowicz and Jones [12] found that in general the transition from progressive to global bending for a given thickness, given by the value $(L/C)_{cr}$ was larger under dynamic loading than for quasi-static loading. They also found a third distinct mode under dynamic loading whereby the tube would begin to buckle progressively and then continue to bend globally or vice versa.

Jensen et al. [13] also studied buckling transition but in aluminium tubes with various cross-sections and impact velocities. They validated numerical models against experimental tests and found good correlation in the progressive buckling mode between the two, as shown in Figure 2.9a. Their numerical simulations were capable of giving a fairly accurate prediction of the collapse mode encountered in experimental tests such as transition buckling shown in Figure 2.9b. They found that at quasi-static and impact velocities up to 13m/s the critical global slenderness $(L/C)_{cr}$ is an increasing function of the cross-sectional slenderness (C/H). The same function is found to be decreasing however for impact velocities of 20m/s. Karagiozova and Alves [14, 15] validated this behaviour experimentally, numerically and theoretically. The study by Jensen et al. [13] emphasised the importance of material properties and inertia effects when characterizing buckling transition. They found that materials with high yield stress and low strain hardening perform better than materials with a low yield stress and high strain hardening.

Figure 2.9: Finite element and experimental specimens showing (a) progressive buckling at V = 13m/s, L = 1120mm, H = 2.5mm and (b) transition buckling at V = 13m/s, L = 1520mm, H = 2mm [13].

2.4 Additional Numerical Studies on Square Tubes

Mathematical studies on metal tubes have been performed by various authors through Finite Element Modeling. Filippov et al. [26] studied the localized vibrations of a thin-walled square tube with a free end and derived equations for the natural frequencies of square tubes. Karagiozova [27] analysed the influence of the transient deformation process on the initiation of buckling in square tubes under axial impact by obtaining the speeds of stress waves that can propagate in an elastic-plastic medium with isotropic linear strain hardening in a plane stress state. She found that the material hardening properties have a strong effect on the speed of the slow plastic wave, while the shear stress affects the speeds of both the fast and slow plastic waves. Further studies by Karagiozova and Jones [28] looked at dynamic elastic-plastic buckling of thin-walled square tubes from the viewpoint of elastic-plastic stress wave propagation, which originates from an axial impact loading. They found that the initial buckling pattern of a square tube depends on both the velocity and mass of a striker. Figure 2.10 shows finite element models of square tube specimens impacted at different velocities by different masses, subjected to 600J axial impact.

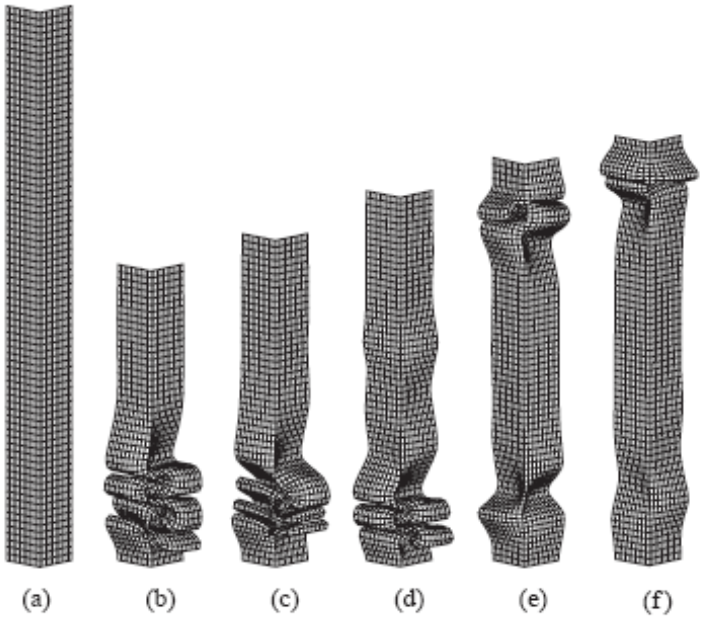

Figure 2.10: Numerical predictions of square tubes subjected to 600J axial impact: (a) initial; (b) V = 14.84m/s; (c) V = 25.34m/s; (d) V = 40.0m/s; (e) V = 64.32m/s; (f) 98.27m/s [28].

2.5 Imperfections, Fillers and Multiple Tubes as Energy Absorbers

2.5.1 Geometric Imperfections

Geometric changes to improve the energy absorption characteristics of tubular structures include additions such as fillers and imperfections. Many papers have been published by a variety of authors on the effects of imperfections on the buckling effect of square tubes. These imperfections include prebuckle [29], corner and dished indentations [30 and 31], cutouts [32], triggered dents [33-35] and blast dents [36]. An overview of the energy absorbing characteristics of tubular structures with geometric and material modifications has been presented by Chung Kim Yuen and Nurick [10]. Welds in tubes can be considered geometric and material imperfections as they essentially thicken a section of tube and change the material properties of the metal. Section 2.5.3 describes weld properties in more detail.

2.5.2 Fillers in Tubes and Multiple Tubes

In the case of fillers the investigations are focused on a single tube with filler such as aluminium foam [37 and 38] or wood [39]. Seitzberger et al. [37] investigated the effects of different tube and filler arrangements on the crushing behaviour of axially compressed tubular crush elements, including two tubes in parallel with aluminium foam, as shown in Figure 2.11.

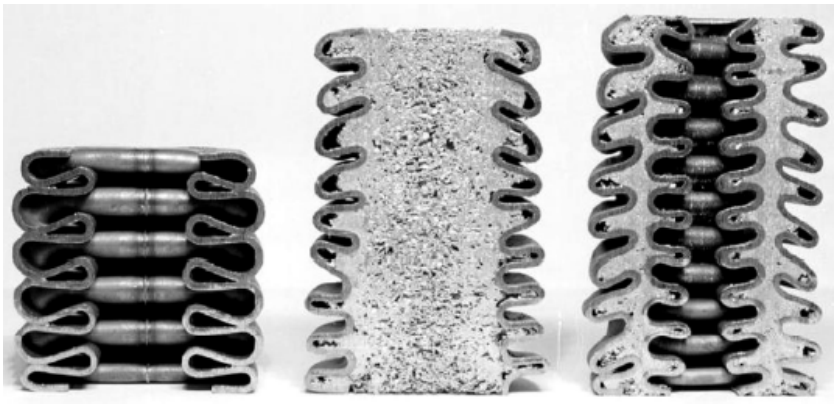

Figure 2.11: Square tube specimens including aluminium foam filled specimen and two tubes in parallel with foam in between them [37].

Other authors that have investigated the response of more than one tubular structure subjected to an axial load include Theobald and Nurick [40] who investigated the efficiency of multiple thin-walled tubes in parallel placed between steel plates and subjected to blast loading. A finite element model showing quarter symmetry of their setup is shown in Figure 2.12. No published work exists on plates between axially stacked tubes.

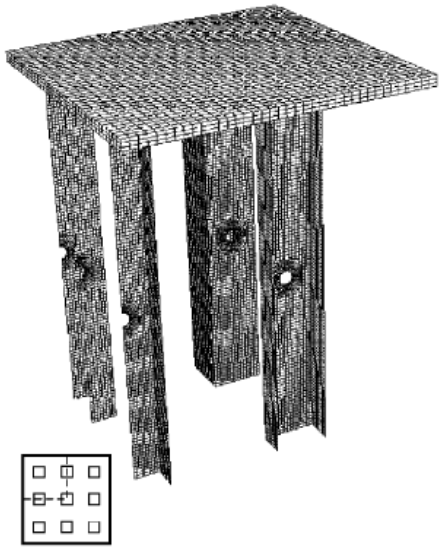

Figure 2.12: Finite element model showing quarter symmetry of square tubes in parallel including steel plate subjected to blast loading [40].

2.5.3 Weld Properties

In general the mechanical response of a welded joint depends on the variance in material properties between the base metal (BM), weld metal (WM) and heat affected zone (HAZ). While the BM is the part of the parent material not affected by the heat input, the WM and HAZ result from the welding process [41]. Numerous tests and methods, including tensile testing and micro-hardness testing, have been performed (with varying results) to characterise weld profiles. Rodrigues et al. [41] performed tensile tests and numerical modelling thereof of welded joints and found that in high strength steel weld subjected to slow cooling rates, the yield stress in the relatively soft HAZ can fall below the BM value and is thus the most likely area for a specimen to fail [41]. The dimensions of the weld zones also have an effect on where a tensile specimen deforms first. Figure 2.13 shows the various weld zones and the resulting plastic localisation in the HAZ after tensile deformation in a tensile test specimen.

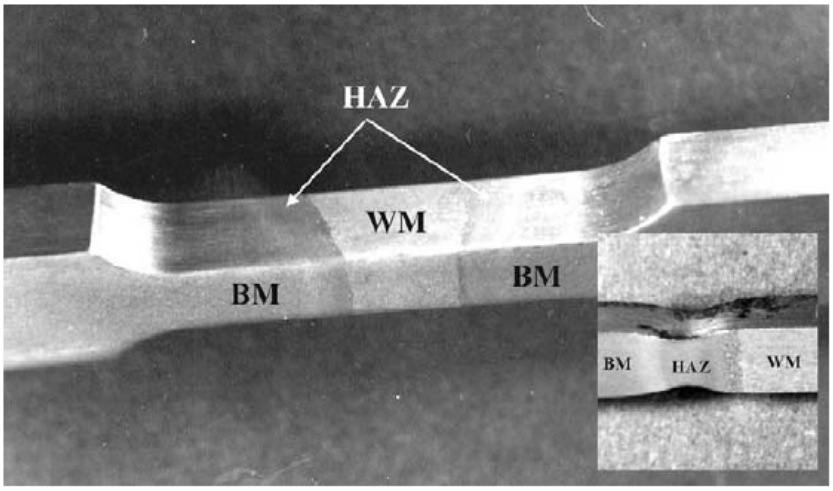

Figure 2.13: Constitutive weld zones of a tensile test specimen and resulting deformation in HAZ [41].

The "rule of mixtures" or iso-strain method is used to analyse tensile tests in which the weld line is parallel to the tensile load. Various authors have used this method to characterise weld profiles [42-44]. Kim et al. [42] performed FEM on bursting failure of seam welded tubes and found that initial fracture takes place in the HAZ near the weld line. From their stress- strain curves they found that the HAZ has a lower work hardening aspect than the base metal as shown in Figure 2.14. Figure 2.11 also shows that the yield strengths of the weld and base metal are slightly higher than that of the HAZ.

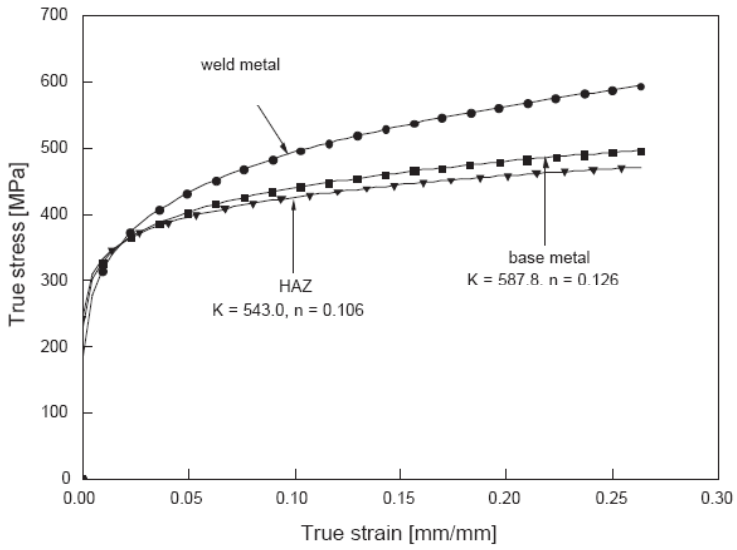

Figure 2.14: True stress- true strain curve weld zones [42].

Micro-tensile specimens yield more accurate results as they can be cut from each weld zone and the stress-strain curve can be obtained for each zone. Cam et al. [45] used this method to characterise a variety of laser beam welded steel joints. Micro-tensile specimen stress-strain curves compare well with regular circular tensile test specimens taken from the BM. This type of characterisation includes a measure of the different ductilities in the weld zones which is very useful for any failure modeling using FEM.

2.6 Final Comments

A brief summary of an extensive literature review has been presented focusing on topics such as crashworthiness, energy absorbers, buckling modes and numerical studies on square tubes. Although the topic of crushing square tube specimens has been extensively and comprehensively studied, the use of multiple tubes as energy absorbers in systems is a fairly new and ongoing field of research. Hitherto no studies having been carried out to investigate axially stacked tubes (in particular the effect of plate-divided and welded axially stacked tubes) the novelty of this topic provides the motivation for this research as well as further contributing to the field of thin-walled structured as impact energy absorbers.

3. EXPERIMENTAL DETAILS

This chapter serves as a detailed description of the research procedures that were followed. It describes all experimental apparatus and the techniques used for gathering information. The theory used in the analysis of tensile tests, quasi-static and dynamic axial crush tests is discussed. Results are presented in Chapter 4.

3.1 Tensile Testing

The material of the thin-walled square-tube sections used in this study is mild steel produced by a steel tube manufacturer of South Africa. The manufacturing techniques and the chemical composition of the mild steel are unknown. The nominal thickness of the mild steel throughout the square-tubes is 1.6mm with a range of thickness from 1.55 to 1.6 mm. Inconsistencies in the manufacturing of the steel may have occurred which may cause a variation in material properties. Tensile tests are performed on specimens cut out from the sides of the mild steel tubes (as shown in Figure 3.1) to determine main material properties.

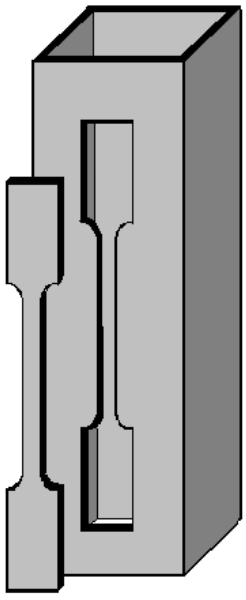

Figure 3.1: Tensile test specimen extracted from side of a square tube.

3.1.1 Test procedure

Tensile test specimens are manufactured in conformance with the British Standard BS EN 10002-1:2001 system and tensile tests are conducted in the Centre for Material's Engineering of University of Cape Town. Prior to testing, the thickness and width of each specimen is measured at different points along the length. Each specimen has a nominal gauge length of 50 mm and a width of 1.6 mm. The geometry of the specimens is shown in detail in Figure 3.2. The red markings on the specimen in Figure 3.3 show the location of the gauge length. Anisotropy is not investigated and the specimens are tested only in the rolling direction (0°) since tubes are crushed axially in this direction during quasi-static and dynamic tests.

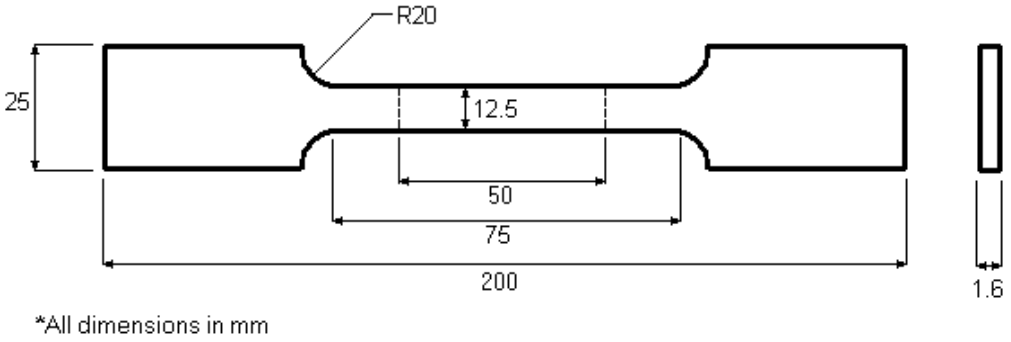

Figure 3.2: Quasi-Static tensile test specimen geometry.

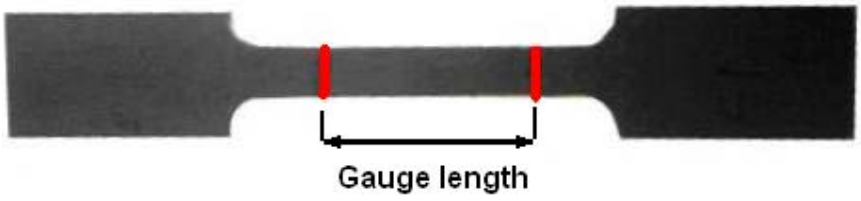

Figure 3.3: A tensile test specimen showing the gauge length.

The specimens are tested on a Zwick 1484 tensile testing machine shown in Figure 3.4(a) and (b) and tested under displacement control at room temperature. The tensile test specimen is mounted in the test grips and the force is zeroed before testing starts. The cross-head speed and hence strain rate are kept constant during testing. The

specimens are slowly loaded in tension while the load and the deflection data are recorded on a computer using the TestXpert software package. The Zwick machine has a nominal load capacity of 200 kN, but for tensile tests the grips are only rated to 100 kN.

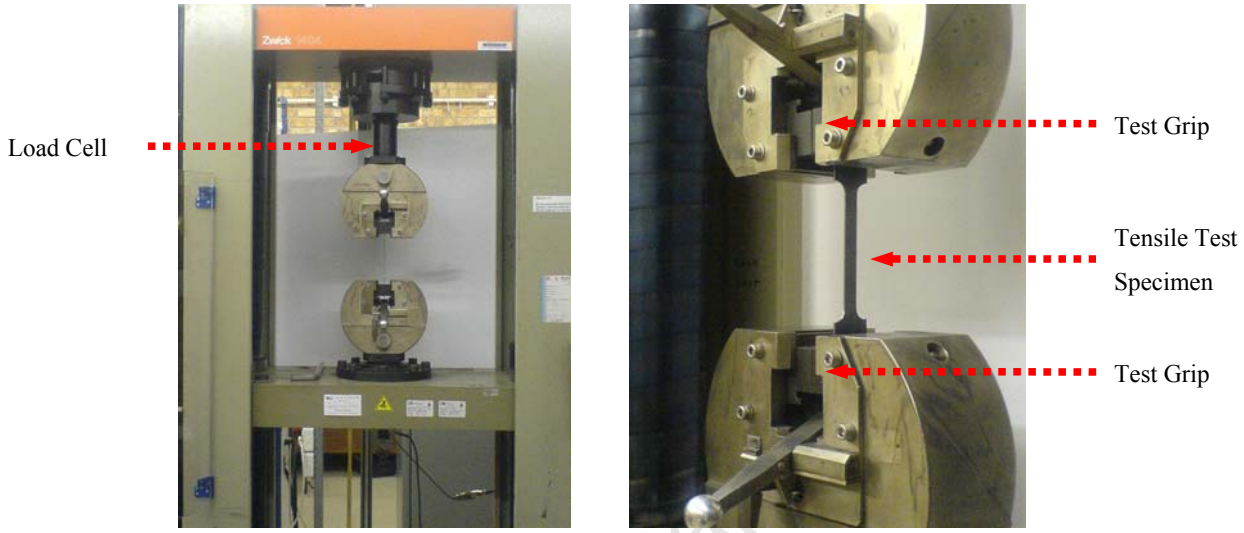

Figure 3.4: Zwick tensile test machine.

The quasi-static tensile tests are performed at cross-head speeds of 10, 20, 50 and 100 mm/min. These cross-head speeds correspond to strain rates of 3.33×10^{-3}, 6.67×10^{-3}, 1.67×10^{-2} and 3.33×10^{-2} s^{-1} respectively for an initial gauge length of 50mm. While the use of an extensometer would provide more accurate readings it was considered not necessary because the displacement of the cross-bed, constantly monitored by the Zwick machine, was within experimental errors and was considered accurate enough.

Force versus displacement curves are acquired from the data outputted by the TestXpert program. The maximum slope of the linear part of the force versus displacement curve represents the effective stiffness of the specimen. Figure 3.5 shows that the first part of the curve is not linear. This is due to machine compliance and 'bedding in' and is represented by 'x' in figure 3.5. All points are shifted left by 'x' to remove the effects of machine compliance and 'bedding in'. Also, the displacement data captured by the TestXpert program is the displacement of the entire

specimen but to plot force versus displacement curves, only the displacement of the gauge length is required. Therefore, all points on the curves are multiplied by a factor (equal to final displacement of gauge length/ final displacement of entire specimen) to remove the displacement of the specimen outside the gauge length.

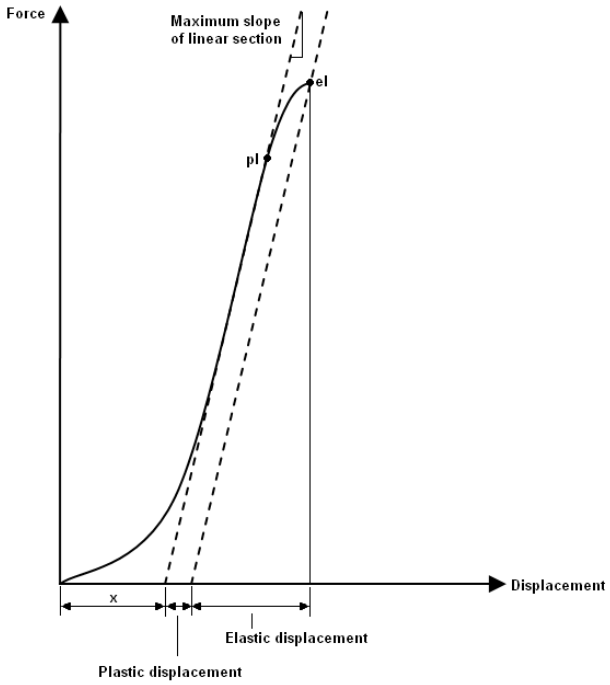

Figure 3.5: 'Smoothing' of force-displacement curve [47].

As shown in Figure 3.2 the parallel length of the specimens is 75mm, but the specimen is expected to fail within the 50mm gauge length. Sometimes however a specimen can neck outside the gauge length. The results of these specimens are still useful until the peak of the force versus displacement curves. The experimental force versus displacement curves are shown in Figures 3.6 (a) and (b).

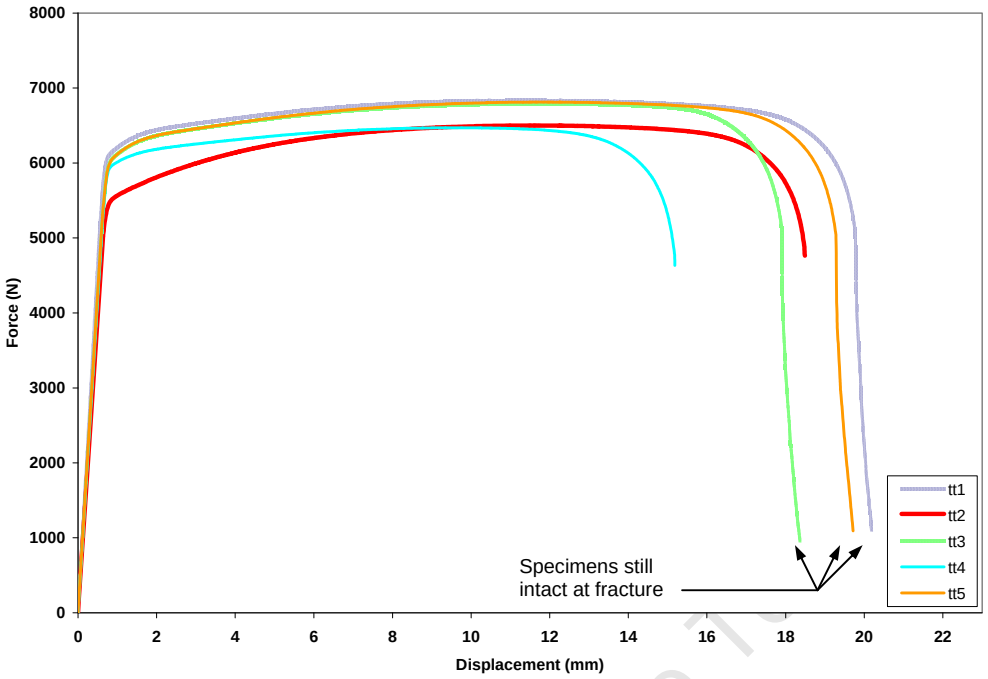

(a) Cross-head speed = 10mm/min

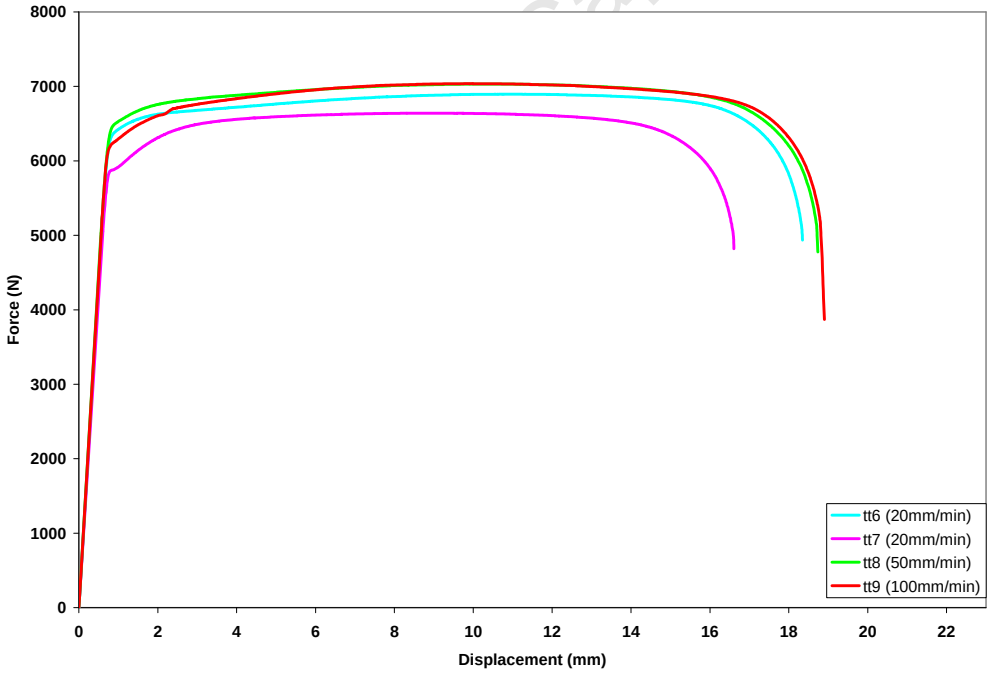

(b) Higher cross-head speeds

Figure 3.6: Force versus displacement graphs for experimental tensile tests.

3.1.2 Analysis of Tensile Test Data

This section presents the equations used to generate true stress versus true strain curves from force versus displacement curves. The theoretical approach was followed similarly to that proposed by Shigley *et al.* [46] and Bonorchis [47].

The cross-sectional area of the gauge section of the specimen is given by:

$$A_g = w_g t_g \tag{3.1}$$

Where w_g and t_g are the specimen gauge width and thickness respectively.

The strain rate at which each specimen is tested is a function of the cross-head speed (chs) and the gauge length (L_g) of the specimen:

$$\dot{\varepsilon} = chs / L_g \tag{3.2}$$

The *dynamic tensile stress* is given by:

$$\sigma_y^d = P / A_g \tag{3.3}$$

where P is the tensile load applied to the specimen.

The *static tensile stress* can be calculated by rearranging the following equation to solve for σ_y:

$$\sigma_y^d / \sigma_y = 1 + \left(\dot{\varepsilon} / D\right)^{1/q} \tag{3.4}$$

where D = 844s^{-1} and q = 2.207 (these are values obtained for South African mild steel from Hopkinson bar tests [25]).

Equation (3.4) is known as the Cowper-Symonds Equation for converting dynamic stress to static stress. *D* is the *Cowper-Symonds coefficient* and *q* is the *Cowper-Symonds exponent.*

The extension of the gauge length is given by ΔL_g which is the difference between L and L_g where L_g is the gauge length corresponding to load P. The strain is calculated from:

$$\varepsilon = \Delta L_g / L_g \tag{3.5}$$

During the test, the data is recorded by the TestXpert program and a force-displacement diagram is plotted. Using the equations above, a stress-strain diagram can be plotted. Figure 3.7 portrays a typical stress-strain diagram for a ductile material.

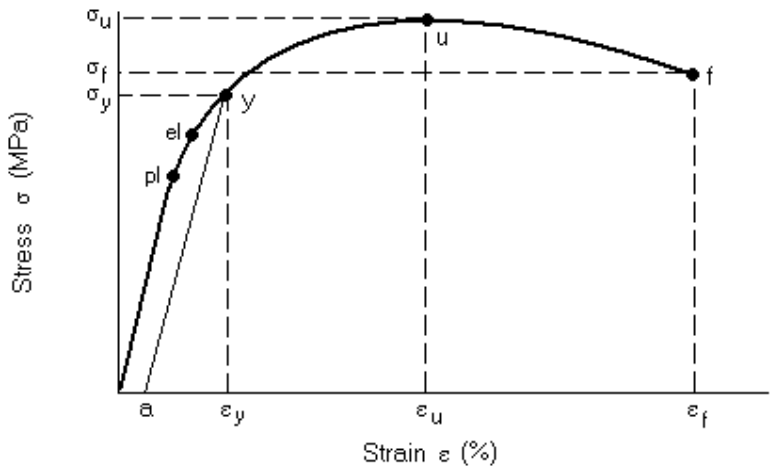

Figure 3.7: Stress-Strain curve for a ductile material [46].

Point *pl* is called the *proportional limit*. This is the point where the curve first starts to deviate from a straight line. If the load is removed at this point, no permanent set will be observable at this point. In the linear range, the uni-axial stress-strain relation is given by *Hooke's law* as

$$\sigma = E\varepsilon \tag{3.6}$$

where E is *Young's modulus* or *modulus of elasticity* and is the slope of the stress-strain curve. However, for this investigation, **210 GPa** is used for E as this is a commonly used value in theoretical calculations involving mild steel.

Point *el* is called the *elastic limit.* If the specimen is loaded beyond this point, Plastic deformation takes place and the material will take on a permanent set when the load is removed.

The material will reach a point where the strain begins to increase rapidly without a corresponding increase in stress. This point is the *yield point.* The *ultimate tensile stress,* σ_u, is the maximum stress reached and corresponds to point *u* in Figure 3.4. The values σ and ε, as shown in Figure 3.7, are known as *engineering stress* and *engineering strain* respectively and are not *true* values.

The stress calculated in Equation (3.3) is based on the original area *before* the load is applied. In reality, as the load is applied the area reduces so that the *actual* or *true stress* is larger than the *engineering stress*. To obtain the true stress the load and the cross-sectional area must be measured simultaneously during the test. Figure 3.4 represents a ductile material where the stress appears to decrease from points σ_u to σ_f. Typically, beyond the point σ_u, the specimen begins to "neck" at a location of weakness where the area reduces dramatically. For this reason the true stress is much higher than the engineering stress at the necked section.

Engineering strain given by Equation (3.5) is based on the net change in length from the original length. However, it is customary to use the *true strain*, often called *logarithmic strain* in a *true stress-strain diagram*. *True strain* is the sum of incremental elongations divided by the current gauge length.

For each test, the *true stress,* σ_{true}, and *true strain* in the longitudinal direction or *logarithmic strain*, ε_{true}, can be calculated as follows:

$$\sigma_{true} = \sigma_0(1+\varepsilon) \tag{3.7}$$

$$\varepsilon_{true} = \ln(1+\varepsilon) \tag{3.8}$$

Equations 3.7 and 3.8 are only applicable for the elastic portion of the stress-strain diagram. There are other mathematical functions that give slightly more accurate stress and strain values. However, for the purposes of this research, it is sufficient to go as far as to establish the *True Stress* and *True Strain* since that is all that is needed to determine the *yield stress* σ_y of mild steel. True stress vs true strain curves and engineering stress vs engineering strain curves are shown in Figure 3.8 for cross-head speeds of 10mm/min and higher cross-head speeds respectively.

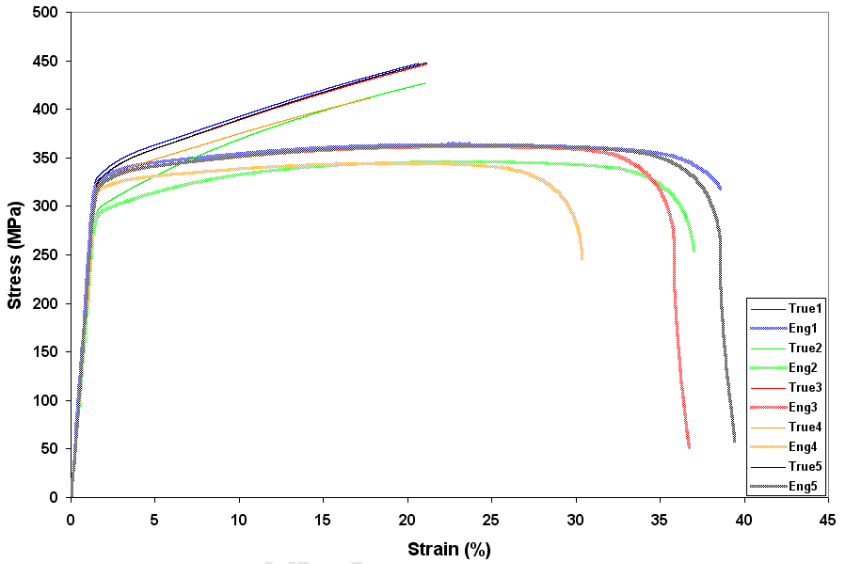

(a) Cross-head speed = 10mm/min

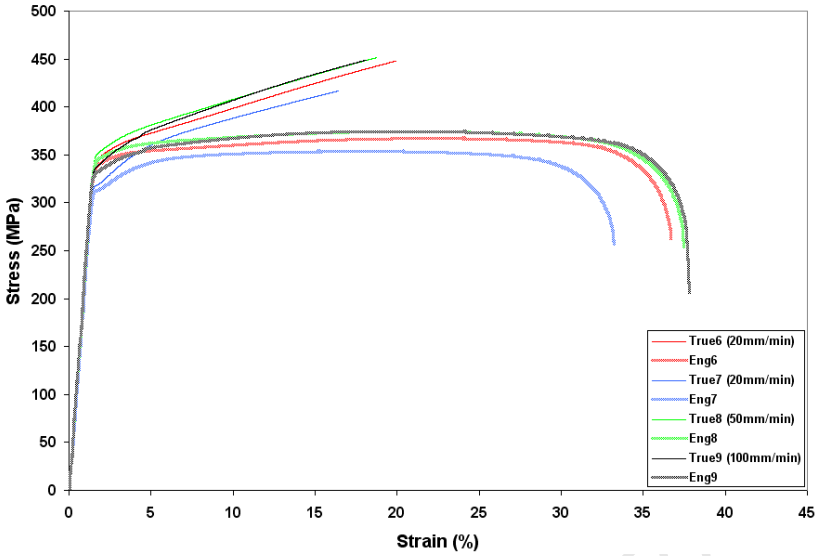

(b) Higher cross-head speeds

Figure 3.8: Force versus displacement graphs for experimental tensile tests.

Often, there is not a clear or obvious yield point, so *yield stress*, σ_y, can be defined by an *offset method* as shown in Figure 3.7. Line *ay* is drawn at slope *E*. Point *a* is usually given as 0.2 % of the original gauge length (ε = 0.002). The yield stresses obtained by the offset method for each specimen are shown in Table 3.1.

Table 3.1 Yield stresses of tensile test specimens obtained from offset method.

Specimen	*1*	*2*	*3*	*4*	*5*	*6*	*7*	*8*	*9*
chs (mm/min)	10	10	10	10	10	20	20	50	100
$\dot{\varepsilon}$ **(s^{-1})**	3.33×10^{-3}	3.33×10^{-3}	3.33×10^{-3}	3.33×10^{-3}	3.33×10^{-3}	6.67×10^{-3}	6.67×10^{-3}	1.67×10^{-2}	3.33×10^{-2}
ε **at failure (%)**	40.6	37.2	37.0	30.6	39.6	37.0	33.4	37.8	38.0
σ_y^d **(MPa)**	330	302	327	323	326	346	320	351	338
σ_y **(MPa)**	329	301	326	322	325	344	318	348	335

The average static yield stress of the nine specimens is calculated to be **328 MPa**.

Due to necking of the specimens there is a component of hydrostatic tensile stress which causes the measured stress (after necking) to be higher than the actual true material stress. The necking correction (to remove the effects of hydrostatic stress) for a rectangular specimen can be accomplished by using the MLR method by Mirone [48, 49] which involves multiplying the nominal (uncorrected) true stress values after necking by

$$1 - 0.6058(\varepsilon_{eq} - \varepsilon_N)^2 + 0.6317(\varepsilon_{eq} - \varepsilon_N)^3 - 0.2107(\varepsilon_{eq} - \varepsilon_N)^4 \qquad (3.9)$$

where ε_{eq} is the current value of the true strain and ε_N is the strain at necking initiation.

The corrected true stress-strain curve for specimen 1 is shown in Figure 3.9.

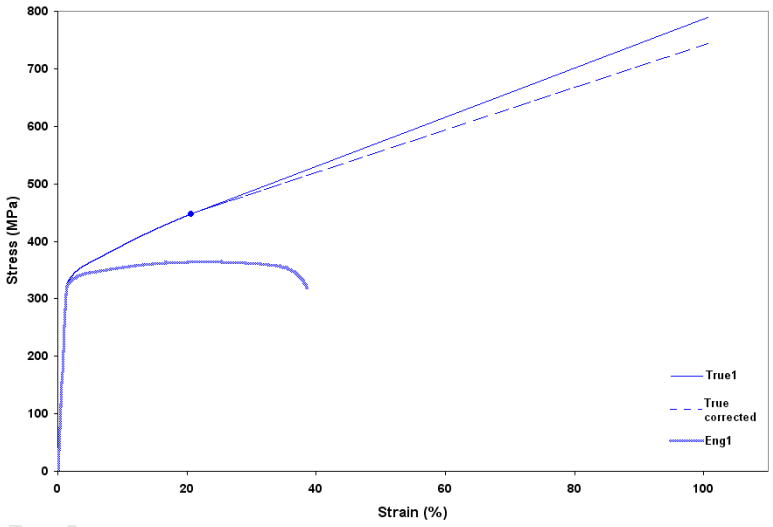

Figure 3.9: the influence of tensile necking on the tensile stress-strain curve for specimen 1.

3.2 Axial Crushing of Two Thin-Walled Square Tubes

From the outset of this project, the intention was to investigate the energy absorption characteristics by the plastic deformation of two square-tubes axially stacked and axially welded. A number of two-tube profiles were axially crushed quasi-statically and dynamically.

3.2.1 Tube Sizes and Configurations

All specimens have the same thickness *H* and width of a side *C* - 1.6 mm and 50 mm, respectively, with slightly rounded edges as portrayed in Figure 3.10. Since *C* and *H* remained constant, it follows that the ratio *C/H* also remained constant. For this research *C/H* has a value of **31.25**. As mentioned in Chapter 2, Jones [2] proposes that symmetric crushing mode forms in thin square tubes with $C/H > 40.8$ approximately. The extensional mode of crushing is predicted to form in thick square tubes with $C/H < 7.5$, approximately. The asymmetric mixed mode B-type progressive buckling is predicted to form within the range $7.5 \leq C/H \leq 40.8$. Therefore, the specimens used in this research are expected to buckle progressively in the asymmetric B-type mode.

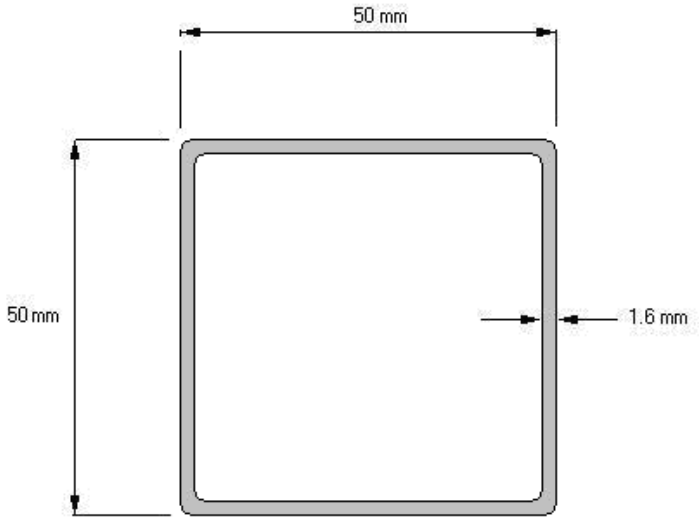

Figure 3.10: Cross-Section view of Tube Specimen.

Three different configurations are set up for experimental testing as shown in Figure 3.11. Configuration **s** is a single tube specimen while configurations **p** and **w** are both axially stacked two-tube specimens. Configuration **p** includes a rigid mild steel plate in between the top and bottom tube. The plate and top tube are balanced on top of the bottom tube but are not tied in any way. The mild steel plate (shown in Figure 3.12a) measures 75 mm × 75 mm and has a thickness of 10 mm. Configuration **w** is a welded specimen. Two tubes are seam welded together on all four sides of the two tubes by the process of Gas Tungsten Arc Welding (GTAW), more frequently referred to as TIG welding. TIG welding is a commonly used high quality welding process. A TIG welded specimen is shown in Figure 3.12b. In **p** and **w** configurations the top and bottom tubes have equal unclamped lengths. The bottom 50 mm of each specimen is clamped during testing and is thus not able to deform. In both plate-divided and welded specimens, care was taken to ensure the appropriate alignment of top and bottom tubes. During welding top and bottom tubes are clamped so as to minimise misalignment, while in the case of plate-divided specimens, the plate is marked on both sides with squares such that when the specimen is set up, the four edges of the cross-sections of each tube are parallel with their corresponding edges on the other tube and the edges of the plate.

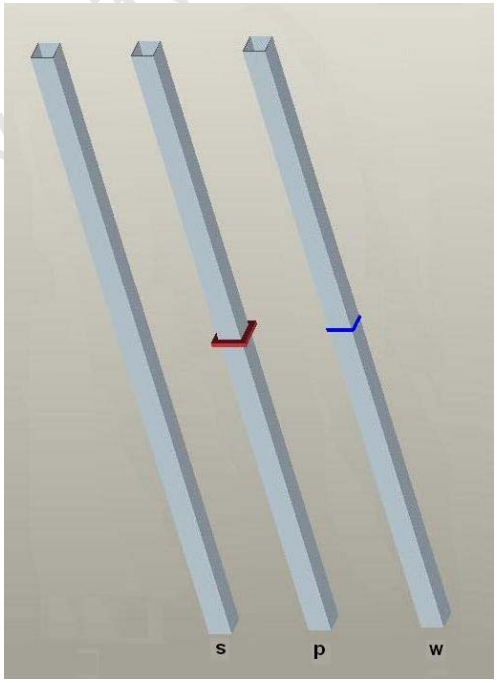

Figure 3.11: Tube configurations.

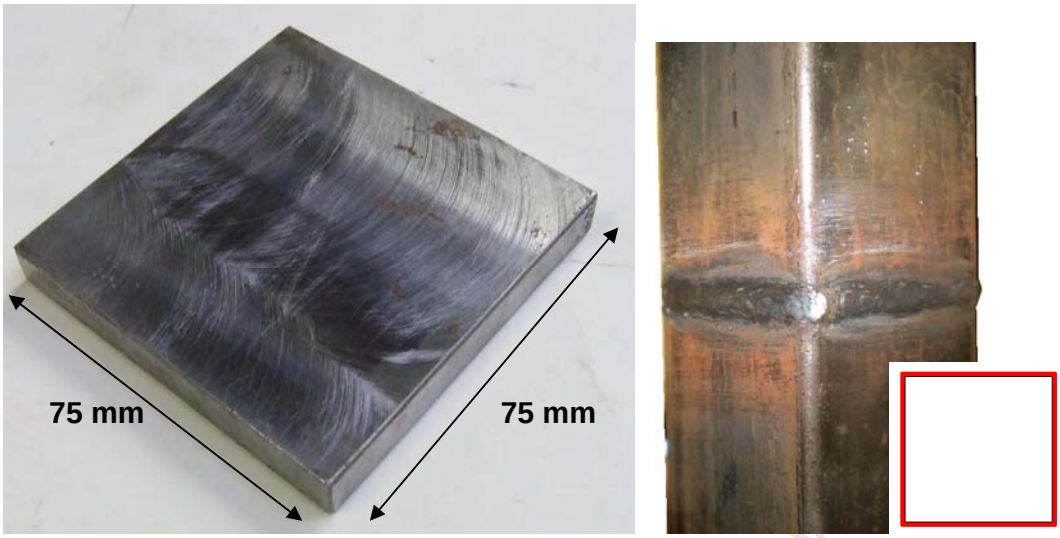

(a) **(b)**

Figure 3.12: (a) Rigid mild steel plate inserted between tubes in 'p' configuration and (b) two mild steel tubes TIG welded together (with top view shown) as in 'w' configuration.

3.2.2 Specimen Clamp

An existing clamp is used to hold specimens in place during quasi-static and dynamic crush tests. The clamp, shown in Figure 3.13, holds the bottom 50 mm of each specimen fixed, which prevents that section of the specimen from crushing. It also ensures that the specimen stands upright and level. The clamp is tightened with cap screws. To make certain that the clamp does not shift during a drop test for dynamic testing the clamp is bolted to the base of the drop test rig. On the other hand, during quasi-static testing, the clamp does not have to be bolted down since the almost constant downward pressure applied to the specimen during quasi-static crushing allows for negligible lateral displacement.

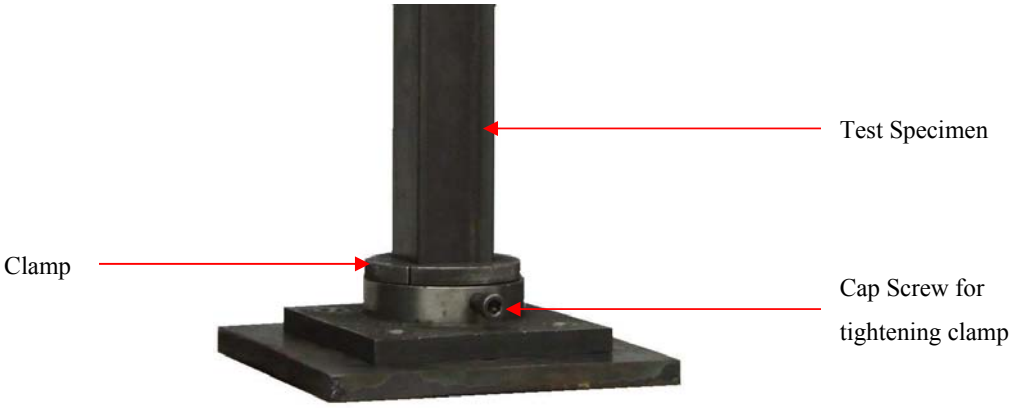

Figure 3.13: Clamp used to secure specimen in quasi-static and dynamic tests.

3.2.3 Quasi-Static Axial Crushing

Quasi-static tests are performed to investigate the manner in which specimens buckle and to ascertain the magnitude of forces involved during buckling. The Zwick testing machine is used for the axial crushing of the specimens. Figure 3.14 shows a specimen prepared for quasi-static testing.

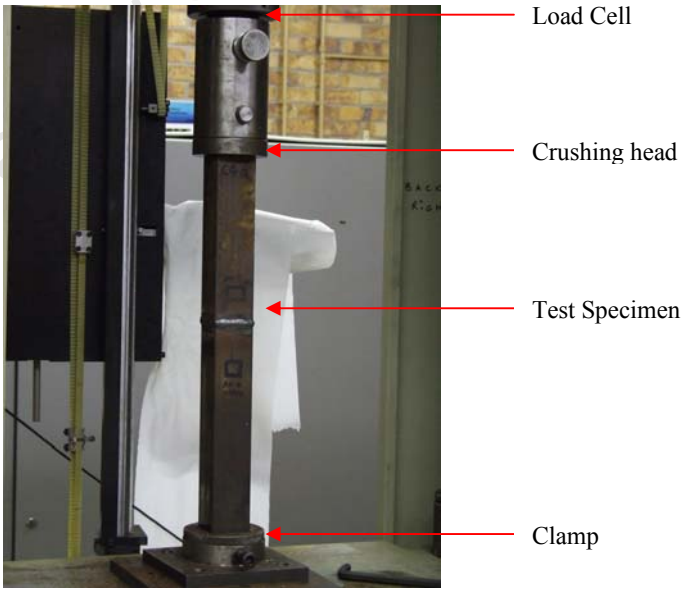

Figure 3.14: A welded specimen ready for quasi-static crushing in the Zwick testing machine.

The specimens are crushed at average strain rates that were within the quasi-static region. These strain rates were of the same order of magnitude (10^{-3} s^{-1}) as what is used in the tensile tests. For a square tube, mean strain rate is given by Jones [2] as

$$\dot{\varepsilon} = 0.33\left(\frac{chs}{C}\right) \tag{3.10}$$

where *chs* is the cross-head speed. Typically for quasi static crush tests, strain rates range from 10^{-3} to 10^{-2} s^{-1}.

Similar to the tensile tests, the Zwick records the instantaneous crush load at a certain cross head displacement and the TestXpert program plots an axial force- axial displacement curve. From this curve the peak force P_{ult} can be read off and the mean crushing force P^s_m can be calculated and compared with the theoretical value as proposed by Jones for a strain rate insensitive material [2]:

$$P^s_m \Big/ M_0 = 52.22\left(\frac{C}{H}\right)^{1/3} \tag{3.11}$$

Where $$M_0 = \sigma_y \frac{H^2}{4} \tag{3.12}$$

So for a yield stress of 328MPa, M_0 = 210N, thus making P_m^s = 34.5kN.
The total plastic deformation energy is calculated from the mean crushing force P^s_m and the final cross-head displacement δ.

$$E_p = P_m^s \times \delta \tag{3.13}$$

The *chs* and the crushed distance δ are specified on the user interface of the TestXpert program before each test commences.

3.2.4 Dynamic Axial Crushing

The drop test rig at UCT's BISRU is used to perform all dynamic tests (Figure 3.15).

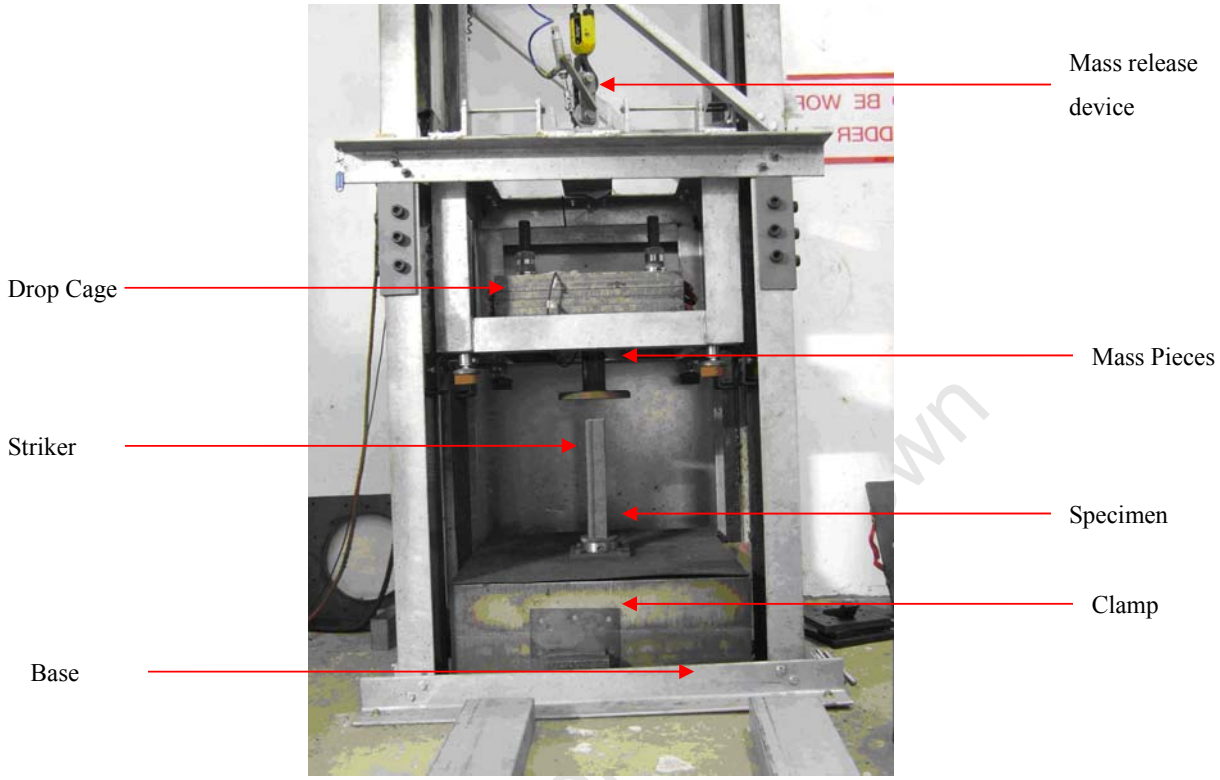

Figure 3.15: Drop Tester for dynamic testing.

Each specimen is inserted into the clamp which is securely bolted to the base. Care is taken to ensure that each specimen is level so that it is likely to crush in the desired manner. The mass of the cage and the mass pieces is kept constant at **340 kg**. The drop cage with the mass pieces is lifted to a specified height and then released. The drop heights used and their corresponding impact velocities are shown in Table 3.2.

Table 3.2 Drop heights and their corresponding impact velocities

Drop Height (m)	*Impact Velocity of Drop Mass (m/s)*
1.69	5.75
2.15	6.50
2.68	7.25
3.26	8.00
3.90	8.75

The impact velocities are calculated from the conservation of energy, assuming that the potential energy $E_{potential}$ of the drop mass, at the above mentioned heights, would be converted into kinetic energy $E_{kinetic}$ at the moment of impact. Since the rails of the drop test rig are well lubricated, the effect of friction is assumed to be negligible and therefore not taken into account. Potential energy is equated to kinetic energy as follows:

$$E_{potential} = E_{kinetic} \tag{3.14}$$

$$Mgh = \tfrac{1}{2} MV_i^2 \tag{3.15}$$

where M is the drop mass, g is gravitational acceleration (9.81m/s), h is the drop height and V is the impact velocity; this can be rearranged as follows

$$V = \sqrt{2gh} \tag{3.16}$$

The Total plastic deformation energy E_p is the energy absorbed by a specimen at the instant the drop mass comes to rest. It is given by

$$E_p = Mg(h + \delta) \tag{3.17}$$

where δ is the overall deflection of the specimen. The overall deflection of a specimen is measured mechanically using a height gauge.

The mean dynamic crushing force P^d_m, was calculated form the total energy absorbed by the tube system and the deflection of the tubes

$$P_m^d = \frac{E_p}{\delta} \tag{3.18}$$

The use of a high-speed camera and Photron software allows one to measure the time taken to crush a specimen. The software also allows footage to be stopped at any stage

of the crushing of a specimen to determine the crushed distance at a specific time. Graphs of tube length vs time are plotted for some specimens in Chapter 5. This is a very time consuming process and slightly inaccurate. Since the drop height and crush distance is known, average deceleration, *a*, can be calculated from the simple equation of motion:

$$\delta = Vt + \tfrac{1}{2}at^2 \tag{3.19}$$

where t is the time taken from the moment the striker touches the specimen to the time when the specimen is completely crushed. From Newton's second law we know that $F = Ma$. Therefore the mean crushing force is:

$$P_m^d = Ma \tag{3.20}$$

where *M* is the mass of the drop cage. This equation does not take into account the mass of the tubes.

From equations 3.17 and 3.19 we have two experimental mean crushing load values that can be compared to the theoretical value given by Jones [2] as:

$$P_m^d\,(theoretical) = 13.05\sigma_0 H^2 \left(C/H\right)^{1/3} \left\{1 + \left(0.33V/CD\right)^{1/q}\right\} \tag{3.21}$$

Theoretical values for the mean dynamic crushing force for the drop heights that were used are given in Table 3.3.

Table 3.3 Theoretical mean dynamic crushing forces for given drop heights

Drop Height (m)	***Impact Velocity of Drop Mass (m/s)***	P^d_m **(kN)** **(theoretical)**
1.69	5.75	41.94
2.15	6.50	42.40
2.68	7.25	42.85
3.26	8.00	43.26
3.90	8.75	43.66

Force-displacement graphs cannot be generated during dynamic tests due to limitations in measuring equipment because of budget constraints.

The geometric efficiency e_G as used by Arnold and Altenhof [8] is a measure of how well an absorber compresses. It is the ratio of the total crosshead displacement δ_T, to the original length of the absorber, L. Geometric efficiency is used as a basis of comparison for dynamic tests.

$$e_G = \frac{\delta}{L} \tag{3.22}$$

Arnold and Altenhof [8] also used the specific energy of a structure as a performance metric. It is the energy absorbed by a structure divided by its mass. This is useful for comparing energy absorption of specimens with different masses.

$$S_e = \frac{E_p}{m} \tag{3.23}$$

where m is the mass of the absorber.

3.2.5 Comparison between Quasi-Static and Dynamic Tests

Where possible, quasi-static and dynamic test specimens are compared. Experimental results are compared with the theoretical [2] force ratio.

$$P_m^d \Big/ P_m^s = 1 + \left(0.33V \Big/ CD\right)^{1/q} \tag{3.24}$$

3.3 Final comments

The experimental procedure for conducting quasi-static and dynamic tests has been described. Although experimental setup is not difficult by any means, care needs to be taken and a certain level of experience is needed to ensure that desirable and accurate results are obtained. Thus theoretical equations are used as a basis to ensure that experimental results are at an adequate level of acceptability.

4. EXPERIMENTAL RESULTS

This chapter outlines the results of the quasi-static and dynamic crushing tests. Results are presented through tables, graphs and test images for easier recognition. More detailed analysis of the results is presented in Chapter 5. Work on this thesis is a continuation of work carried out during the author's undergraduate thesis involving dynamic tests on plate-divided specimens. Furthermore, preliminary tests prior to this thesis were carried out to investigate the performance of different weld configurations in welded tube specimens. Section 4.1 explains the naming system used for these tests.

4.1 Identification of Dynamic Tests

Throughout this thesis, tests mentioned as part of **Group A** refer to tests performed on plate-divided specimens as part of the author's undergraduate thesis in 2006. **Group B** refers to preliminary tests performed by the author on axially stacked and welded tubes with different weld configurations in 2007. **Group C** refers to tests performed for this thesis and is the primary focus of this investigation. Table 4.1 summarises the number of tests performed for each Group. Table 4.2 summarises results of 46 dynamic tests performed in Group A. Table 4.3 summarises results of 34 dynamic tests performed in Group B. Table 4.4 and Table 4.5 summarise results of 74 dynamic tests performed in Group C.

Table 4.1 Summary of all dynamic tests

Group	*Year*	*Tests performed*	*Successful tests*	*Unsuccessful tests*	*Main focus*		
					s	*w*	*p*
A	2006	46	34	12			×
B	2007	34	22	12		×	
C	2008	74	74	-	×	×	×

Notation used in Table:
s **single tube specimens**
w **welded tubes specimens**
p **plate-divided tubes specimens**

Table 4.2 Experimental data for Group A dynamic tests (plate-divided specimens)

(with C = 50mm, H = 1.6mm and M = 340kg)

Specimen	***L*** ***(mm)***	***h*** ***(m)***	***V*** ***(m/s)***	δ_{L1} ***(mm)***	δ_{L2} ***(mm)***	δ_{total} ***(mm)***	E_{pd} ***(kJ)***	P^{d}_{m} ***(kN)***	***Deformation mode [lobes]***
150p100A	250	3.293	8.04	92.1	82.6	175	11.57	66.20	IF [3.5][2]
150p100B	250	2.148	6.49	-	-	-	-	-	TS
150p100C	250	2.153	6.50	80.2	82.8	163	7.72	47.40	S [3][2.5]
150p125A	275	2.152	6.50	54.4	103.3	158	7.70	48.85	S [2][4]
150p125B	275	2.676	7.25	-	-	-	-	-	FO
150p125C	275	2.683	7.26	56.0	104.5	161	9.48	59.08	S [1.5][3.5]
150p125D	275	3.291	8.04	110.3	103.4	214	11.69	54.69	S [4.5][4.5]
150p150A	300	3.286	8.03	94.4	116.4	211	11.66	55.33	S [3.5][5]
150p150B	300	2.681	7.25	-	-	-	-	-	FO
150p150C	300	2.155	6.50	23.2	121.0	144	7.67	53.18	S [1][4.5]
100p200A	300	3.262	8.00	37.9	163.1	201	11.55	57.46	S [1][7]
100p200B	300	2.682	7.25	7.3	161.6	169	9.51	56.31	S [0.5][6.5]
100p200C	300	2.155	6.50	79.2	55.5	135	7.64	56.76	IF [2.5][1.5]
100p200D	300	2.159	6.51	0.0	134.3	134	7.65	56.94	S [0][5.5]
150p175A	325	3.287	8.03	70.1	138.8	209	11.66	55.81	S[3.5][5.5]
150p175B	325	2.682	7.25	-	-	-	-	-	FO
150p175C	325	2.682	7.25	23.6	142.9	167	9.50	57.06	S [1][5.5]
150p175D	325	2.161	6.51	0.0	141.0	141	7.68	54.47	IF [0][6]
125p200A	325	3.258	8.00	36.7	157.6	194	11.51	59.27	S [1][7]
125p200B	325	2.679	7.25	8.1	165	173	9.51	54.95	S [0.5][6.5]
125p200C	325	2.152	6.50	0.0	148.7	149	7.67	51.59	S [0][6]

Notation used in Table:

p	**plate-divided tubes specimen**
A	**Asymmetric progressive**
FO	**Fly-out failure**
G	**Global bending**
IF	**Irregular folding**
S	**Symmetric progressive**
T	**Transition**
TS	**Tearing and splitting**
[ ][ ]	**Number of complete lobes in bottom and top tube, respectively**

Table 4.2 (continued)

Specimen	***L*** ***(mm)***	***h*** ***(m)***	***V*** ***(m/s)***	δ_{L1} ***(mm)***	δ_{L2} ***(mm)***	δ_{total} ***(mm)***	E_{pd} ***(kJ)***	P^{d}_{m} ***(kN)***	***Deformation mode [lobes]***
150p200A	350	3.260	8.00	-	-	-	-	-	FO
150p200B	350	3.258	8.00	34.1	163.3	197	11.53	58.38	S [1][6.5]
150p200C	350	3.298	8.04	38.1	158.9	197	11.66	59.19	S [1][6]
150p200D	350	2.681	7.25	22.5	160.8	183	9.55	52.12	S [1][6.5]
150p200E	350	2.684	7.26	5.3	161.6	167	9.51	57.00	S [0.5][6.5]
150p200F	350	2.154	6.50	0.0	131.1	131	7.62	58.12	IF [0][6.5]
150p200G	350	2.150	6.49	-	-	-	-	-	FO
150p200H	350	2.152	6.50	-	-	-	-	-	FO
150p200I	350	2.156	6.50	0.0	155.2	155	7.71	49.66	S [0][6.5]
175p200A	375	3.897	8.75	55.7	165.0	221	13.76	62.23	IF [1.5][6]
175p200B	375	3.288	8.03	-	-	-	-	-	FO
175p200C	375	3.266	8.00	30.5	164.9	195	11.55	59.07	S [1][6.5]
175p200D	375	2.682	7.25	0.0	161.7	162	9.48	58.66	S [0][6.5]
200p200A	400	3.901	8.75	-	-	-	-	-	FO
200p200B	400	3.288	8.03	-	-	-	-	-	FO
200p200C	400	3.258	8.00	18.3	160.5	179	11.46	64.10	IF [1][4]
225p200A	425	4.313	9.20	55.5	165.7	221	15.12	68.37	S [1.5][5.5]
225p200B	425	3.901	8.75	65.9	162.4	228	13.77	60.32	S [2.5][6.5]
225p200C	425	3.292	8.04	28.8	164.2	193	11.62	60.19	IF [1][6]
225p200D	425	2.682	7.25	0.0	160.3	160	9.48	59.15	IF [0][5]
225p200E	425	2.125	6.46	-	-	-	-	-	FO
250p200A	450	3.902	8.75	-	-	-	-	-	FO
250p200B	450	3.917	8.77	194.2	34.6	229	13.83	60.42	S [8][1]
250p200C	450	3.292	8.04	42.8	162.2	205	11.66	56.90	S [1][7]
250p200D	450	2.676	7.25	0.0	164.4	164	9.47	57.76	S [0][6]

Notation used in Table:

p	**plate-divided tubes specimen**
A	**Asymmetric progressive**
FO	**Fly-out failure**
G	**Global bending**
IF	**Irregular folding**
S	**Symmetric progressive**
T	**Transition**
TS	**Tearing and splitting**
[ ][ ]	**Number of complete lobes in bottom and top tube, respectively**

Table 4.3 Experimental data for Group B dynamic tests (different weld configurations)

(with C = 50mm, H = 1.5mm and M = 340kg)

Specimen	*Weld type*	L_{bottom} *(mm)*	L_{top} *(mm)*	*h (m)*	*V (m/s)*	δ_{total} *(mm)*	E_{pd} *(kJ)*	P^d_m *(kN)*	*Deformation mode [lobes]*
A1a		150	200	3.260	8.00	231	11.64	50.51	S [11]
A1b		150	200	3.260	8.00	-		-	WF – TS
A1c		150	200	3.259	8.00	272	11.78	43.23	A [11]
A1d		150	200	3.259	8.00	262	11.74	44.90	S [11]
A1e	‖	150	200	3.602	8.40	-	-	-	IF – TS
A2a		150	200	3.900	8.75	296	13.99	47.36	S [12]
A2b		150	200	3.259	8.00	-	-	-	WF – TS
A2c		150	200	3.603	8.40	-	-	-	WF – TS
A2d		150	200	3.594	8.40	-	-	-	WF – TS
A3b		150	200	3.260	8.00	-	-	-	WF – TS
A3c		150	200	3.596	8.40	286	12.95	45.32	S[11]
A3d		150	200	3.603	8.40	286	12.97	45.31	S [10]
Asingle		350	-	3.261	8.00	283	11.82	41.75	S [12]
B1a		200	200	3.259	8.00	286	11.82	41.31	S [12]
B1b		200	200	3.259	8.00	300	11.87	39.58	S [12]
B1c		200	200	3.259	8.00	253	11.71	46.27	A [10]
B1d		200	200	3.260	8.00	273	11.79	43.12	S [12]
B1e	‖	200	200	3.600	8.40	-	-	-	IF – TS
B2a		200	200	3.596	8.40	318	13.06	41.00	S [13]
B2b		200	200	3.597	8.40	321	13.07	40.73	S [13]
B2c		200	200	3.601	8.40	316	13.07	41.30	S [13]
B2d		200	200	3.596	8.40	318	13.05	41.07	S [12]
Bsingle		400	-	3.259	8.00	-	-	-	G

Notation used in Table:

A	**Asymmetric progressive**
G	**Global bending**
IF	**Irregular folding**
S	**Symmetric progressive**
T	**Transition**
TS	**Tearing and shearing**
WF	**Weld failure**
[ ]	**Number of complete lobes in bottom and top tube, respectively**

	4-sided seam	*Corner spots*	*Side spots*	*2-sided seams*	*2 side slits*	*Single tubes*
Weld schematic			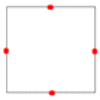			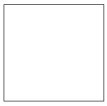

Table 4.3 (continued)

Specimen	*Weld type*	L_{bottom} *(mm)*	L_{top} *(mm)*	*h (m)*	*V (m/s)*	δ_{total} *(mm)*	E_{pd} *(kJ)*	P^d_m *(kN)*	*Deformation mode [lobes]*
C1a		250	200	3.263	8.00	284	11.83	41.63	A [12]
C1b		250	200	3.256	8.00	292	11.83	40.51	S [12]
C1c		250	200	3.264	8.00	298	11.88	39.83	S[12]
C1d		250	200	3.259	8.00	-	-	-	G
C1e		250	200	3.597	8.40	-	-	-	IF - TS
C2c		250	200	3.598	8.40	347	13.16	37.88	S [15]
C3a		250	200	3.596	8.40	336	13.11	39.04	S [15]
C3b		250	200	3.599	8.40	326	13.09	40.19	S [15]
C3c		250	200	3.598	8.40	-	-	-	WF – TS
C3d		250	200	3.599	8.40	-	-	-	WF - TS
Csingle		450	-	3.259	8.00	301	11.87	39.45	S [13]

Notation used in Table:

A	**Asymmetric progressive**
G	**Global bending**
IF	**Irregular folding**
S	**Symmetric progressive**
T	**Transition**
TS	**Tearing and shearing**
WF	**Weld failure**
[ ]	**Number of complete lobes in bottom and top tube, respectively**

	4-sided seam	*Corner spots*	*Side spots*	*2-sided seams*	*2 side slits*	*Single tubes*
Weld schematic						

Table 4.4 Experimental data for Group C dynamic tests on single and welded square tubes (with C = 50mm, H = 1.6mm and M = 340kg)

Specimen	*L (mm)*	*h (m)*	*V (m/s)*	δ_{total} *(mm)*	E_{pd} *(kJ)*	P^d_m *(kN)*	*Deformation mode [lobes]*
300sA	300	3.257	7.99	255	11.71	45.97	S [10]
150w150A	300	3.258	8.00	250	11.70	46.86	S [11]
300sB	300	2.679	7.25	238	9.73	40.81	S [10]
150w150B	300	2.679	7.25	227	9.69	42.77	S [10]
300sC	300	2.148	6.49	190	7.80	40.96	S [7]
150w150C	300	2.149	6.49	166	7.72	46.57	A [7]
300sD	300	1.689	5.76	145	6.12	42.24	S [5.5]
150w150D	300	1.688	5.75	124	6.05	48.60	A [5.5]
400sA	400	3.903	8.75	323	14.10	43.61	S [13]
200w200A	400	3.901	8.75	318	14.07	44.23	S [14]
400sB	400	3.263	8.00	285	11.83	41.58	S [11.5]
200w200B	400	3.260	8.00	269	11.77	43.70	S [12.5]
400sC	400	2.680	7.25	229	9.70	42.41	S [9.5]
200w200C	400	2.680	7.25	225	9.69	43.02	S [9.5]
400sD	400	2.150	6.49	192	7.81	40.68	S [7.5]
200w200D	400	2.150	6.49	182	7.78	42.70	S [7.5]
500sA	500	3.263	8.00	292	11.86	40.63	S [12]
250w250A	500	3.260	8.00	289	11.84	40.93	S [12.5]
500sB	500	2.682	7.25	235	9.73	41.35	S [9.5]
250w250B	500	2.680	7.25	226	9.69	42.85	S [9.5]
500sC	500	2.153	6.50	184	7.79	42.45	S [7]
250w250C	500	2.150	6.49	161	7.71	47.84	S [7]
500sD	500	2.153	6.50	165	7.73	46.73	S [7]
250w250D	500	2.149	6.49	165	7.72	46.83	S [7]

Notation used in Table:

s	**single tube**
w	**welded tubes**
A	**Asymmetric progressive**
FO	**Fly-out failure**
G	**Global bending**
IF	**Irregular folding**
S	**Symmetric progressive**
T	**Transition**
[ ][ ]	**Number of complete lobes in bottom and top tube, respectively**

Table 4.5 Experimental data for Group C dynamic tests performed on square tubes (with C = 50mm, H = 1.6mm and M = 340kg)

Specimen	*L (mm)*	*h (m)*	*V (m/s)*	δ_{total} *(mm)*	E_{pd} *(kJ)*	P^{d}_{m} *(kN)*	*Deformation mode [lobes]*
550s	550	3.258	8.00	178	11.46	64.38	S [8.5]
275w275 A	550	3.259	8.00	-	-	-	T [4.5]
275w275 B	550	3.259	8.00	200	11.54	57.69	A [1] - S [7]
275p275	550	3.261	8.00	200	11.54	57.72	S [0][7.5]
600sA	600	3.260	8.00	-	-	-	T [6]
600sB	600	3.258	8.00	156	11.39	72.99	IF [7]
300w300 A	600	3.263	8.00	192	11.52	60.02	S [7.5] - T
300w300 B	600	3.260	8.00	187	11.50	61.48	S [8.5]
300p300	600	3.258	8.00	190	11.50	60.53	S [0][8.5]
650sA	650	3.257	7.99	-	-	-	T [6]
650sB	650	3.257	7.99	185	11.48	62.06	S [7.5]
325w325	650	3.261	8.00	180	11.48	63.76	IF [5]
325p325 A	650	3.258	8.00	168	11.43	68.02	IF [0][8] - T
325p325B	650	3.260	8.00	182	11.48	63.08	A [0][8.5]
700s	700	3.263	8.00	185	11.50	62.16	S [7.5]
350w350	700	3.260	8.00	-	-	-	T [4]
350p350	700	3.257	7.99	138	11.32	82.06	S [7.5][0] - T
800sA	800	3.260	8.00	185	11.49	62.08	S [7.5]
800sB	800	3.260	8.00	186	11.49	61.79	IF [7.5]
400w400	800	3.260	8.00	207	11.56	55.86	IF [7.5]
400p400	800	3.261	8.00	197	11.53	58.60	S [0][7.5]
900s	900	3.260	8.00	202	11.55	57.16	S [7.5]
450w450	900	3.260	8.00	216	11.59	53.68	S [8.5]

Notation used in Table:

s	**single tube**
w	**welded tubes**
p	**plate-divided tubes**
A	**Asymmetric progressive**
FO	**Fly-out failure**
G	**Global bending**
IF	**Irregular folding**
S	**Symmetric progressive**
T	**Transition**
[ ][ ]	**Number of complete lobes in bottom and top tube, respectively**

Table 4.5 (continued)

Specimen	*L (mm)*	*h (m)*	*V (m/s)*	δ_{total} *(mm)*	E_{pd} *(kJ)*	P^d_m *(kN)*	*Deformation mode [lobes]*
1000s	1000	3.263	8.00	175	11.47	65.57	A [0][7]
500w500	1000	3.262	8.00	178	11.47	64.46	IF [8] - T
500p500	1000	3.260	8.00	201	11.54	57.51	S [0][8]
1100s	1100	3.260	8.00	-	-	-	T [6]
550w550	1100	3.261	8.00	215	11.59	53.92	S [8.5]
550p550	1100	3.257	7.99	218	11.59	53.17	S [0][8.5]
1200sA	1200	3.258	8.00	137	11.32	82.74	IF [6]
1200sB	1200	3.257	7.99	190	11.50	60.51	IF [7.5]
600w600	1200	3.258	8.00	-	-	-	T [6]
600p600	1200	3.258	8.00	174	11.45	65.92	S [0][7.5]
1300s	1300	3.258	8.00	207	11.56	55.83	S [8]
650w650	1300	3.262	8.00	206	11.57	56.15	S [8]
650p650	1300	3.258	8.00	212	11.57	54.59	S [0][8]
1400s	1400	3.260	8.00	185	11.49	62.11	IF [7]
700w700	1400	3.258	8.00	185	11.48	62.07	IF [7]
700p700	1400	3.258	8.00	193	11.51	59.64	IF [0][7]
1500s	1500	3.259	8.00	205	11.55	56.36	S [7.5]
750w750 A	1500	3.259	8.00	-	-	-	T [4]
750w750 B	1500	3.263	8.00	170	11.45	67.36	S [6.5] - T
750p750 A	1500	3.258	8.00	196	11.52	58.78	S [0][7.5] - FO
750p750B	1500	3.263	8.00	178	11.48	64.48	S [0][7.5]
1600s	1600	3.262	8.00	197	11.54	58.56	S [7.5]
800w800	1600	3.261	8.00	-	-	-	G
800p800	1600	3.260	8.00	163	11.42	70.04	S [0][8] - FO
1700s	1700	3.260	8.00	190	11.51	60.56	S [7.5] - T
850w850	1700	3.259	8.00	215	11.59	53.89	S [8.5]
850p850	1700	3.260	8.00	201	11.54	57.43	S [0][8.5]

Notation used in Table:

s	**single tube**
w	**welded tubes**
p	**plate-divided tubes**
A	**Asymmetric progressive**
FO	**Fly-out failure**
G	**Global bending**
IF	**Irregular folding**
S	**Symmetric progressive**
T	**Transition**
[ ][ ]	**Number of complete lobes in bottom and top tube, respectively**

4.1.1 Group A Dynamic Tests

As part of the author's undergraduate thesis in 2006, 46 dynamic tests were performed on plate-divided specimens; 34 of which provided successful results and 12 unsuccessful or failed tests which included bending, splitting and tearing. These tests did not form part of testing for this thesis but the results have been included for the reader's interest and also for comparison purposes in chapters that follow. The cross sectional dimensions of these specimens were the same as the specimens used for this thesis. The lengths of the specimens were in the progressive buckling region ranging from 250mm to 450mm Results of these tests are summarised in Table 4.2.

Figure 4.1 shows original and crushed profiles of specimens tested at 3.26m. The bottom tube length was kept constant while the top tube length was increased incrementally in 25mm steps from 100mm to 200mm. In each case, as the top tube was crushed to a maximum, the energy would be transferred through the rigid plate (which was not deformed during tests) and the lobe formation would continue in the bottom tube. Table 4.6 summarises these test results.

Figure 4.1: Plate-divided specimens with L_{bottom} = 150mm and L_{top} alternating from 100mm to 200mm in 25mm increments. h = 3.26m. (50mm clamp length is shown)

Table 4.6 Results on tests performed on plate-divided specimens. L_{bottom} = 150mm. h = 3.26m

Specimen	L_{bottom} *(mm)*	L_{top} *(mm)*	δ_{bottom} *(mm)*	δ_{top} *(mm)*	δ_t *(mm)*	E_{pd}^{bottom} *(kJ)*	E_{pd}^{top} *(kJ)*	E_{pd} *(kJ)*	P^d_m *(kN)*
150p100A	150	100	92.1	82.6	174.7	5.92	5.31	11.23	64.26
150p125D	150	125	110.3	103.4	213.7	5.86	5.49	11.35	53.08
150p150A	150	150	94.4	116.4	210.81	5.07	6.25	11.32	53.70
150p175A	150	175	70.1	138.8	208.9	3.80	7.52	11.32	54.17
150p200B	150	200	38.1	158.9	197.0	2.19	9.13	11.31	57.45

Figure 4.2 also shows original and crushed profiles of specimens tested at 3.26m. With these specimens, the top tube length was kept constant while the bottom tube length was increased incrementally in 25mm steps from 100mm to 250mm. Table 4.7 summarises these test results.

Figure 4.2: Plate-divided specimens with L_{top} = 200mm and L_{bottom} alternating from 100mm to 250mm in 25mm increments. h = 3.26m. (50mm clamp length is shown)

Table 4.7 Results on tests performed on plate-divided specimens. L_{top} = 200mm. h = 3.26m

Specimen	L_{bottom} *(mm)*	L_{top} *(mm)*	δ_{bottom} *(mm)*	δ_{top} *(mm)*	δ_t *(mm)*	E_{pd}^{bottom} *(kJ)*	E_{pd}^{top} *(kJ)*	E_{pd} *(kJ)*	P^d_m *(kN)*
100p200A	100	200	37.9	163.1	201.00	2.11	9.10	11.21	55.77
125p200A	125	200	36.7	157.6	194.3	2.11	9.07	11.18	57.53
150p200B	150	200	34.1	163.3	197.4	1.94	9.25	11.19	56.66
175p200C	175	200	30.5	164.9	195.4	1.75	9.46	11.21	57.33
200p200C	200	200	18.3	160.5	178.3	1.14	9.99	11.13	62.21
225p200C	225	200	28.8	164.2	193.00	1.68	9.60	11.28	58.42
250p200C	250	200	42.8	162.2	205.00	2.36	8.96	11.32	55.23

In Tables 4.6 and 4.7, the amount of energy absorbed by the top and bottom tubes (E_{pd}^{top} and E_{pd}^{bottom}, respectively) in a specimen was calculated as a percentage of the total energy absorbed, E_{pd}, by the specimen. These percentages are equal to the ratio of crushed distances of the top and bottom tubes (δ_{top} and δ_{bottom}, respectively) in a specimen compared to the total crush distance, δ_t, of the specimen. Equations 4.1 – 4.3 show these details.

$$E_{pd} = E_{pd}^{top} + E_{pd}^{bottom} \tag{4.1}$$

$$\delta_t = \delta_{top} + \delta_{bottom} \tag{4.2}$$

$$E_{pd}^{top} = \frac{\delta_{top}}{\delta_t} \times E_{pd} \tag{4.3}$$

4.1.2 Group B Dynamic Tests

These welded specimens were preliminary tests leading up to this thesis. Of the 34 tests performed, 22 provided successful results while 12 yielded unsuccessful results. The square mild steel tubes making up these specimens had the same cross sectional dimensions as the tubes used in master's testing, however the wall thickness was closer to 1.5mm instead of 1.6mm. This explains the larger crush distances measured in these specimens compared to the crush distances measured in the master's specimens. The welded specimens were within the progressive buckling region with original lengths of 350mm, 400mm and 450mm and were labelled Series A, B and C for these lengths, respectively. Four different weld configurations were tested. These included four-sided seam weld, corner spot welds, side spot welds and two sided seam welds. Three side-slit specimens and four single tube specimens were also tested. Side-split specimens are single tubes in which opposite sides are cut into with a hacksaw. Table 4.3 summarises the results obtained from the tests. Successful results are ones in which specimens buckled progressively while failed tests are ones in which bending, splitting or tearing occurs. Table 4.8 shows schematic diagrams of the weld configurations and summarises the test results in terms of number of successful and failed tests.

Table 4.8 indicates that the four-sided seam welded specimens are the most reliable as all the tests performed on these types of specimens provided desirable results. Of the

welded specimens, the corner spot welded and two-sided seam welded specimens were the least reliable, with each configuration only having yielding four out of seven useful results. All three of the side-slit specimens failed disastrously.

Table 4.8 Successful and failed results summary of different weld types in welded specimens

	4-sided seam	*Corner spots*	*Side spots*	*2-sided seams*	*2 side slits*	*Single tubes*	*Total*
Weld schematic			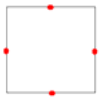			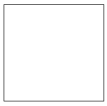	34
Succesful tests (Progressive buckling)	6	4	6	4	0	2	22
Failed tests (Tearing and splitting)	0	3	2	3	3	1	12

As indicated in Table 4.3, two drop heights of 3.26m and 3.6m were used. These drop heights correspond to impact velocities of 8m/s and 8.4m/s, respectively. Figure 4.3 shows original lengths and crushed profiles of 400mm specimens tested at a drop height of 3.26m. Results for these tests are tabulated in Table 4.9. Table 4.9 indicates that the corner spot-welded specimen is the most efficient as it crushed the most but this behaviour was not consistent in other sets tested. Figure 4.4 shows original lengths and crushed profiles of 400mm specimens tested at a drop height of 3.6m. Results for these tests are tabulated in Table 4.10. Although Table 4.8 suggests that the weld type has a significant effect on how the system behaves, from Figure 4.4 and the results in Table 4.10 it is clear that **the weld type makes very little difference to the deformation mode and efficiency in terms of crushed distance in a welded tube. The weld type has a notable effect on a system in terms of the reliability and predictability of the crush mode**. There is only a 5mm difference in crushed distance between the four different welded specimens.

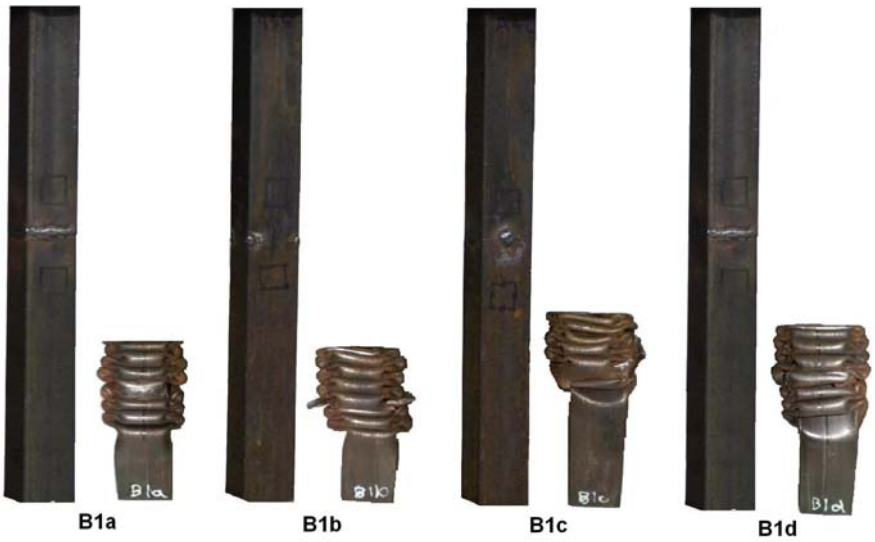

Figure 4.3: 400mm specimens tested with h = 3.26m (50mm clamp length is shown).

Table 4.9 Results of tests performed on 400mm welded specimens with h = 3.26m

Specimen	*Weld type*	*L1 (mm)*	*L2 (mm)*	δ_t *(mm)*	E_{pd} *(kJ)*	P^d_m *(kN)*
B1a		200	200	286	11.82	41.31
B1b		200	200	300	11.87	39.58
B1c		200	200	253	11.71	46.27
B1d		200	200	273	11.79	43.12

Figure 4.4: 400mm specimens tested with h = 3.60m (50mm clamp length is shown).

Table 4.10 Results of tests performed on 400mm welded specimens with h = 3.60m

Specimen	*Weld type*	*L1 (mm)*	*L2 (mm)*	δ_t *(mm)*	E_{pd} *(kJ)*	P^d_m *(kN)*
B2a		200	200	318	13.06	41.00
B2b		200	200	321	13.07	40.73
B2c		200	200	316	13.07	41.30
B2d		200	200	317	13.05	41.07

High-speed camera footage was obtained for some welded specimens. Figures 4.5 - 4.8 show the progressive buckling sequences for specimens B2a, B2b, B2c and B2d respectively. Each frame in a sequence is numbered from (a) to (j) and the corresponding point is shown in the specimen length and axial displacement graph in Figure 4.9. The four specimens display very similar trends in terms of their crushing profiles. The graph shows that all four specimens are crushed by the same amount and that the time taken to stop the drop mass is approximately the same in each specimen (70ms). This in turn indicates that the average deceleration of the impact mass is the same in each specimen. All four specimens decelerated the drop mass by about $110 m/s^2$.

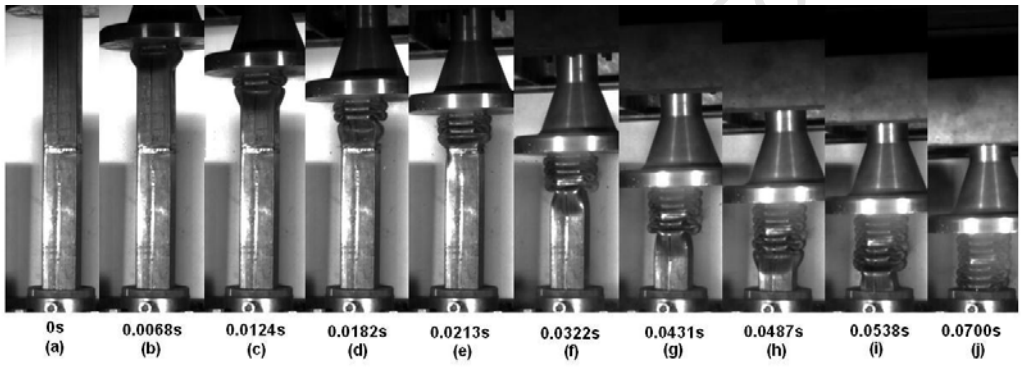

Figure 4.5: Progressive buckling sequence for specimen B2a

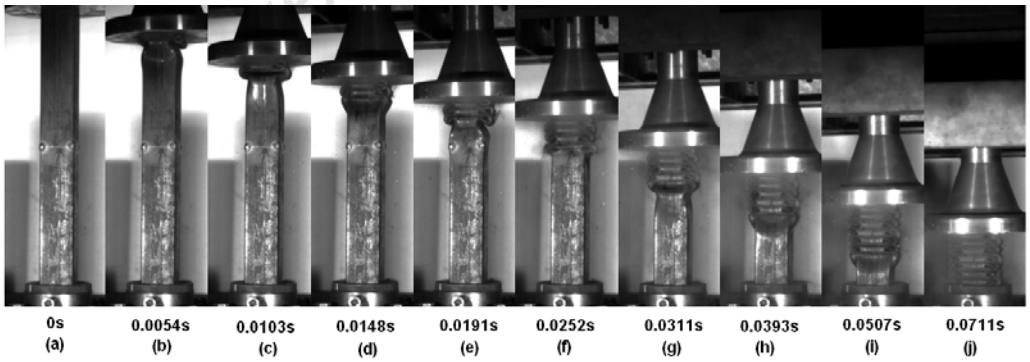

Figure 4.6: Progressive buckling sequence for specimen B2b

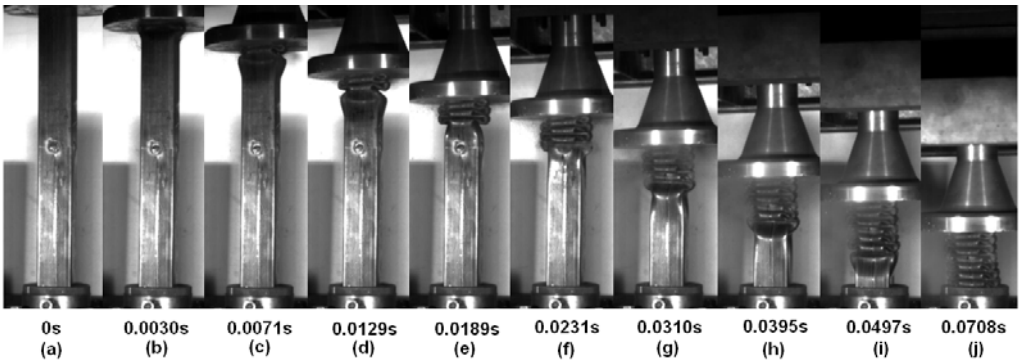

Figure 4.7: Progressive buckling sequence for specimen B2c

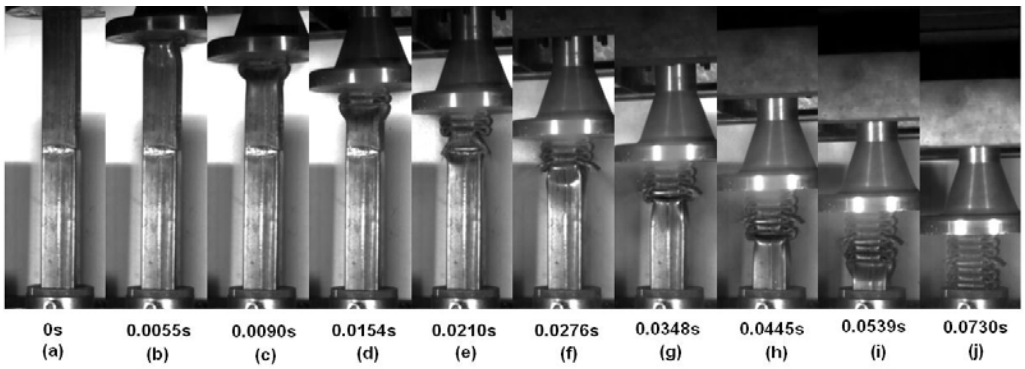

Figure 4.8: Progressive buckling sequence for specimen B2d

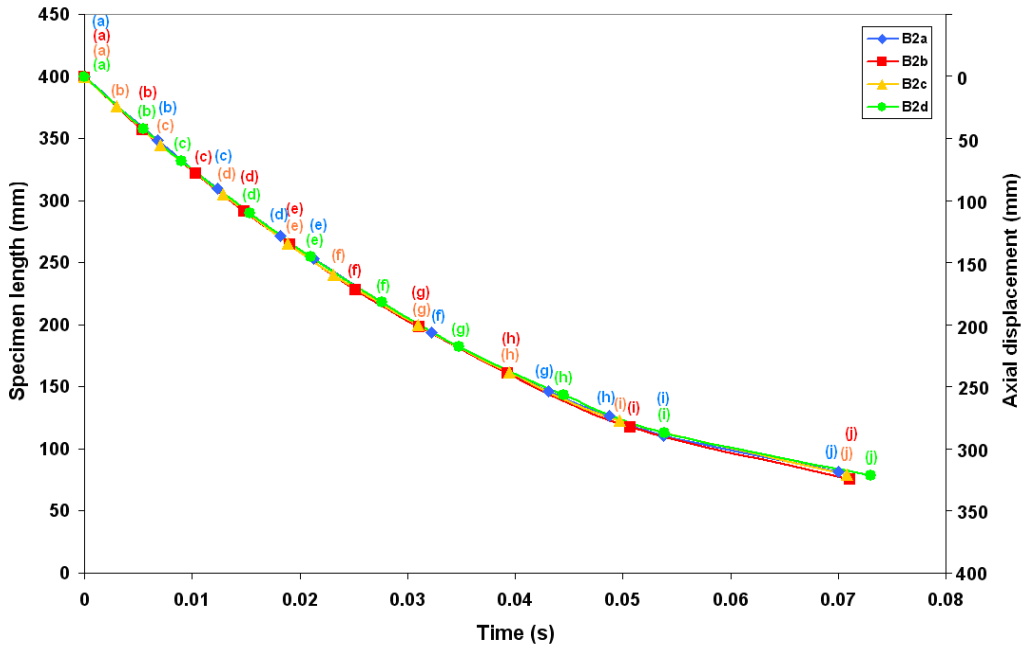

Figure 4.9: Specimen length (left) and axial displacement (right) vs time taken to crush specimen graph for Series B with h=3.6m

Recall that geometric efficiency is a measure of how well an absorber compresses [8] and is given by:

$$e_G = \delta/L \qquad (4.4)$$

where δ is the axial displacement of the tube and L is the original length of the tube. Geometric efficiency has been used for the basis of comparison in this section. Figure 4.10 shows the geometric efficiency chart for specimens tested at a drop height of 3.26m while Figure 4.6 shows the geometric efficiency chart for specimens tested at a drop height of 3.60m.

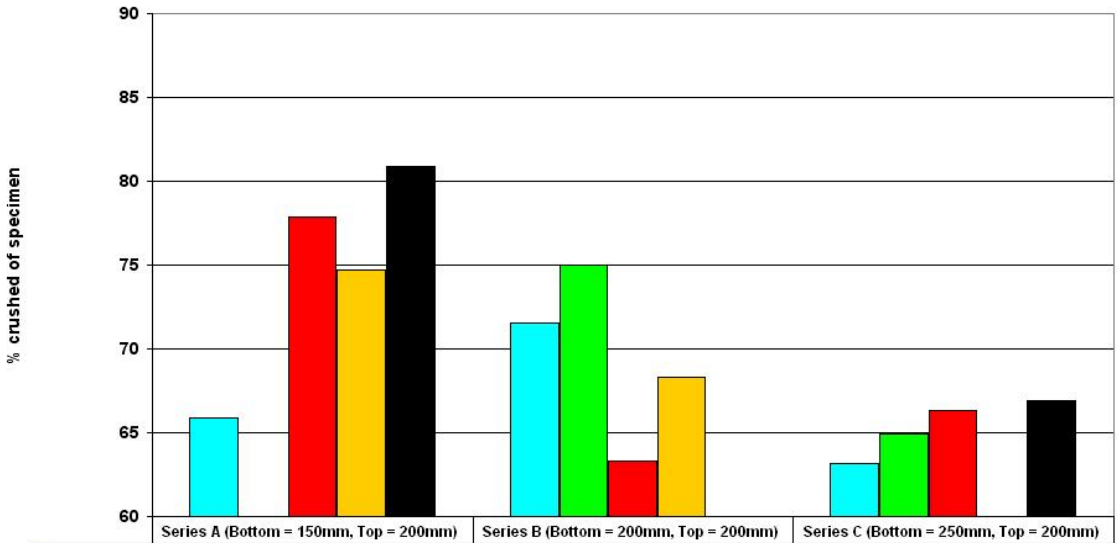

	Series A (Bottom = 150mm, Top = 200mm)	Series B (Bottom = 200mm, Top = 200mm)	Series C (Bottom = 250mm, Top = 200mm)
4 sided seem	65.86	71.55	63.15
corner spots		74.98	64.93
Side spots	77.85	63.29	66.30
2 sided seem	74.73	68.33	
Single tube	80.91		66.89

Figure 4.10 Geometric efficiencies of specimens tested with h = 3.26m.

The graph in Figure 4.10 shows that at a drop height of 3.26m, specimens in series A and B exhibit a fairly large difference in terms of geometric efficiency. In series A there is a difference of 15% between the four-sided seam weld specimen and the single tube specimen. In series B there is a 12% difference between the corner spot weld and the side spot weld specimens. However, there is no consistency in terms of

which weld is more efficient in Series A and B. In series C however, the specimens have very similar geometric efficiencies with the single tube only being 3.5% more efficient than the least efficient specimen (four-sided seam weld) in the series.

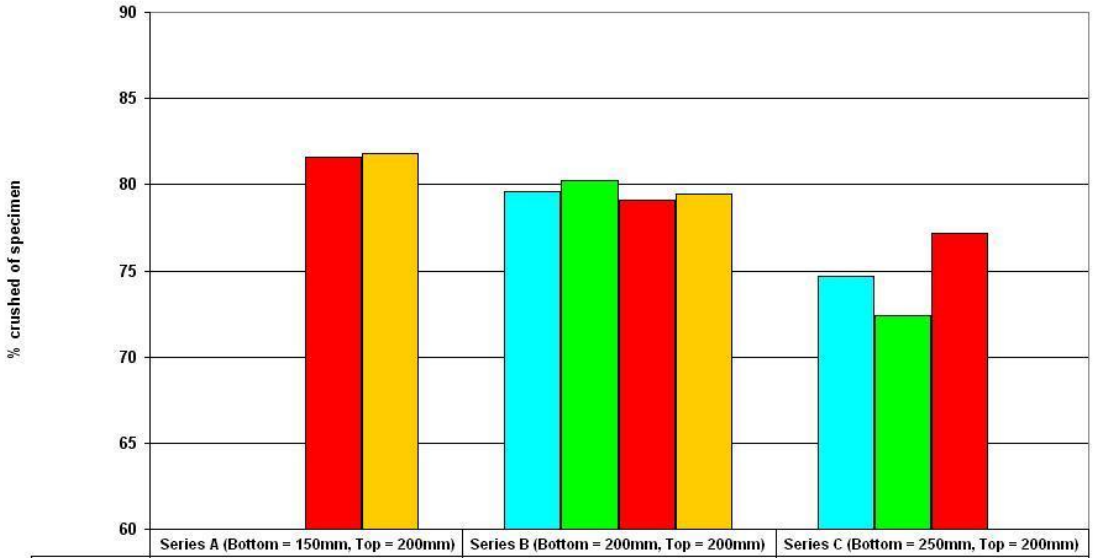

	Series A (Bottom = 150mm, Top = 200mm)	Series B (Bottom = 200mm, Top = 200mm)	Series C (Bottom = 250mm, Top = 200mm)
4 sided seam		79.60	74.66
corner spots		80.22	72.39
side spots	81.62	79.10	77.20
2 sided seam	81.81	79.47	

Figure 4.11 Geometric efficiencies of specimens tested with h = 3.60m.

At a drop height of 3.60m, the graph in Figure 4.11 shows that in all three series, the differences in geometric efficiencies between each weld type specimen is much smaller. Series B has a difference of less than 1% between the four weld types tested in that series. Single tubes were not tested at this drop height. These results show that **there is no superior weld type in terms of geometric efficiency but that in terms of reliability (least failures), the four sided seam weld performed best.**

4.2 Quasi-Static Axial Crushing Results

19 quasi-static crushing tests were performed. Of these, one of them did not yield useful data, while 18 of them provided successful results. The specimens were all crushed at the same cross-head speed and by 73% of their original lengths, the effective crushing distance for symmetric crushing of a square tube [2]. The symmetric mode of crushing was observed in all specimens that underwent progressive buckling. The results are presented in Table 4.11.

Table 4.11 Results of quasi-static tests (with *chs*=10 mm/min, $\dot{\varepsilon}$ =1.1 × 10^{-3} s^{-1}, $P_{m\ (theoretical\ [2])}$=34.53 kN)

Specimen	P_m *(kN) exp*	P_{ult} *(kN)*	*δ (mm)*	*δ (%)*	*Buckling mode and number of lobes*
400s	28.21	88.90	247	61.25	S (12)
200w200	27.48	88.75	290	72.50	S (14)
200p200	29.03	86.37	290	72.50	[S (7)] [A (2)-S (5)]
500s	28.94	87.45	360	72.00	S (16)
250w250	28.18	90.02	360	72.00	S (17)
250p250	27.32	85.63	360	72.00	[S (8)] [S (8)]
600s	29.12	96.91	435	72.50	S (19)
300w300	26.86	92.01	435	72.50	S (19)
300p300	31.19	103.16	435	72.50	[S (9)] [S (10)]
700s	29.22	96.29	505	72.14	S (23)
350w350	28.22	85.17	505	72.14	S (23)
350p350	29.72	91.56	505	72.14	[S (10)] [S (12)]
750s	30.55	107.81	545	72.67	S (24)
375w375	-	89.71	545	72.67	G
375p375	-	95.39	545	72.67	G
800s	-	108.72	580	72.50	G
400w400	-	85.89	580	72.50	G
400p400	-	94.69	580	72.50	G

Notation used in Table:

A	**Asymmetric**	**( )**	**Number of complete lobes**
G	**Global bending**	**[ ] [ ]**	**Bottom and top lobe description, respectively**
S	**Symmetric progressive**		
s	**Single tube specimen**		
w	**welded tubes specimen**		
p	**plate-divided tubes specimen**		

Crushing of specimen 400s ended prematurely due to an error in the initial setup parameters of the software program and therefore crushed less than desired. The same number of lobes and crush modes were observed for all specimens; be it single, welded or plate-divided. Specimen 750s buckles progressively while its welded and plate divided equivalents, 375w375 and 375p375, deform by global bending. It is clear that at 750 mm the buckling mode changes from progressive to global bending. No transition buckling occurred in any of the quasi-static tests performed. This is consistent with experimental findings from Abramowicz et al. [12]. Another point of interest in Table 4.11 is that the mean load P_m for the plate-divided specimens is higher than the single and welded equivalents for the 400mm, 600mm and 700mm long specimens. This is expected since the plate-divided specimens yield two peak ultimate forces as each of the two tubes making up a specimen crush independently.

Figures 4.12a, 4.13a, 4.14a, 4.15a, 4.16a and 4.17a illustrate the comparative axial force versus axial displacement graphs of the 400mm, 500mm, 600mm, 700mm, 750mm, and 800mm specimens, respectively. Following each of these graphs are figures of the progressive buckling of the specimens. In the plate-divided specimens, each of the two tubes making up the specimen is shown crushing separately. The horizontal dashed lines in each axial force-axial displacement graph indicate the mean load P_m of the specimens. Each axial load-axial displacement graph and its corresponding progressive buckling image are lettered in small case letters to indicate the corresponding position of the deformed tube on its load-displacement graph.

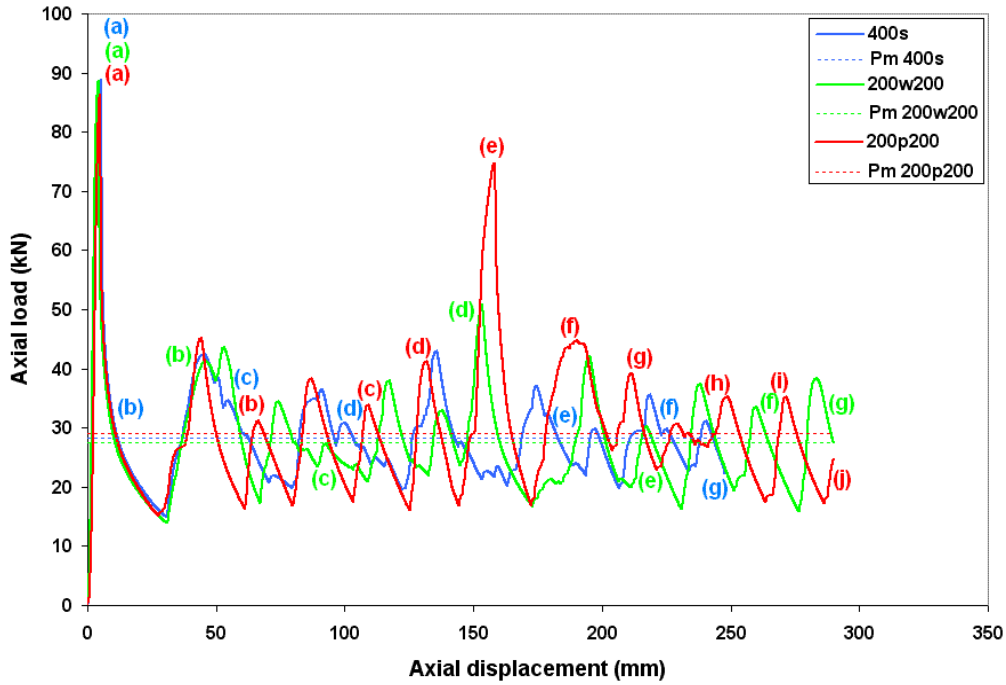

Figure 4.12a: Axial load vs axial displacement graph for 400mm specimens.

Figure 4.12a shows that the initial peaks of the three 400mm specimens are in the same region just below 90kN. Subsequent peaks and valleys overlap along the axial displacement axis and have similar magnitudes. A noticeable feature is the secondary ultimate peak that arose in 200p200. This is as a result of the second tube of the specimen beginning to buckle. This secondary ultimate peak is of similar magnitude to the initial ultimate peaks. The mean axial load of 200p200 is slightly higher than the other two specimens because of this secondary force.

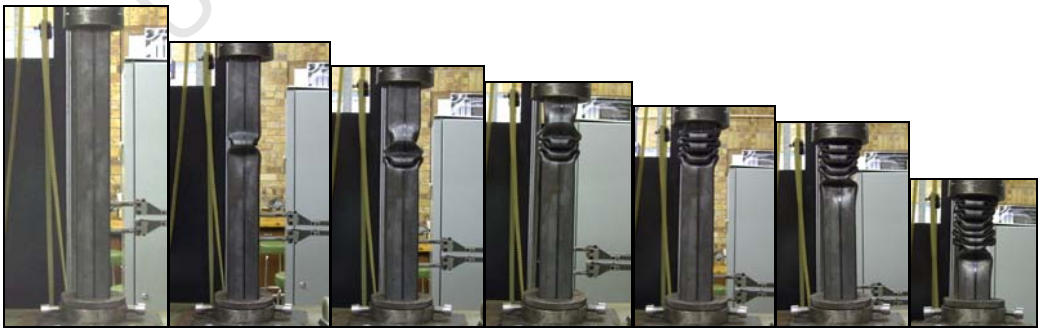

Figure 4.12b: Progressive buckling of specimen 400s.

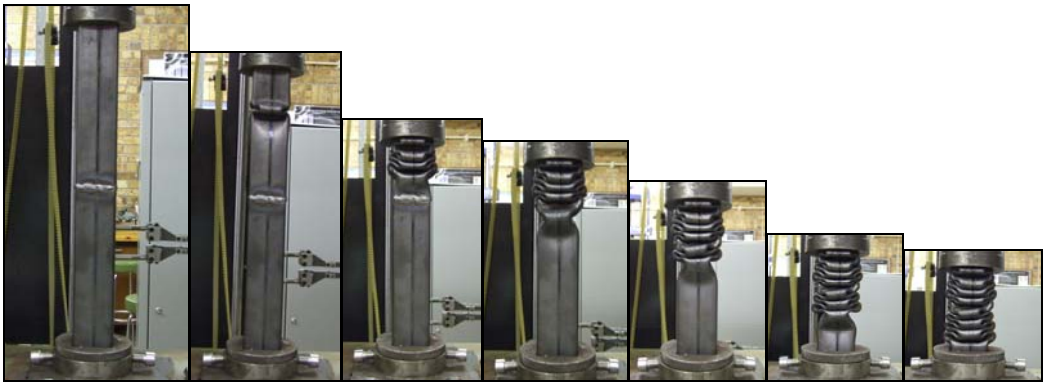

(a) (b) (c) (d) (e) (f) (g)

Figure 4.12c: Progressive buckling of specimen 200w200.

Figure 4.12b shows that the single tube specimen 400s started to buckle close to halfway along the specimen. Similarly to 400s, 200w200 began buckling along the upper half in the top tube of the specimen as shown in Figure 4.12c. The specimen continued to buckle irrespective of the presence of the weld and the weld becomes integrated into the folding mechanism.

In specimen 200p200 (Figure 4.12d), buckling initiated at the bottom of the specimen in the bottom tube. The bottom tube crushed to a maximum up until the plate and then crushing initiated in the top tube. The top tube started buckling at the top by asymmetric mixed mode buckling which then changed to symmetric buckling by the third layer of lobes. The rigid plate retained its original shape with no visible distortion.

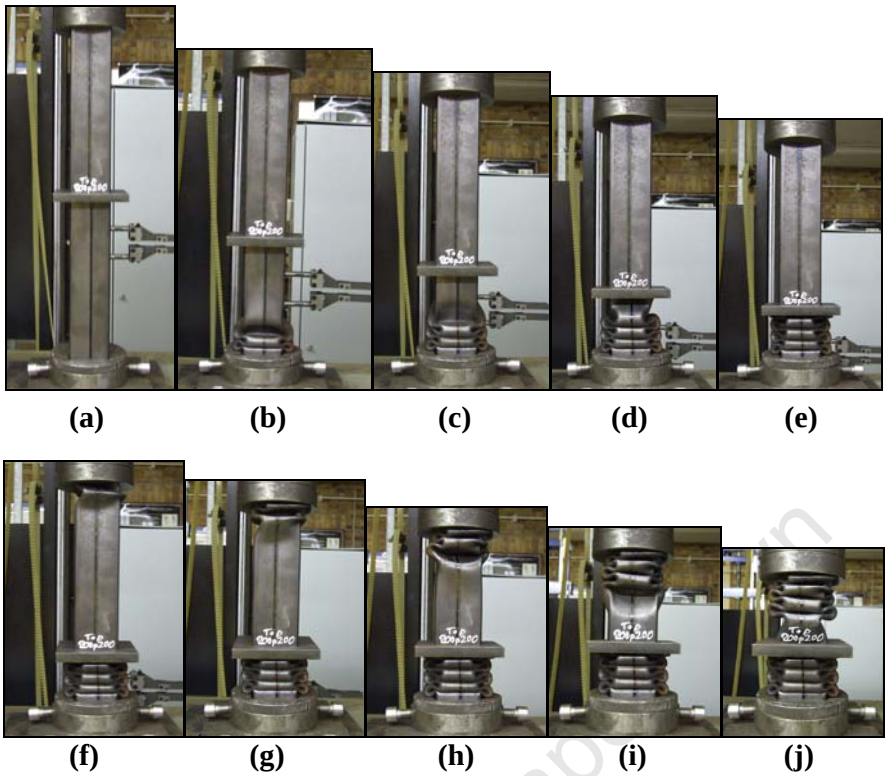

Figure 4.12d: Progressive buckling of specimen 200p200.

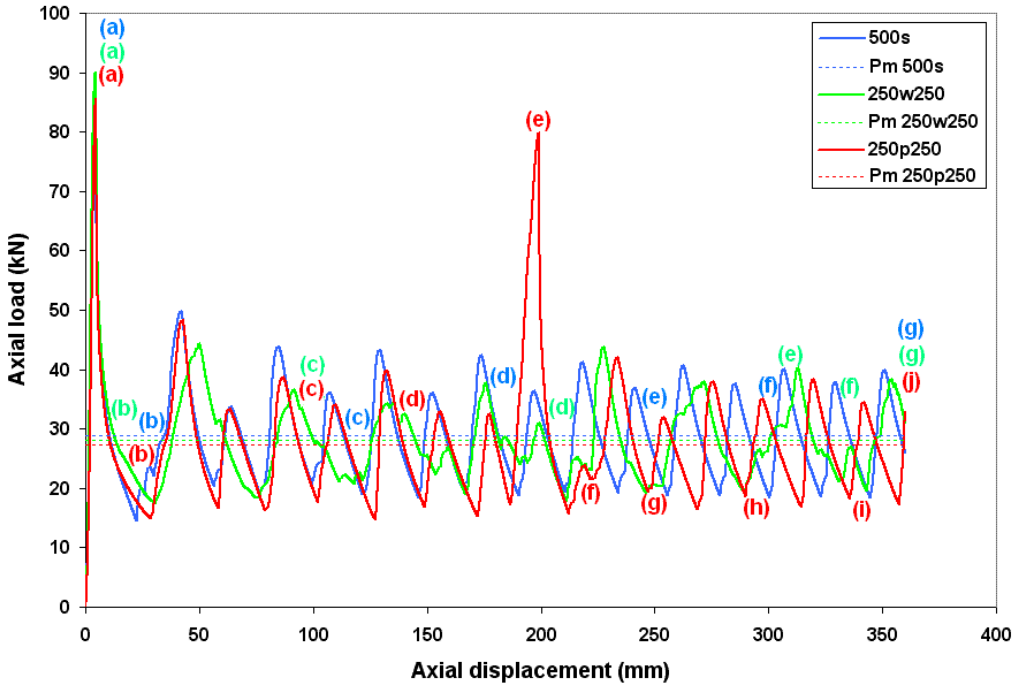

Figure 4.13a: Axial load vs axial displacement graph for 500mm specimens.

Figure 4.13a shows that the initial peaks of the three 500mm specimens are also in the region 90kN. Up to a displacement of 180mm, the single tube 500s and the plate divided tube 250p250 exhibit very similar behaviour with lobes forming at almost the same axial displacement, as can be seen on the axial load-displacement profiles. Again a secondary peak arose in the plate-divided specimen 250p250 with a similar magnitude to the initial peak. The mean axial load of 250p250 is lower than that of the single and welded specimens. This behaviour is inconsistent with the trend observed in all other quasi-static tests in which the mean axial load of the plate-divided specimen was higher than in the single and welded specimens.

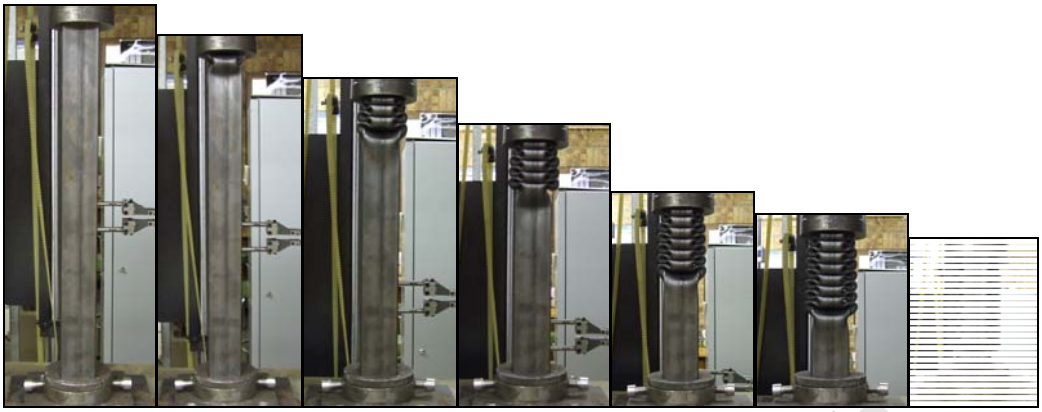

Figure 4.13b: Progressive buckling of specimen 500s.

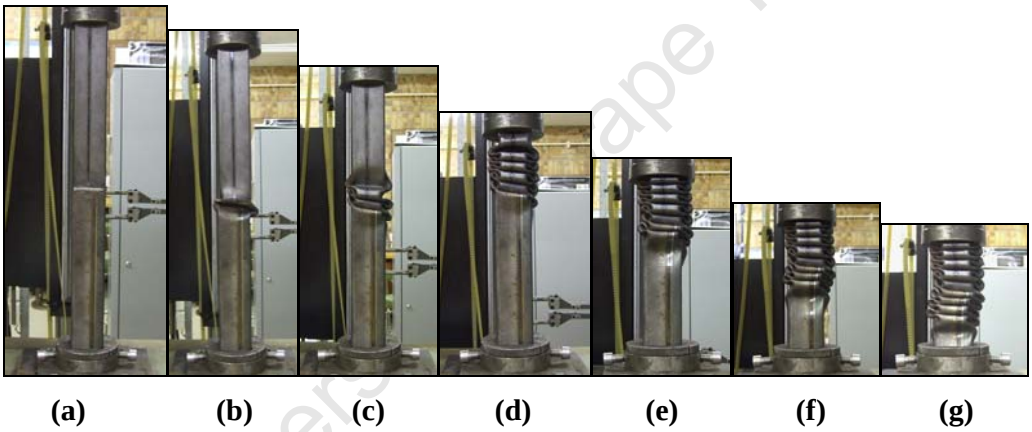

Figure 4.13c: Progressive buckling of specimen 250w250.

Specimen 500s initiated buckling at the top of the specimen as shown in Figure 4.13b and buckled in a very symmetrical manner. Lobe formations in specimen 250w250 started at the weld and although symmetric buckling was observed, the lobes were slightly skew, which also explains the somewhat irregular load-displacement profile in Figure 4.13a.

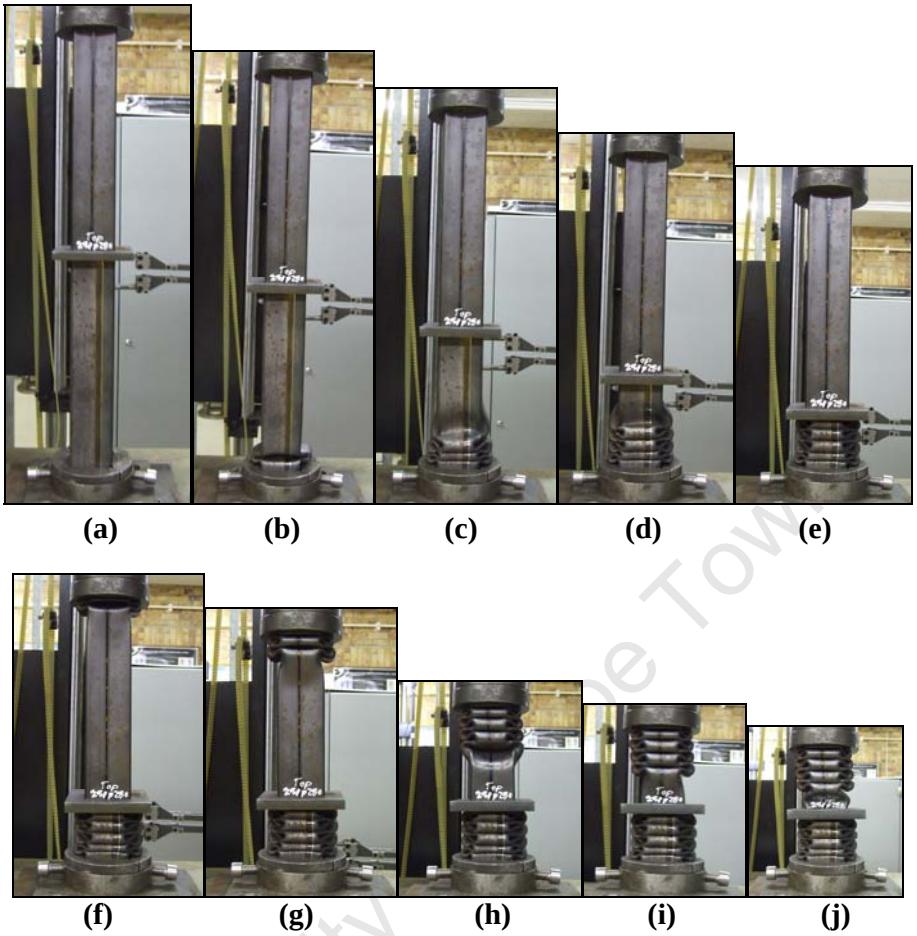

Figure 4.13d: Progressive buckling of specimen 250p250.

As was observed in the 200p200, specimen 250p250 behaved in a similar manner. The bottom tube was the first to start buckling at the bottom, followed by the top tube crushing at the top.

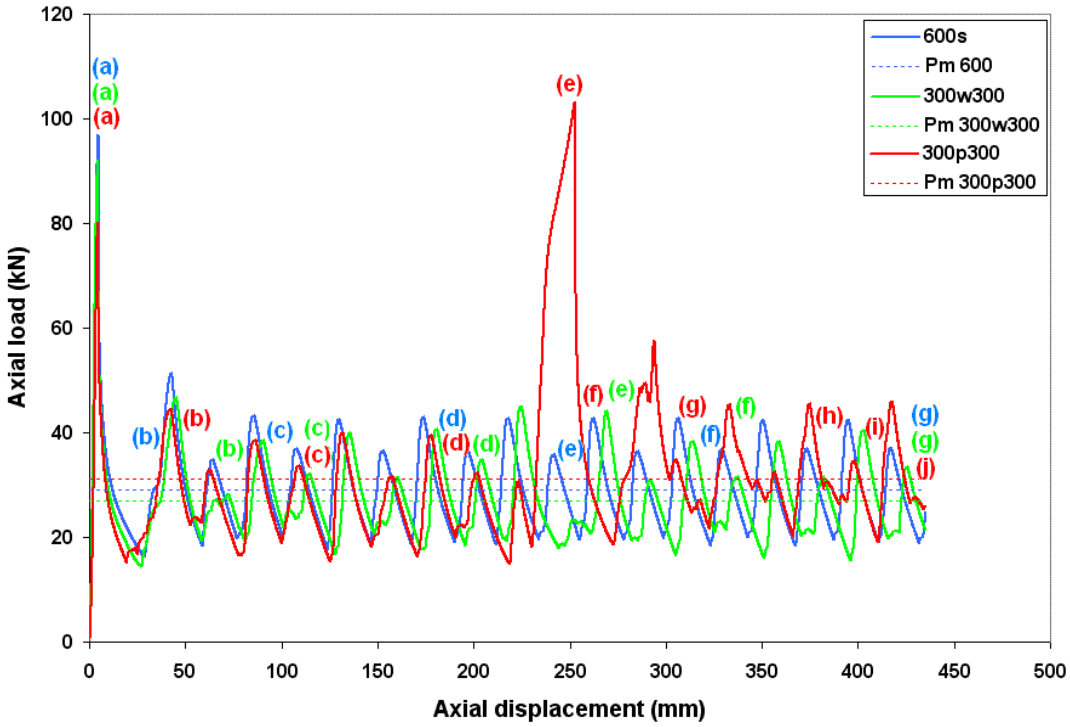

Figure 4.14a: Axial load vs axial displacement graph for 600mm specimens.

The trends observed in the 400mm and 500mm specimens continued in the 600mm specimen in terms of load-displacement profiles as shown in Figure 4.14a. Notably, however, is the secondary ultimate peak in specimen 300p300 is about 30kN higher than the first peak and is the maximum load of the entire specimen. Again, as seen in the 400mm specimens, the plate divided specimen 300p300 has a higher mean load than the single and welded specimens.

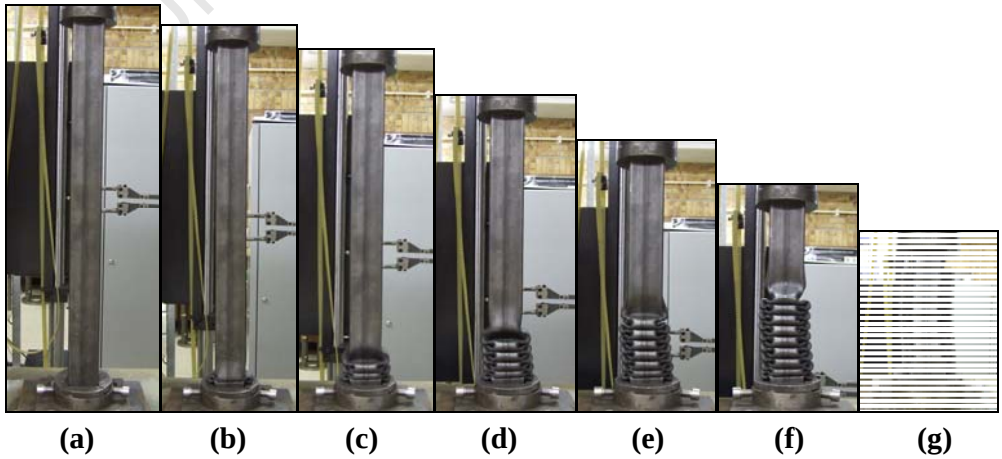

Figure 4.14b: Progressive buckling of specimen 600s.

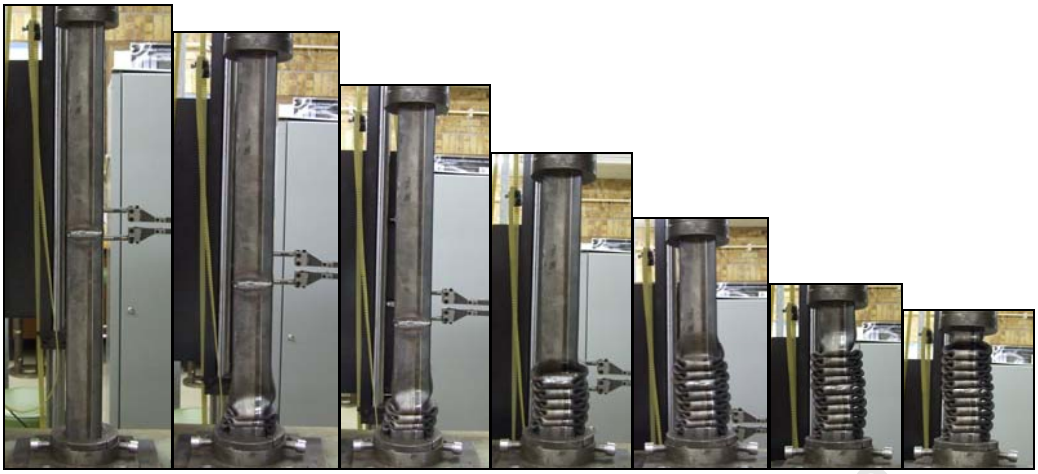

(a) (b) (c) (d) (e) (f) (g)

Figure 4.14c: Progressive buckling of specimen 300w300.

Buckling in specimen 600s initiated at the bottom as shown in Figure 4.14b, different to what was seen in 400s and 500s. 300w300 behaved very similarly with buckling occurring at the bottom of the specimen as shown in Figure 4.14c. Both specimens formed 19 layers of symmetrical lobes.

In the plate divided specimen 300p300, lobe formation started at the very top of the top tube opposed to what was observed in 200p200 and 250p250. Once the top tube was crushed to a maximum, the bottom tube started buckling at the top near the plate as shown in Figure 4.14d.

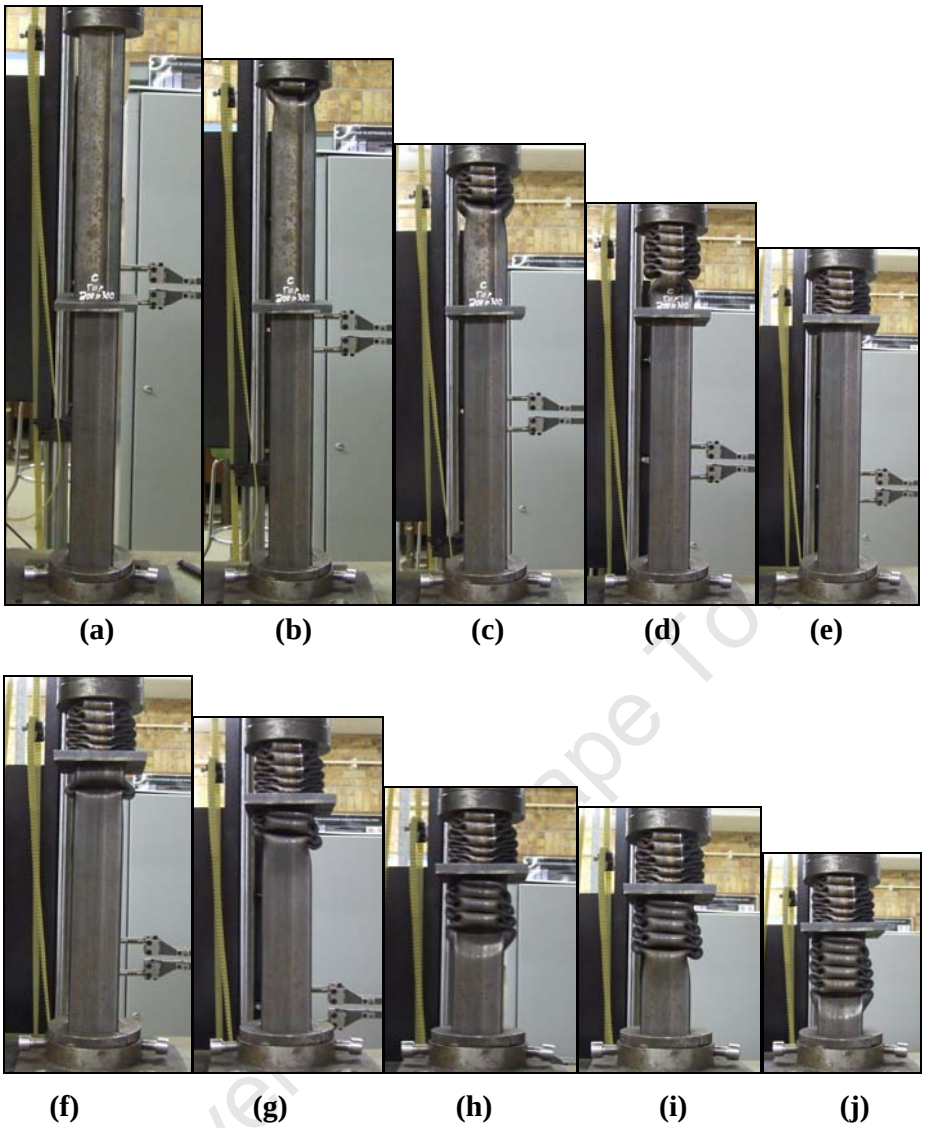

(a) (b) (c) (d) (e)

(f) (g) (h) (i) (j)

Figure 4.14d: Progressive buckling of specimen 300p300

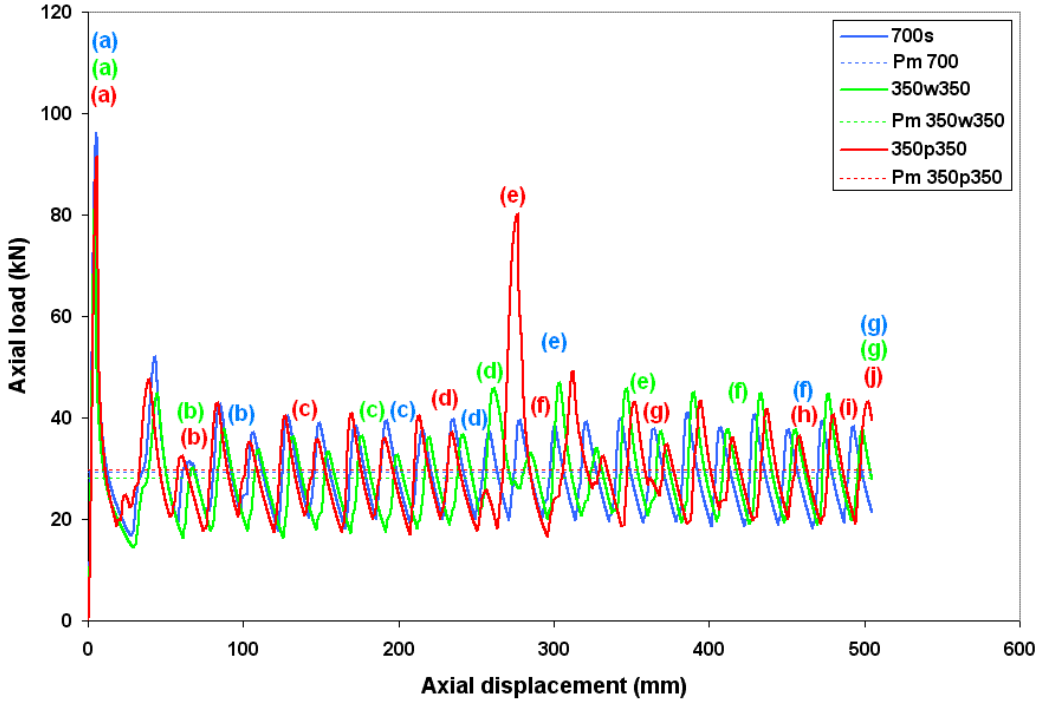

Figure 4.15a: Axial load vs axial displacement graph for 700mm specimens.

The axial load-displacement graph for the 700mm specimens in Figure 4.15a exhibits similar features to aforementioned load displacement graphs with the characteristic secondary ultimate peak revealing itself in the plate divided specimen 350p350 and the slightly higher mean load for that specimen.

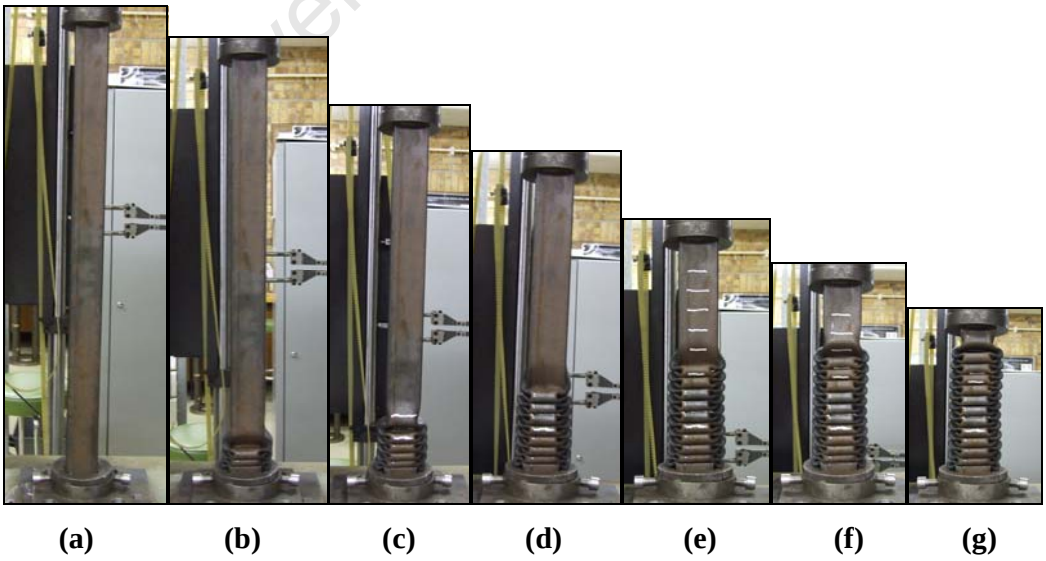

Figure 4.15b: Progressive buckling of specimen 700s.

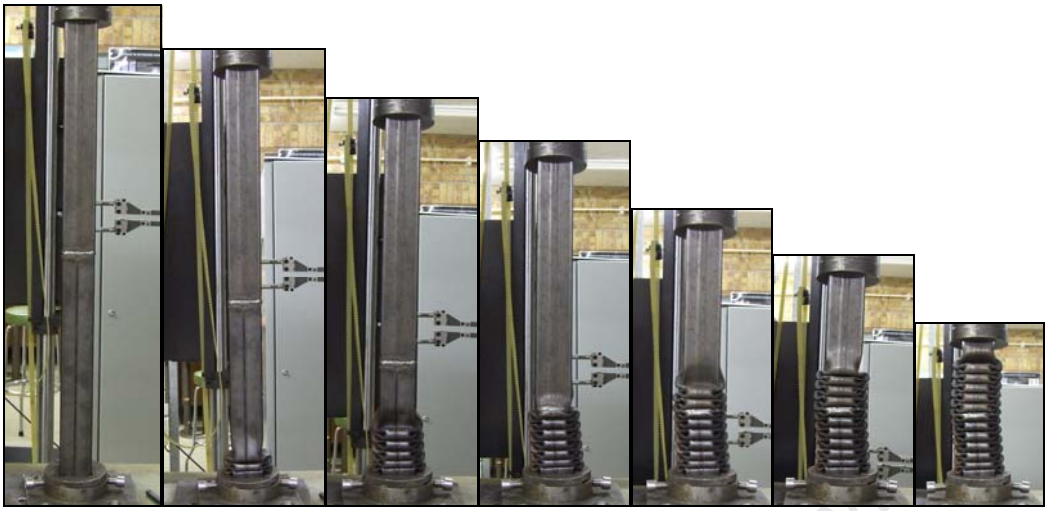

Figure 4.15c: Progressive buckling of specimen 350w350.

Specimen 700s and 350w350 buckle similarly with buckling initiating at the bottom of each specimen as shown in Figures 4.15b and 4.15c respectively. 23 layers of lobes formed in both specimens.

In the plate divided specimen 350p350, buckling initiated in the top tube but on this occasion at the plate as shown in Figure 4.15d. Thereafter, the bottom tube crushed from the top down. There seems to be no consistency in the initial formation of lobes in plate divided specimens.

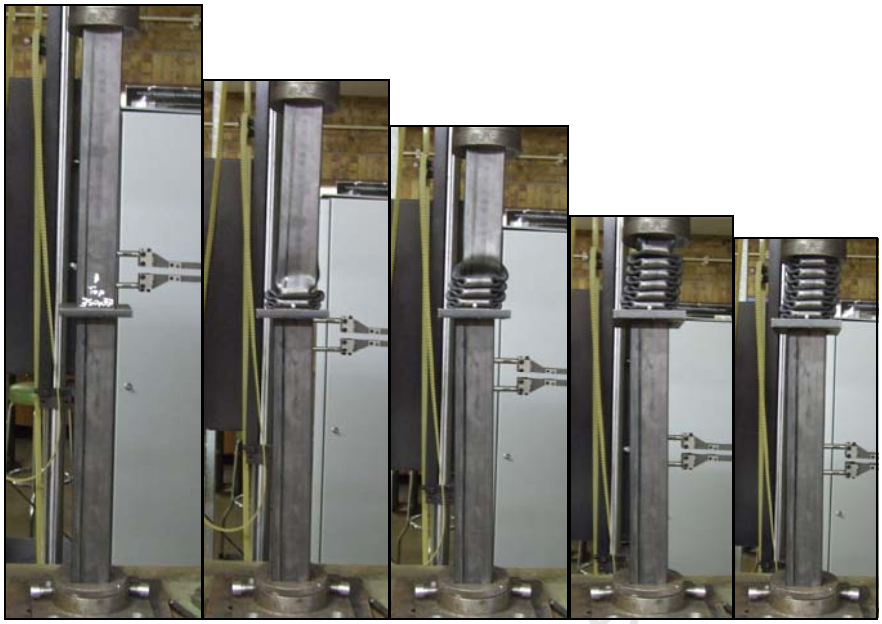

(a) **(b)** **(c)** **(d)** **(e)**

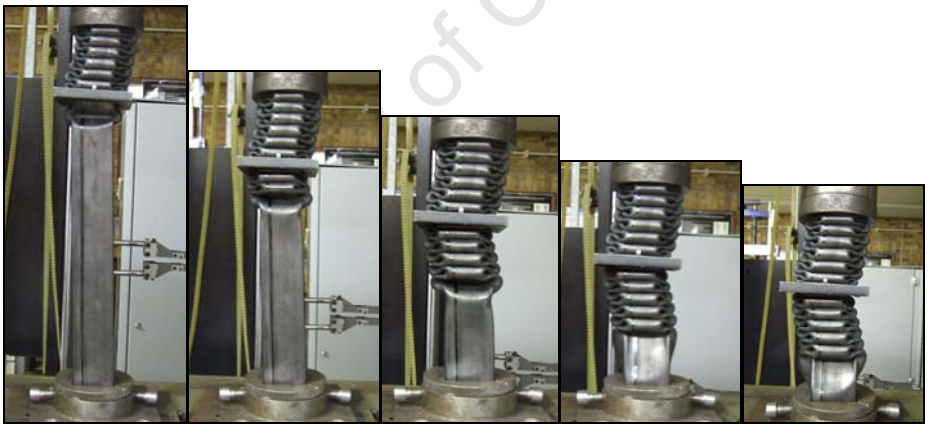

(f) **(g)** **(h)** **(i)** **(j)**

Figure 4.15d: Progressive buckling of specimen 350p350.

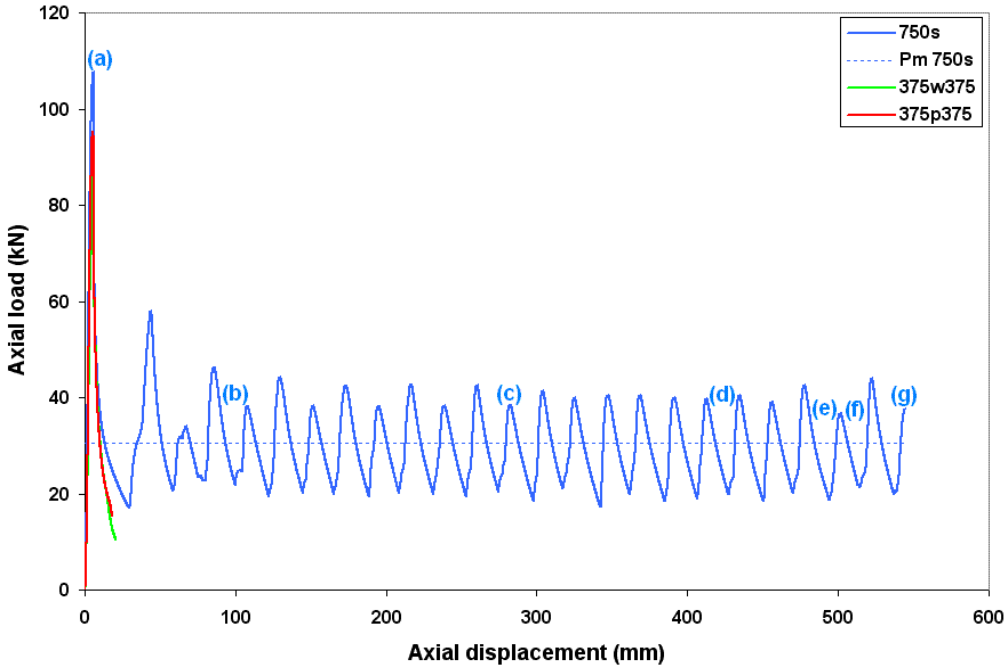

Figure 4.16a: Axial load vs axial displacement graph for 750mm specimens.

The 750mm specimens provided definitive results in that the boundary from progressive buckling to global bending could be ascertained. While the single tube specimen 750s buckled in the characteristic progressive manner, specimens 375w375 and 375p375 experienced global bending.

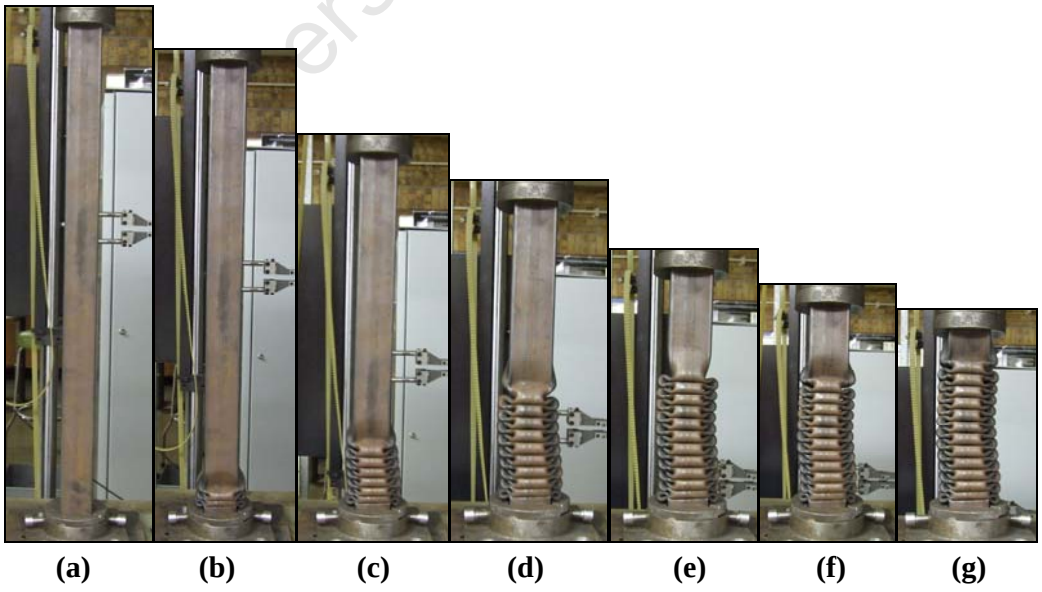

Figure 4.16b: Progressive buckling of specimen 750s.

Figure 4.16b shows the progressive buckling which occurred in 700s while Figures 4.16c and 4.16d reveal global bending in 375w375 and 375p375, respectively. In 375w375, buckling occurred at the weld while in 375p375, buckling occurred just above the plate.

Figure 4.16c: Global bending of specimen 375w375 and (x) close-up showing position of buckling.

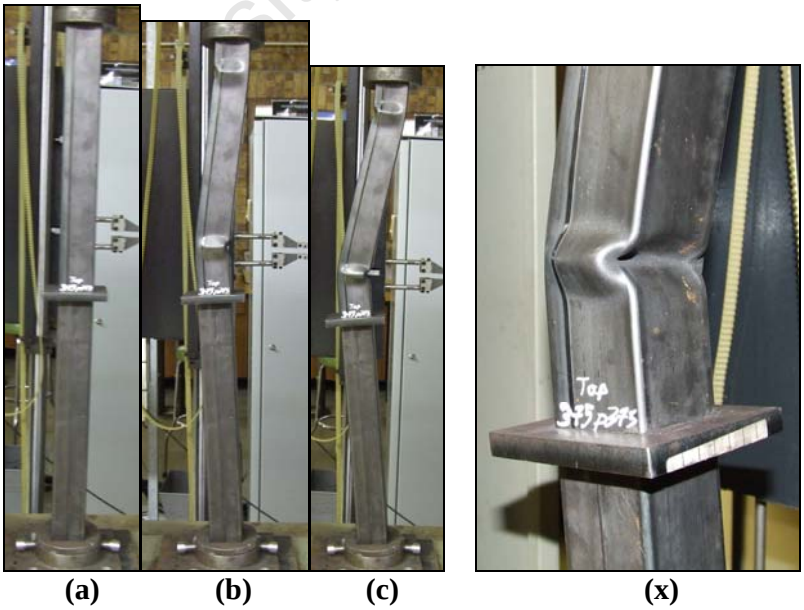

Figure 4.16d: Global bending of specimen 375p375 and (x) close-up showing position of buckling.

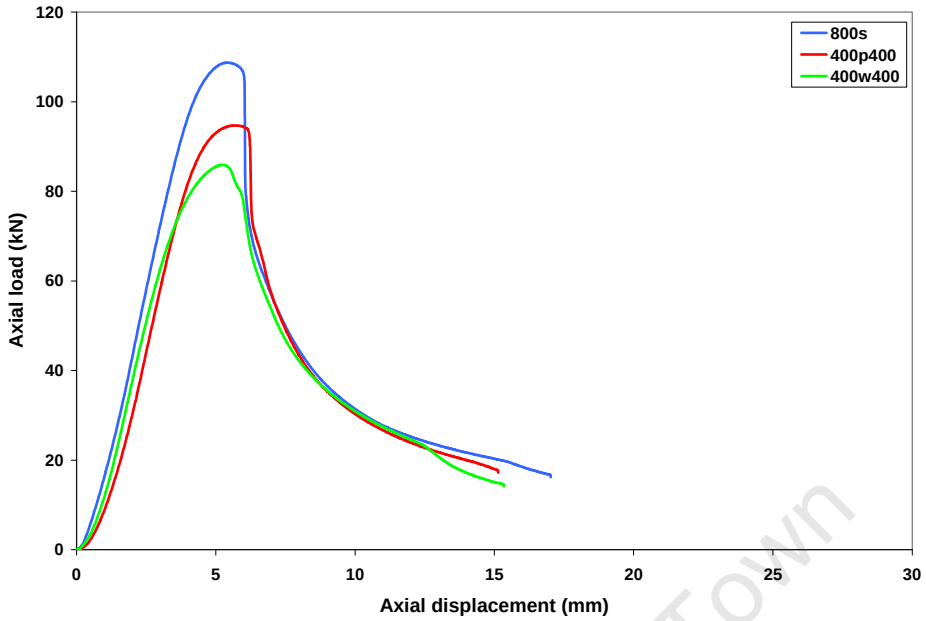

Figure 4.17a: Axial load vs axial displacement graph for 800mm specimens

In the 800mm specimens, global bending occurred in all three specimens. The peak loads differed considerably in the three specimens as shown in Figure 4.17a. Tests were terminated early as to avoid damage to test equipment. Figure 4.17b shows the three specimens after testing and the close-up of were buckling occurred.

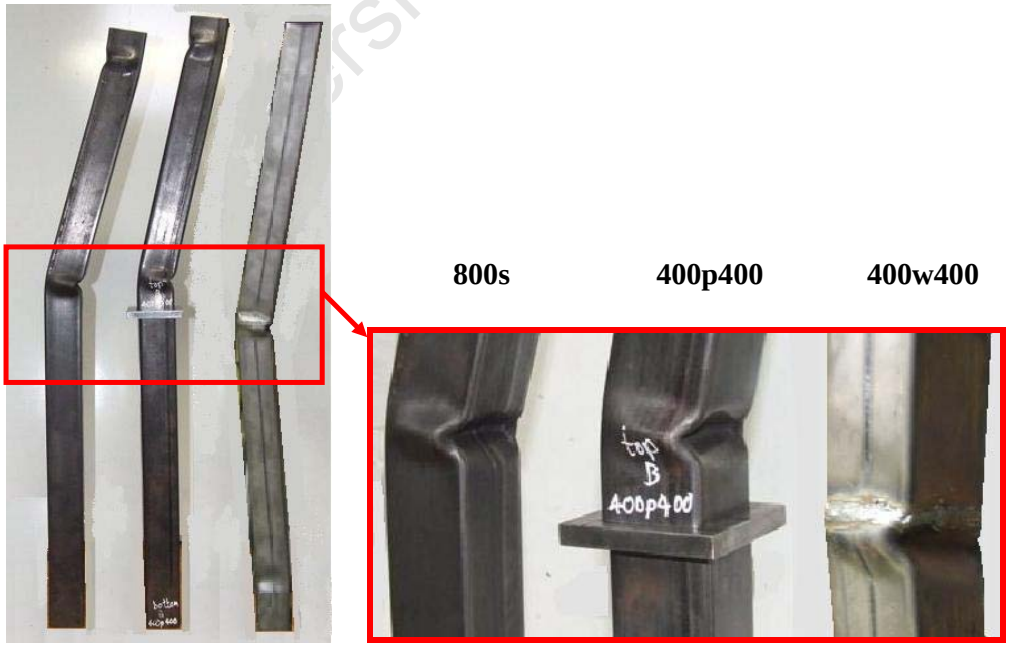

Figure 4.17b: Global bending of 800mm specimens

4.3 Dynamic Axial Crushing Results of Group C

Section 4.1 describes the splitting up of dynamic tests into Group A, Group B and Group C and tabulates the results for these specimens, as well as briefly explaining results obtained from Group A and B. In this section, results of Group C tests are explained in more detail with reference to Table 4.4 and Table 4.5.

4.3.1 Progressive Buckling of Single and Welded Tube Specimens

Table 4.4 summarises results performed on Group C single and welded tubes with lengths of 300mm, 400mm and 500mm. 24 tests were performed; 12 on single tube specimens and 12 on welded specimens. The welded specimens consisted of two tubes welded together at their ends such that the weld was half way along the specimen (not including the 50mm allowed for clamping).

Table 4.4 and Figure 4.18 show that single tubes crushed more than welded equivalents in all tests performed with 300mm specimens at drop heights of 3.26m, 2.68m, 2.15m and 1.69m. The seam weld did not inhibit lobe formation but caused the specimens to crush less than their single tube counter-parts because the lobe that formed over the weld in each case was used slightly more of the material to form. Specimen 300sA and its welded equivalent 150w150A only had a difference in crush difference of 5mm. Specimens 150w150C and 150w150D exhibited asymmetric buckling in initial lobe formation and then continued to crush symmetrically. All other tubes buckled symmetrically. Figure 4.18 shows the specimen length on the left and the crushed distance on the right.

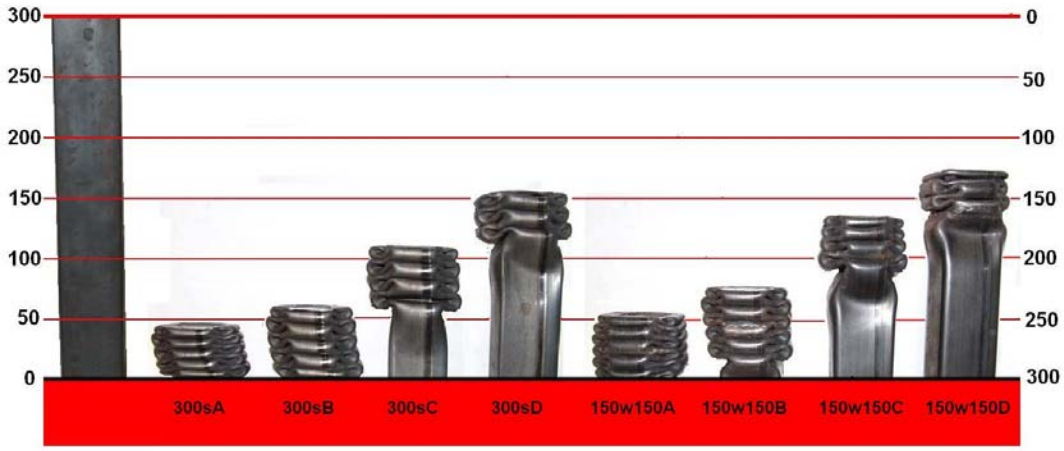

Figure 4.18: Progressive buckling of 300mm single tube specimens and welded equivalents at drop heights of 3.26m, 2.68m, 2.15m and 1.69m respectively.

400mm specimens exhibited similar trends to those seen in the 300mm specimens. Tests were performed with drop heights of 3.9m, 3.26m, 2.68m and 2.15m. Again, the welded specimens were crushed by less than the single tube equivalents but the differences were much smaller as can be seen from Table 4.4 and Figure 4.19. Specimens 400sC and 200w200C only had a difference of 4mm in their crush lengths. All eight tubes tested buckled symmetrically.

Figure 4.19: Progressive buckling of 400mm single tube specimens and welded equivalents at drop heights of 3.9m, 3.26m, 2.68m and 2.15m respectively.

Tests performed with 500mm specimens once again showed that single tube specimens crushed slightly more than the welded equivalents. Tests were performed

at drop heights of 3.26m, 2.68m and 2.15m. Specimen 500sC, 500sD, 250w250C and 250w250D were tested with the same drop height. As can be seen in Figure 4.20, 250w250C buckling initiated at the weld half way along the specimen and for this reason a retest in the form of 250w250D was performed. Specimens 500sD and 250w250D were crushed by exactly the same amount of 165mm.

Figure 4.20: Progressive buckling of 500mm single tube specimens and welded equivalents at drop heights of 3.26m, 2.68m and 2.15m (twice) respectively.

4.3.2 Dynamic Tests in Transition and Global Bending Region

Table 4.5 summarises results performed on Group C single, welded and plate-divided specimens with lengths ranging from 550mm to 1700mm. Every test was performed at a drop height of 3.26m corresponding to an impact velocity of 8m/s. 50 tests were performed and these tests were considered the main focus of this thesis. Of these 50 tests, 7 of the specimens buckled in the transition mode (characterised by progressive buckling and ultimately global bending) while only one specimen experienced global bending. Most specimens buckled progressively while others, although deformed progressively, could be seen to be on the verge of the transition region. This will be highlighted later in this chapter.

The 550mm specimens were tested first. The single tube buckled progressively but buckling initiated at the bottom of the tube just above the clamp as can be seen in Figure 4.21. The specimen deformed by 178mm. the welded specimen 275w275A buckled in the transition mode with some lobe formation followed by global bending. A retest was then performed in the form of 275w275B. This specimen deformed in a symmetric progressive manner by 200mm with lobe formation initiating at the top of the specimen. The plate-divided specimen 275p275 also buckled in a symmetric progressive manner and also deformed by 200mm. In this specimen, however, lobe formation initiated at the bottom of the top tube.

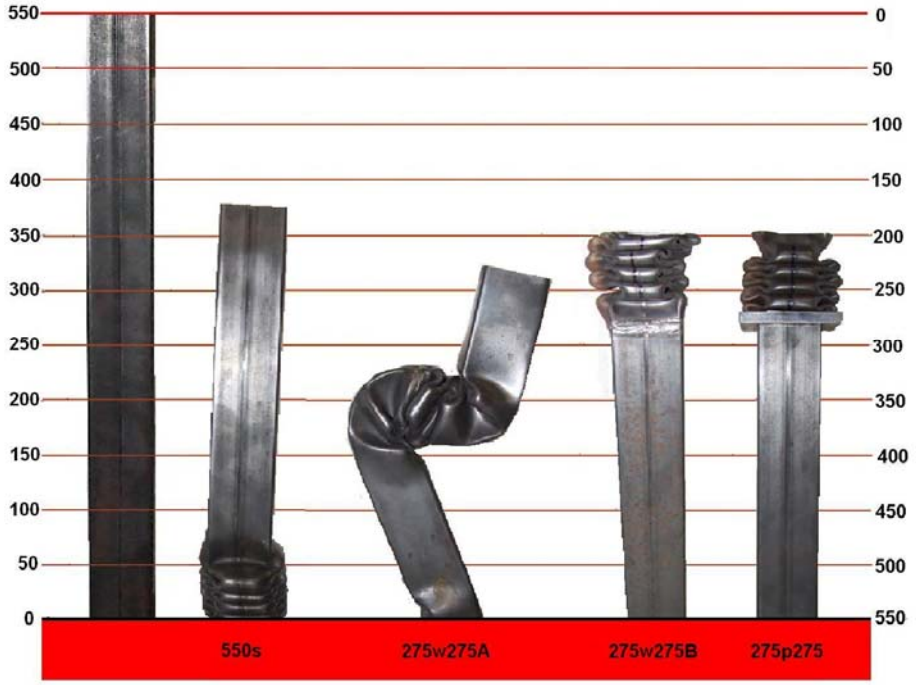

Figure 4.21: Buckling profiles of 550mm specimens. The tube on the left shows the original length of the specimen.

In the 600mm specimens, the single tube 600sA buckled in the transition mode as shown in Figure 4.22. Its retest 600sB buckled progressively by 156mm but in an irregular manner as can be seen by the close up in Figure 4.22a. The welded specimen 300w300A formed symmetric lobes but interestingly one layer of lobes formed at the bottom near the clamp as shown in Figure 4.22b while the rest formed at the top. Furthermore, the skew shape of the specimen suggests that continued crushing may have caused it to buckle in the transition mode. A retest of the welded specimen was performed in the form of 300w300B. This specimen buckled in a symmetric progressive manner. The plate-divided specimen also buckled in this way. The two welded specimens and the plate-divided specimens deformed by similar amounts, namely 192mm, 187mm and 190mm, respectively.

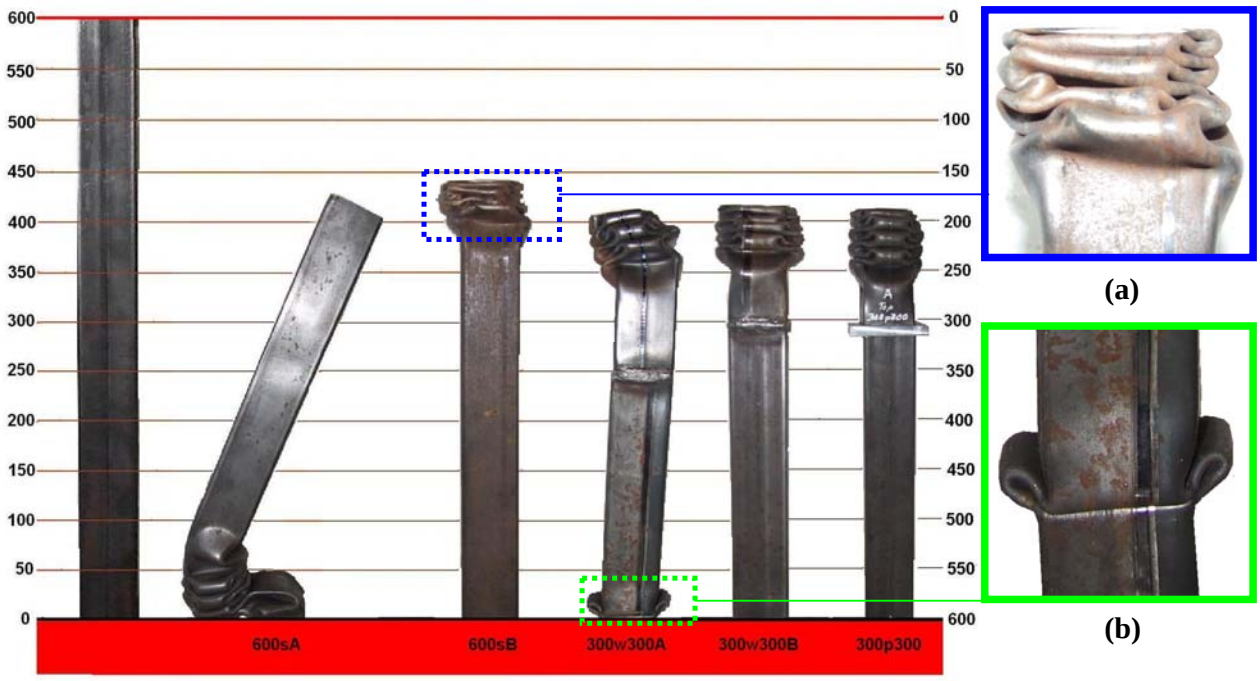

Figure 4.22: Buckling profiles of 600mm specimens with close ups of (a) 600sB and (b) 300w300A.

650mm specimens behaved similarly to 600mm specimens. Again the single tube specimen (650sA) deformed by transition buckling as shown in Figure 4.23. A retest (650sB) faired better by symmetric progressive buckling with a final crush distance of 185mm. The welded specimen 325w325 buckled progressively but lobe formation initiated at the weld and continued in the bottom half of the specimen as shown in the close up in Figure 4.23a. In the plate-divided specimen 325p325A progressive buckling occurred but transition buckling would probably have occurred if the specimen was deformed further. This can be seen in the close up in Figure 4.23b by the global bending that had just started at the end of the test in the bottom of the specimen. A retest 325p325B was performed and this test was characterised by the normal symmetric progressive buckling. 325w325 and 325p325B were crushed by 180mm and 182 mm respectively, just less than the crush distance of specimen 650sB of 185mm.

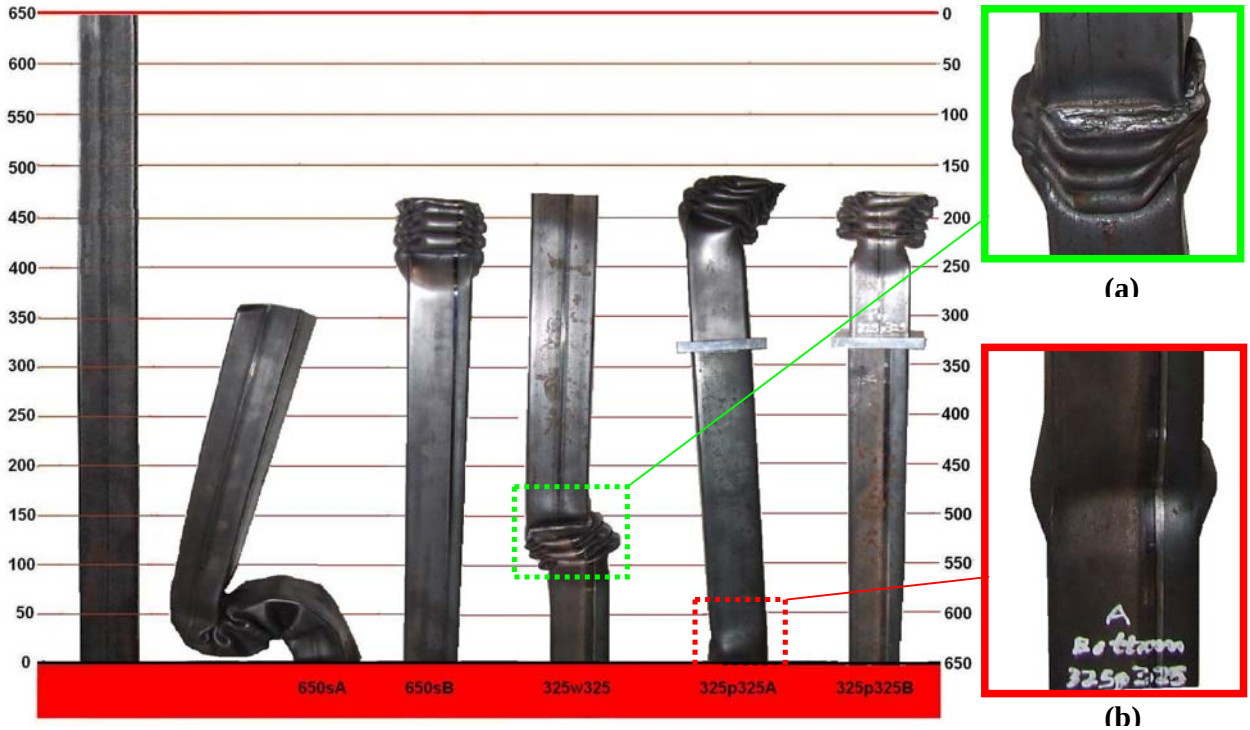

Figure 4.23: Buckling profiles of 650mm specimens with close ups of (a) 325w325 and (b) 325p325A.

As was seen in the 550mm single tube specimen in Figure 4.21, the 700mm single tube specimen buckled progressively with lobe formation initiating at the bottom of the tube as shown in Figure 4.24. It crushed by 185mm, the same amount as 650sB in the previous set. The welded tube specimen 350w350 underwent transition buckling. Lobe formation occurred around the welded region before global bending occurred at the base of the specimen which caused the specimen to bend severely and the mass crushed the top end of it laterally thus flattening it as shown in the close up in Figure 4.24. The plate-divided specimen 350p350 buckled progressively but lobes formed in the bottom tube of the specimen right below the plate and were slightly skew. Further crushing, it seems, may have caused transition buckling.

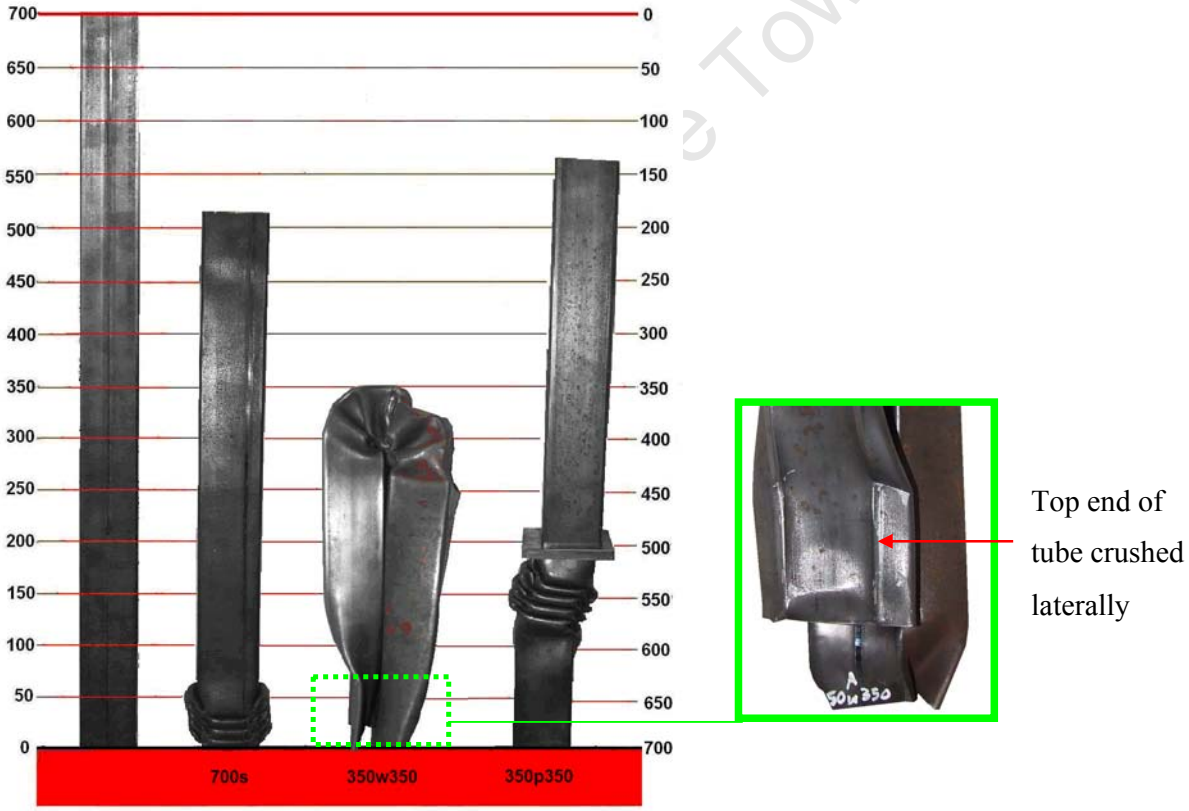

Figure 4.24: Buckling profiles of 700mm specimens with close up of specimen 350w350.

Tests on 800mm specimens revealed that once more the single tube specimen, in this case 800sA, buckled progressively with lobe formation starting at the bottom end of the tube right above the clamp (see Figure 4.25). The retest 800sB exhibited similar behaviour with most lobes forming at the lower end but one layer of lobes forming at the top end as shown in the close up in Figure 4.25a. It is unclear where the lobes started forming. In the welded tube specimen 400w400, lobe formation occurred in the upper half just above the weld and also a half-lobe formed near the top of the specimen as shown in the close up in Figure 4.25b.

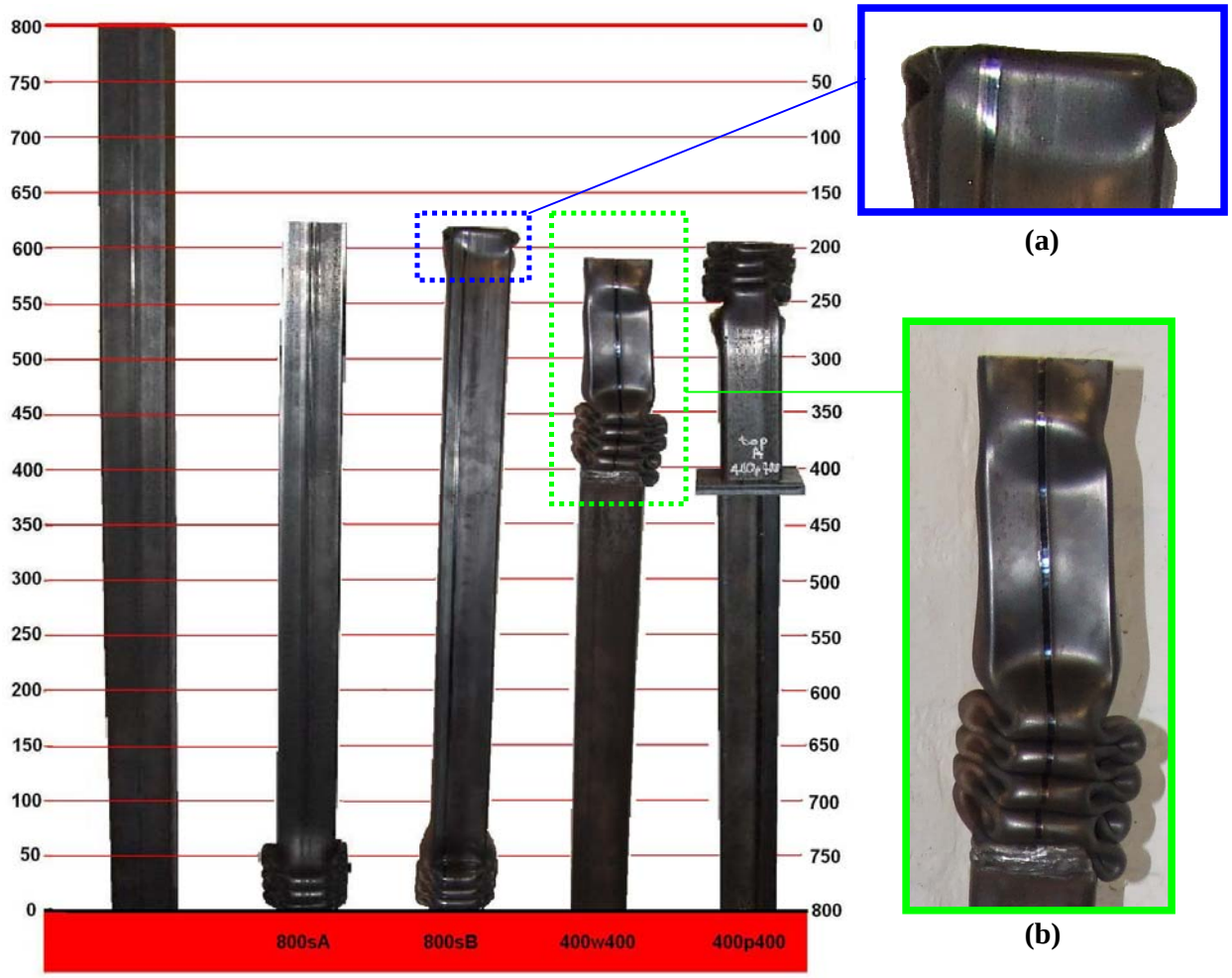

Figure 4.25: Buckling profiles of 800mm specimens with close ups of (a) 800sB and (b) 400w400.

In the 900mm tests, the single tube specimen 900s buckled progressively with lobes forming at the bottom end of the tube as shown in Figure 4.26. This follows the trend seen in the 700mm and 800mm single tube. Warping occurred at the upper end of the tube suggesting that lobe formation may have continued at the upper end if the tube was crushed more. A close up of this warping is shown in Figure 4.26. 900s deformed by 202mm while its welded equivalent 450w450 crushed by 216mm. A plate-divided specimen was not available for this set.

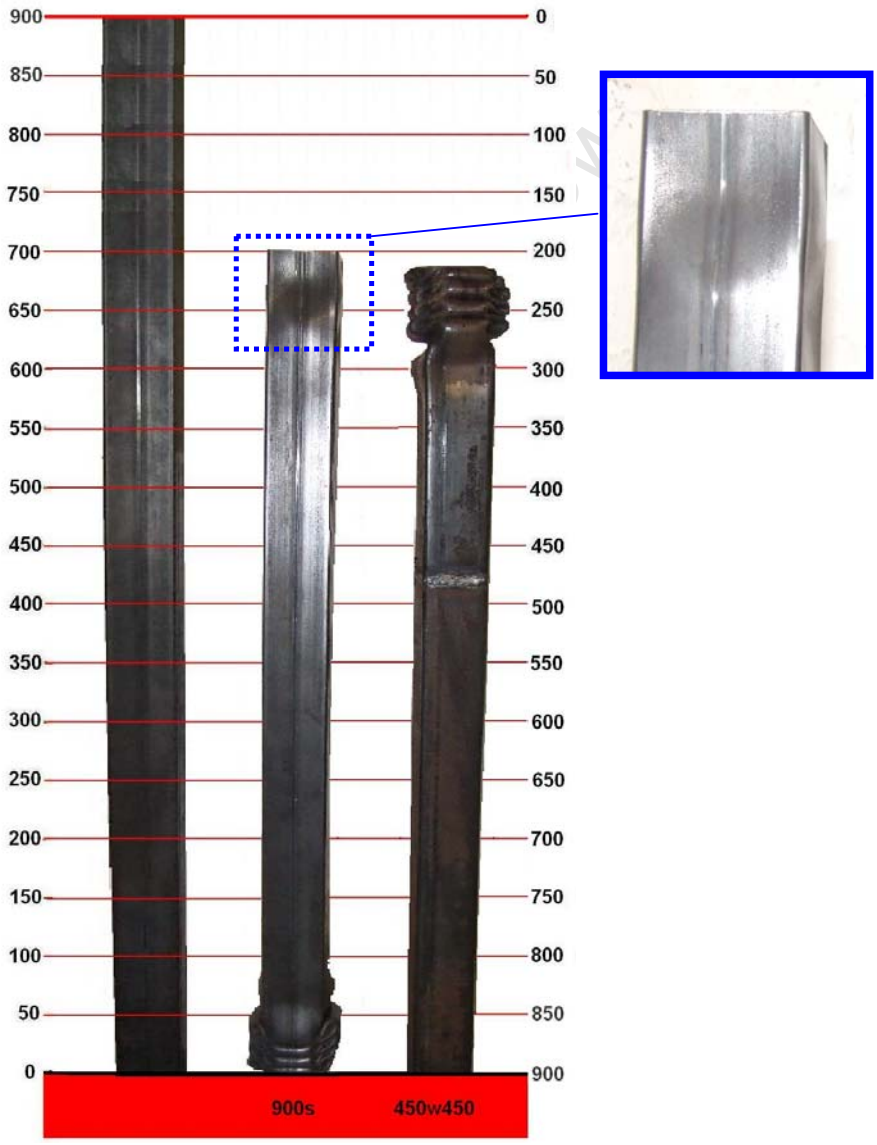

Figure 4.26: Buckling profiles of 900mm specimens with Close up of 900s showing warping.

In 1000mm tests the single, welded and plate-divided specimens all deformed progressively with lobe formation initiating at the top of each specimen as shown in Figure 4.27. In 500w500, the lobes, although symmetric in nature, formed skew and the warping at the bottom of the tube suggests that this specimen may have experienced transition buckling if further crushing had taken place. The plate-divided specimen 500p500 crushed by 201mm, about 25mm more than the single and welded equivalents.

Figure 4.27: Buckling profiles of 1000mm specimens with close up of 500w500 showing skew lobe formation.

1100mm test results revealed that the single tube in this case, 1100s, buckled in the transition region while the welded and plate-divided specimens (550w550 and 550p550, respectively) buckled in a symmetric progressive manner, as shown in Figure 4.28. Figure 4.28 also shows the close up of the top end of 1100s showing the combination of progressive buckling and global bending that characterises transition buckling. 550w550 and 550p550 were crushed by 215mm and 218 mm, respectively.

Figure 4.28: Buckling profiles of 1100mm specimens up of 1100s showing skew lobe formation characterising transition buckling.

Tests performed on 1200mm specimens (see Figure 4.29) revealed inconsistent behaviour in the deformation of single tubes. 1200sA crushed progressively but with a irregular folding mechanism near the end of the crush zone as shown by the close up in Figure 4.29a. In 1200sB lobe formation occurred at the top of the specimen and at the bottom right above the clamp. Figure 4.29b shows the close up of the lobes formed at the lower end of the specimen. It is uncertain which set of lobes formed first. The welded tube specimen 600w600 underwent transition buckling. Figure 4.26c shows a close up of the buckling zone. The plate-divided specimen crushed in a symmetric progressive manner.

Figure 4.29: Buckling profiles of 1200mm specimens with close ups of (a) 1200sA and (b) 1200sB and (c) 600w600.

Of all the length sets tested, the 1300mm specimens could be describes as the most consistent since all three specimen types (single, welded and plate-divided) buckled in a symmetric progressive manner and lobe formation initiated at the top of each specimen, as shown in Figure 4.30. Furthermore, the crush distances were all over 200mm and differed by very small amounts. 1300s was crushed by 207mm, 650w650 by 206mm and 650p650 by 212mm.

Figure 4.30: Buckling profiles of 1300mm specimens.

The 1400mm specimens were also relatively consistent with each other, exhibiting similar behaviour to 1300mm specimens when crushed. Again the lobes formed at the upper end of the specimens (see Figure 4.31) in a symmetric progressive manner but in all three cases the lobes were notably skew as shown in the close ups in Figures 4.31a, b and c. The reason for this is not clear but it may be that the drop mass shifted slightly after previous tests and caused it to impact these specimens at a very slight angle.

Figure 4.31: Buckling profiles of 1400mm specimens with Close ups of (a) 1400s, (b) 700w700 and

(c) 700p700 showing skew lobe formation.

According to theoretical predictions [12] it would have been expected that at 1500mm square tubes of this cross-section would buckle in the global bending mode as the theoretical boundary at which these type of tubes step out of the transition zone and into the global bending zone occurs at 1494mm. However, as is almost always the case, the 'real world' doesn't conform to theory. None of the 1500mm specimens experienced global bending. The deformed profiles for the 1500mm specimens are shown in Figure 4.32. 1500s, 750w750B (retest) and 750p750B (retest) buckled in a symmetric progressive manner. 750w750A buckled in the transition mode (see Figure 4.32a) after undergoing initial progressive buckling. Specimen 750p750B provided an interesting result in that the top tube buckled progressively in a symmetric manner but then slipped out along with the plate causing the drop cage to continue falling and slightly crushing the top end of the bottom tube as shown in Figure 4.32b. The crush distance of the bottom tube was not considered.

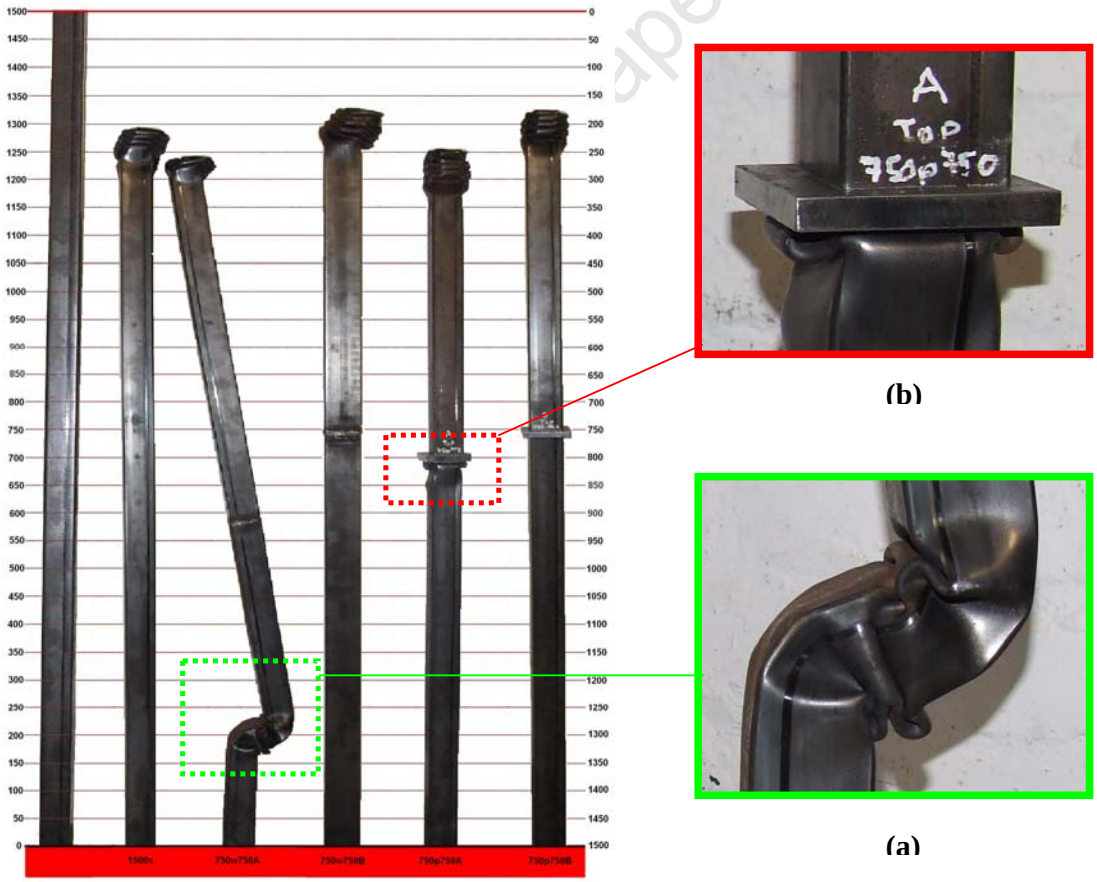

Figure 4.32: Buckling profiles of 1500mm specimens with close ups of (a) transition zone of 750w750A and (b) secondary crushing of bottom tube in 750p750A after fly-out of top tube.

In 1600mm specimens (see Figure 4.33), the single tube specimen, 1600s, buckled in a progressive symmetric mode while the welded specimen, 800w800, underwent global bending (as was expected for this length) before the weld failed (see Figure 4.33a) and caused shearing and severe damage to the tube as the drop cage came to rest just a couple of centimetres above the clamp. In the case of the plate-divided specimen, 800p800, once again the top tube of the specimen deformed in a symmetric progressive manner before slipping out along with the plate causing the drop cage to impact the bottom tube and caused some deformation to it as shown in Figure 4.33b. Similarly to 750p750A, the crush distance of the bottom tube was not taken into account in calculations.

Figure 4.33: Buckling profiles of 1600mm specimens with close ups of (a) failure at weld of 800w800 and (b) secondary crushing of bottom tube in 800p800 after fly-out of top tube.

In 1700mm specimens, global bending was certainly expected to occur but once again symmetric progressive buckling prevailed as shown in Figure 4.34. In the single tube specimen, 1700s, although progressive buckling occurred (crush distance of 190mm), the tube was on the verge of transition buckling and would have started to bend globally if it had been crushed more (see close up in Figure 4.34). In this set the welded tube was crushed by the most (215mm).

Figure 4.34: Buckling profiles of 1700mm specimens with close up showing initiation of global bending that would have led to transition buckling in 1700s.

5. ANALYSIS OF EXPERIMENTAL RESULTS

This chapter provides more detailed analysis of experimental results that were presented in Chapter 4. In particular, the results are compared to those obtained by Abramowicz and Jones [12].

5.1 Quasi-Static Axial Crushing

It was originally predicted that the specimens would buckle in the asymmetric mixed mode B-type since the ratio of C/H for all specimens was 31.25. Jones [2] showed that theoretically asymmetric mixed mode B-type progressive buckling occurs within the range $7.5 \leq C/H \leq 40.8$. However, this was not the case as all specimens that buckled progressively exhibited the symmetric mode, except in the case of specimen 200p200 in which the top tube buckled in progressive asymmetric mixed mode A shown in Figure 5.1.

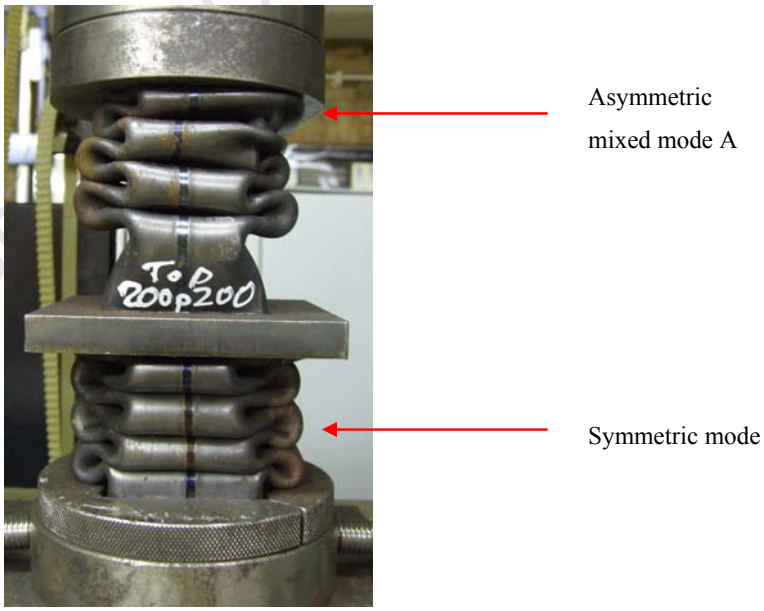

Figure 5.1: Progressive buckling of specimen 200p200 showing asymmetric mixed mode A in top tube and symmetric mode in bottom tube.

5.1.1 Weld Behaviour and Formation of Lobes

Although each welded specimen comprised of two tubes, the specimens as a whole behaved as a single tube. The weld permitted continuity between the two tubes allowing lobe formation to continue unaltered at the weld and past the weld as shown in Figure 5.2. Figure 5.3 shows that a slight change in load was experienced by the specimen as the weld formed part of a lobe layer. This would be expected since at the weld the specimen wall was essentially thicker, making a specimen stronger at this point and slightly more force would have been required to deform it.

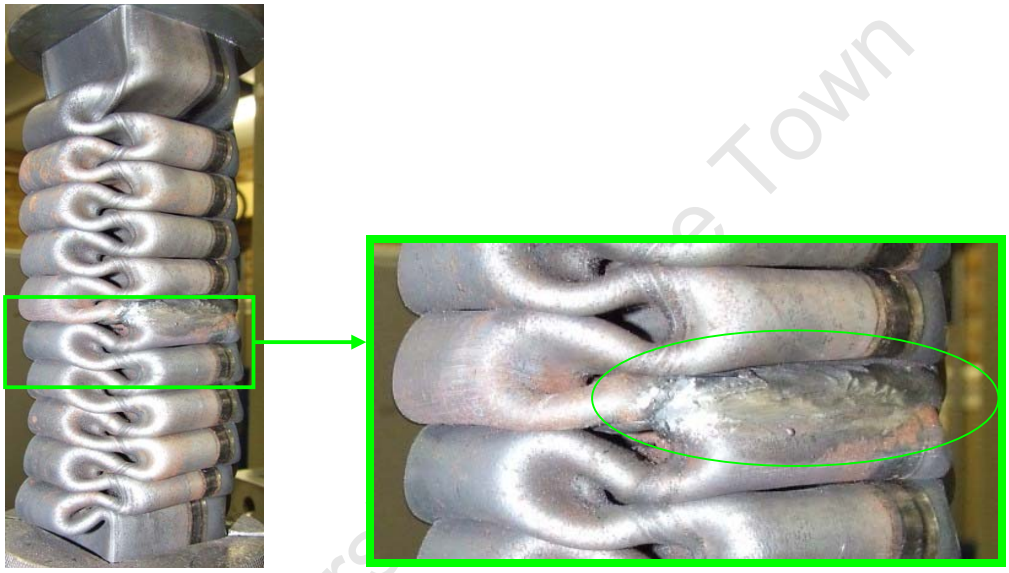

Figure 5.2: Specimen 300w300 showing how the weld becomes incorporated as a lobe.

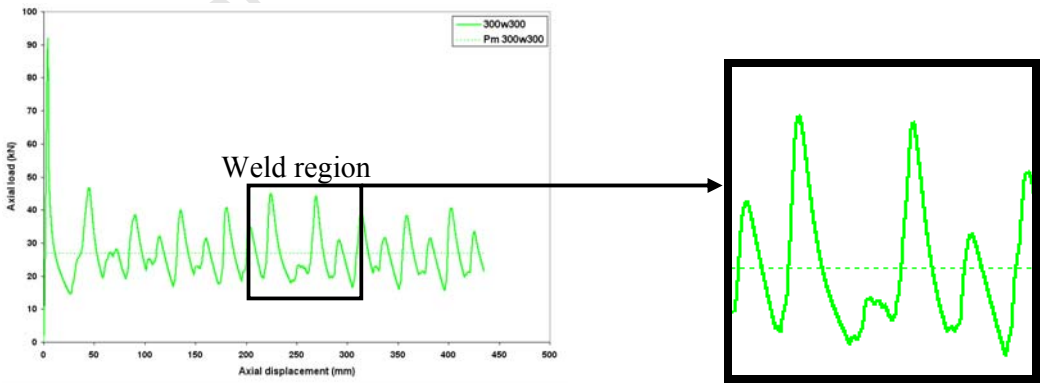

Figure 5.3: Axial load-displacement graph of specimen 300w300 showing a slight change in load as lobe formation incorporates weld.

5.1.2 Plate-Divided Specimens' Behaviour and Formation of Lobes

Plate-divided specimens differed from single and welded tube specimens in that they are characterised by two ultimate peak loads (see points A and B in Figure 5.4) as each tube in the specimen crushed independently of the other but not at the same time. As one tube was crushed to a maximum, the second tube would start to buckle. Two ultimate peak loads are undesirable in structural crashworthiness applications since it represents two very large decelerations which in turn pose a great risk to passenger or cargo safety in a vehicle. An interesting feature of axial load-displacement curves in plate-divided specimens was the greater axial displacement required to initiate the second peak load than the first peak load. Figure 5.4 shows the axial load-displacement curve of 250p250. X_1 is the axial displacement of the bottom tube required to reach the first peak load of 86kN while X_2 is the axial displacement required to reach the second peak load of 80kN which occurred in the top tube. X_2 is 12.5mm, almost three times larger that the value of X_1 of 4.6mm. The reason for this behaviour is that as the top tube began to crush, the bottom tube was still crushed by a small amount. Once lobe formation initiated in the top tube, the bottom tube ceased to displace any further.

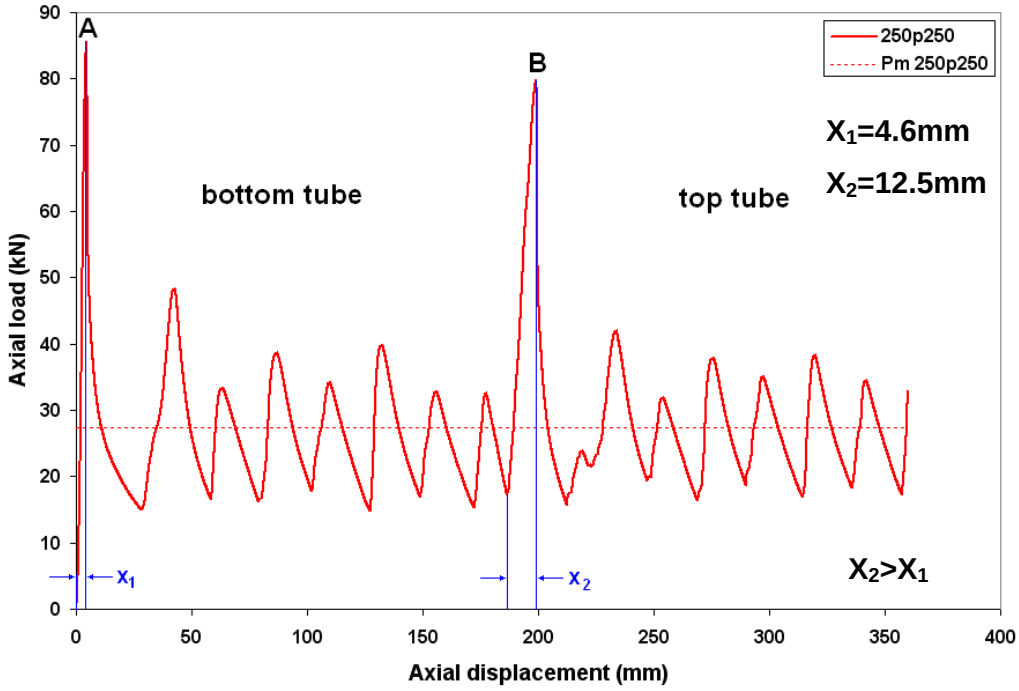

Figure 5.4: Axial load-displacement graph of specimen 250p250 showing the axial displacement required to reach each peak.

Another point of interest with regard to plate-divided specimens was the initiation of lobe formation. There was no consistency in initial lobe location. Figure 5.5 shows three of the plate-divided specimens. In 250p250, buckling first occurred at the bottom of the bottom tube and the top tube buckled at the top as shown in Figure 5.5a. In 300p300, buckling initiated in the top tube at the top and the bottom tube also buckled from the top as shown in Figure 5.5b. In 350p350 buckling started in the top tube at the bottom right above the plate and the bottom tube buckled from the top right below the plate.

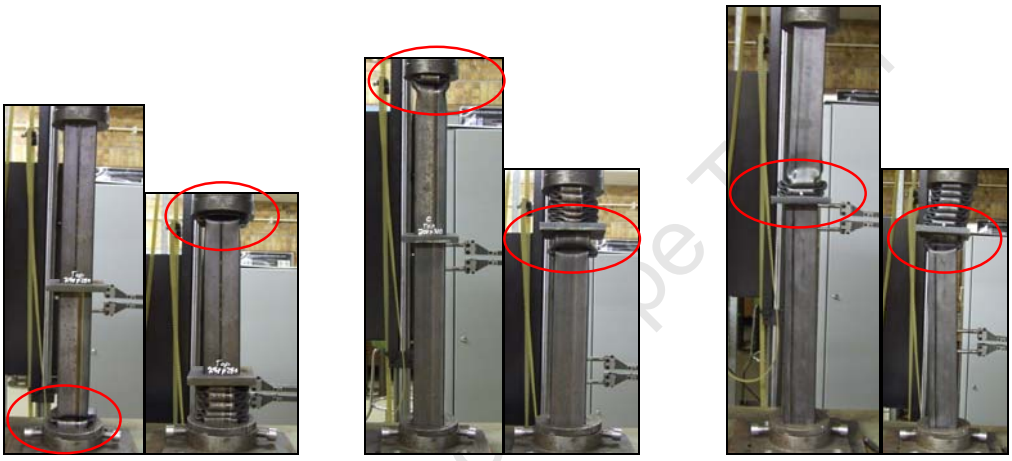

(a) **(b)** **(c)**

Figure 5.5: Initiation of lobes in (a) 250p250, (b) 300p300 and (c) 350p350 showing inconsistency in lobe initiation location.

The initiation location of lobes in plate-divided specimens appears to be random and it seems difficult to predict where buckling would occur. It would appear that each tube making up a specimen had a 'weaker' end and presumably buckling occurred in these regions.

5.1.3 Region from Progressive to Global Bending

Quasi-static test revealed a *changeover* region in which specimens would buckle in the global bending mode as opposed to the progressive mode. The word *changeover* is used and this should not be confused with *transition. Transition* implies a combination of progressive and global bending while *changeover* refers to a definitive region where either progressive buckling or global bending would occur, but not a combination of the two. Transition buckling was not observed in quasi-static tests. Abramowicz and Jones [12] also noted this behaviour in quasi-static experiments performed on mild steel square tubes. Abramowicz and Jones derived theoretical and empirical formulae for the critical length-to-width aspect ratio under quasi-static loading and are given by Eq. (5.1) and (5.2), respectively:

$$\left(\frac{L}{C}\right)_{cr} = 2\frac{\left(\frac{C}{H}\right)^{1/3}}{1-2.88\left(\frac{H}{C}\right)^{4/3}} \qquad \textit{Theoretical} \text{ [12]} \qquad (5.1)$$

and

$$\left(\frac{L}{C}\right)_{cr} = 2.482e^{\left(0.0409\frac{C}{H}\right)} \qquad \textit{Empirical} \text{ [12]} \qquad (5.2)$$

where L and C are the length and width of the tube respectively, and t is the wall thickness of the tube. Eq. 5.2 was obtained by means of a best fit curve of their experimental data. For tubes with width of C = 50mm and thickness t = 1.6mm, the critical length-to-width aspect ratios are as follows:

$$\left(\frac{L}{C}\right)_{cr} = 6.49 \qquad \textit{Theoretical} \text{ [12]} \qquad (5.3)$$

and

$$\left(\frac{L}{C}\right)_{cr} = 8.91 \qquad \textit{Empirical} \text{ [12]} \qquad (5.4)$$

Table 5.1 presents length-to-width ratios and buckling modes of quasi-static specimens.

Table 5.1 Length-to-width aspect ratios of quasi-static specimens

Specimen	*L (mm)*	*C (mm)*	*H (mm)*	$\left(\frac{L}{C}\right)$	$\left(\frac{L_{bottom}}{C}\right)$	$\left(\frac{L_{top}}{C}\right)$	$\left(\frac{C}{H}\right)$	*Buckling mode and number of lobes*
400s	400	50	1.6	8	-	-	31.25	S (12)
200w200	400	50	1.6	8	-	-	31.25	S (14)
200p200	400	50	1.6	8	4	4	31.25	[S (7)] [A (2)-S (5)]
500s	500	50	1.6	10	-	-	31.25	S (16)
250w250	500	50	1.6	10	-	-	31.25	S (17)
250p250	500	50	1.6	10	5	5	31.25	[S (8)] [S (8)]
600s	600	50	1.6	12	-	-	31.25	S (19)
300w300	600	50	1.6	12	-	-	31.25	S (19)
300p300	600	50	1.6	12	6	6	31.25	[S (9)] [S (10)]
700s	700	50	1.6	14	-	-	31.25	S (23)
350w350	700	50	1.6	14	-	-	31.25	S (23)
350p350	700	50	1.6	14	7	7	31.25	[S (10)] [S (12)]
750s	750	50	1.6	15	-	-	31.25	S (24)
375w375	750	50	1.6	15	-	-	31.25	G
375p375	750	50	1.6	15	7.5	7.5	31.25	G
800s	800	50	1.6	16	-	-	31.25	G
400w400	800	50	1.6	16	-	-	31.25	G
400p400	800	50	1.6	16	8	8	31.25	G

Notation used in Table:

A	**Asymmetric**	**( )**	**Number of complete lobes**
G	**Global bending**	**[ ] [ ]**	**Bottom and top lobe description, respectively**
S	**Symmetric progressive**		
s	**single tube specimen**		
w	**welded tubes specimen**		
p	**plate-divided specimen**		

For single tube specimens, global bending only occurred in the 800mm tube while for welded and plate-divided specimens global bending occurred for 750mm specimens. Specimen 750s buckled in a progressive manner. Figure 5.6 shows how results of quasi-static tests compared to the theoretical and empirical curves obtained by Abramowicz and Jones [12]. Their data points are not included for the sake of clarity.

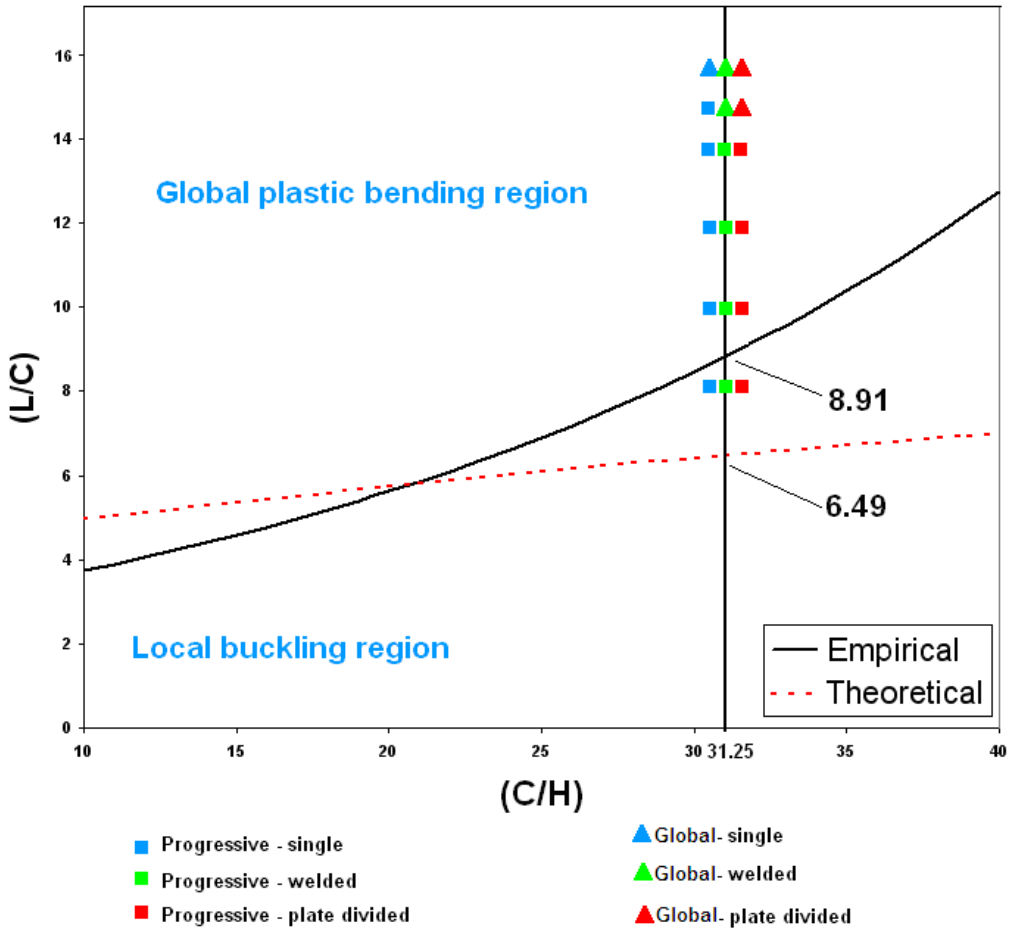

Figure 5.6: Length-to-width ratio versus width-to-thickness ratio graph showing quasi-static data (C/H = 31.25) compared to lines separating global plastic bending and local buckling (progressive buckling) obtained by Abramowicz and Jones [12].

From their theoretical equation (see eq. 5.1), Abramowicz and Jones [12] predicted that global bending would occur at a critical length-to-width aspect ratio of 6.49. Their experimental data yielded an increase of this ratio to 8.91. From the quasi-static results it appears that for single tubes the critical ratio lies between 15 and 16 while for welded and plate-divided specimens the critical ratio is between 14 and 15. More tests with different width-to-thickness ratios (C/H) would need to be performed to confirm this trend and in turn equations similar to those derived by Abramowicz and Jones [12] could be obtained. One should also bear in mind that the yield stresses of the mild steel tubes tested by Abramowicz and Jones [12] ranged from 249MPa to 464MPa depending on the cross sectional dimensions. They performed quasi-static

tensile tests in the same way as they were performed for this thesis, by cutting tensile test specimens from the sides of the tubes, and they were tested at strains in the same order of magnitude. Table 5.2 compares material data obtained by Abramowicz and Jones [12] and data obtained from tensile tests performed for this thesis.

Table 5.2 Comparison of material data to that obtained by Abramowicz and Jones [12]

Specimen type	*C (mm)*	*H (mm)*	*(C/H)*	σ_y *(MPa)*
SA*	8.5	**1.55**	5.46	**385**
SB*	14.8	1.22	12.10	361
SC*	28.7	1.30	22.10	326
SD*	30.84	1.19	25.92	263
SE*	37.3	1.17	**31.84**	**249**
SF*	54.0	1.42	37.99	464
50×50×1.6**	**50.0**	**1.60**	**31.25**	**328**

* Material data obtained from tensile tests by Abramowicz and Jones [12].

** Material data obtained from tensile tests for this thesis.

Table 5.2 shows that specimen type SA closely matches the 50×50×1.6 tube in terms of thickness (in blue for SA) but the difference in static yield stress (in blue for SA) is quite considerable with a difference of 57MPa in favour of specimen type SA. The *C/H* ratio for specimen type SE (in green) closely matches the ratio for the 50×50×1.6 tube but in this case SE has a static yield stress of 249MPa compared to 328MPa for the 50×50×1.6 tube. This makes sense since the SE type specimen has a smaller thickness. The lower yield stress may have made the tube more unstable under the same loading conditions than a tube with higher yield strength. This difference in yield stresses between geometrically similar tubes could be a significant factor which explains the difference between the experimental results compared to those of Abramowicz and Jones [12].

5.2 Dynamic Axial Crushing

As with quasi-static specimens, it was originally predicted that the specimens would buckle in the asymmetric mixed mode B-type since the ratio of C/H for all specimens was 31.25. However, asymmetric mixed mode was the exception and not the rule as most specimens that buckled in the progressive buckling region, buckled in a symmetric manner. There were a number of cases were specimens would crush slightly irregularly or askew but the lobe layers still exhibited symmetric mode. Transition and global bending were also observed in some specimens and will be discussed further. Figure 5.7 is a chart showing crushed distance and buckling modes of specimens tested with a drop height of 3.26m (V = 8m/s). Most tests were performed with this drop height for ease of comparison.

5.2.1 Single Tube Specimens and Formation of Lobes

Of the three specimen configurations, single tubes exhibited the most predictable behaviour. Extensive studies have been performed on single tubes and most theory and equations that exist for square tube buckling relate to single tubes. For this reason single tubes provided a good basis for comparison for the other two configurations, namely welded and plate-divided specimens. Single tubes buckled in a progressive manner for almost all lengths tested, including up to the longest tube of 1700mm. However, three single tubes buckled in the transition mode as shown in Figure 5.8. In all three cases it seems that the tubes started to buckle in a progressive manner and then continued to buckle in an global bending manner. Two of these specimens were relatively short tubes with lengths of 600mm and 650mm. Retests of both these tubes resulted in progressive buckling. The 1100mm tube also buckled in a transition mode but tubes on either side of it in terms of length (1000mm and 1200mm) buckled in a progressive mode. These ‘anomalies’ suggest that the tubes may have been lined up slightly skew in the clamp and struck at a slight angle by the impact mass triggering global bending after some initial lobe formation. Specimen 1700s buckled in a progressive manner but global bending had just started to occur near the bottom of the tube. Any further crushing of the tube would probably have resulted in transition buckling being observed.

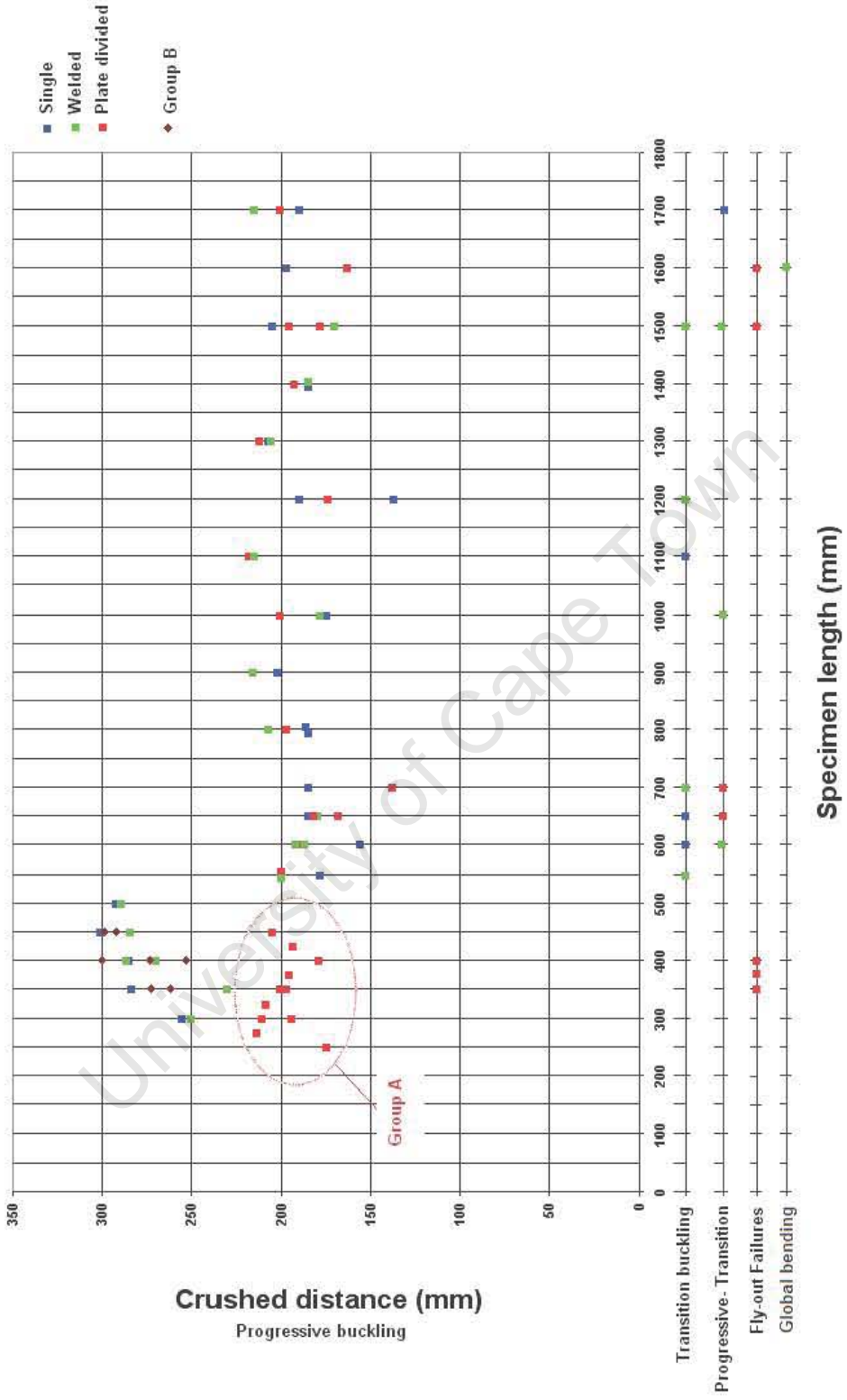

Figure 5.7: Crushed distances and buckling mode chart of dynamic tests performed with h = 3.26m (V = 8m/s).

(a) **(b)** **(c)** **(d)**

Figure 5.8: Single tube specimens (a) 600sA, (b) 650sA and (c) 1100s that buckled in the transition mode characterised by initial progressive buckling and subsequent global bending. (d) 1700s on the verge of transition buckling.

An interesting observation from single tube test results is the formation of lobes. Figure 5.9 shows lobe formation position of single tube specimens. While in most cases lobe formation occurred at the top of each tube, there were a few specimens that started buckling from the bottom right above the clamp. Most noteworthy of this occurrence are specimens 700s, 800sB and 900s since their lengths follow on from each other. This behaviour might be coincidental but it may also have to do with stress wave propagation through the length of tube.

Figure 5.9: Position of lobe formation in single tube specimens with original lengths ranging from 550mm to 1500mm (not scaled). Blue arrows indicate lobe formation from the top while orange arrows indicate lobe formation from the bottom above the clamp.

5.2.2 Welded Specimens and Formation of Lobes

Of the three specimen configurations, welded tube specimens behaved the most erratically with varied results. It was pointed out that in quasi-static tests welded tube specimens behaved very similarly to single tubes in that only one peak force arose instead of two as seen in plate-divided specimens. This tendency was confirmed in dynamic tests as welded tube specimens had very similar crush distances and identical buckling modes to single tubes. This was especially true in the case of shorter tubes. However in longer tubes, some welded tubes buckled in a transition mode (see Figure 5.10) while the single tube equivalents buckled progressively. Specimens 300w300A, 500w500 and 750w750B buckled in a progressive manner but were on the verge of transition buckling. Any further crushing would probably have caused these specimens to bend globally after their initial progressive lobe formation. Only one welded tube specimen (800w800) buckled in the global bending mode as shown in Figure 5.10. This instability caused by the global buckling in this tube caused the weld to break on three sides (one side remained attached). In some cases, where

progressive buckling did occur, lobe formation initiated in the weld region. This occurred in 325w325 and 400w400 as shown in Figure 5.11.

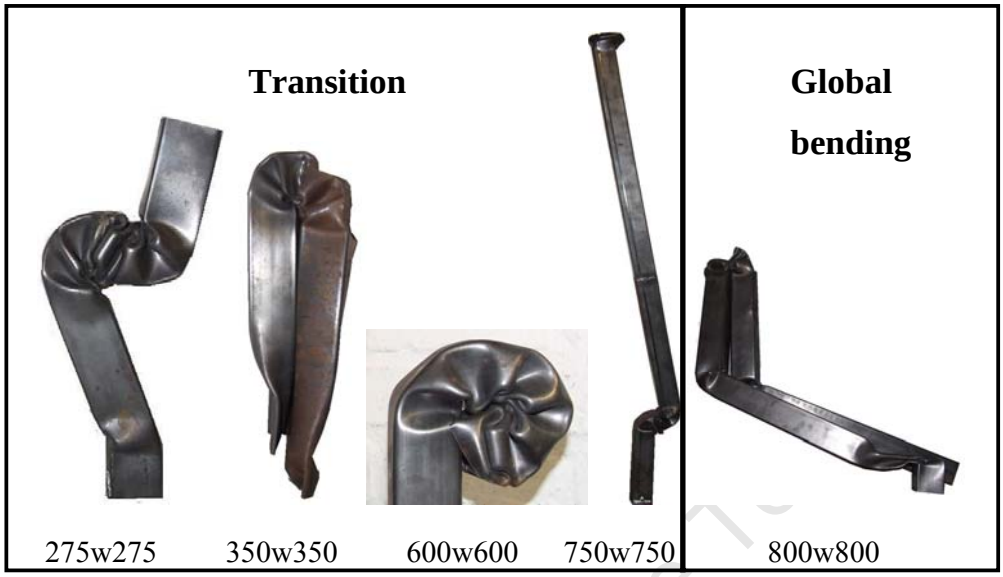

Figure 5.10: Welded tube specimens that buckled in the transition mode and global bending mode.

Figure 5.11: Lobe formation in (a) the bottom tube of 325w325 just below the weld and (b) the top tube in 400w400 just above the weld.

5.2.3 Plate-divided Specimens and Formation of Lobes

Plate-divided specimens did not exhibit any transition or global bending. In most cases, specimens buckled progressively in a symmetric manner. Transition and global bending are undesirable collapse modes in tubular structures and are not favourable to plastic deformation energy absorption. At some specimen lengths, while single or welded tubes buckled in a transition or global bending manner, plate-divided specimens would buckle progressively. In other cases where all three specimen configurations buckled in the progressive mode, the plate-divided specimen would crush more than the single and welded tube configurations. This behaviour was noticed in longer tube specimens but in shorter tube specimens, the plate-divided specimens would crush less than the welded and single tubes. In some plate-divided specimens, *fly-out failures* occurred. *Fly-out failure* was a term coined in tests performed on specimens in **Group A** where it was often observed that as a plate-divided specimen was struck by the drop mass, the top tube and plate would slip out leaving the clamped bottom tube alone to be crushed by the mass as shown in Figure 5.12. It should be noted that the plate and top tube were only balanced loosely and not tied to each other in any way. Fly-out failures were common in short specimens up to 400mm in length but were observed in 1500mm and 1600mm specimens too. At lower impact velocities, fly-out failures were more prevalent.

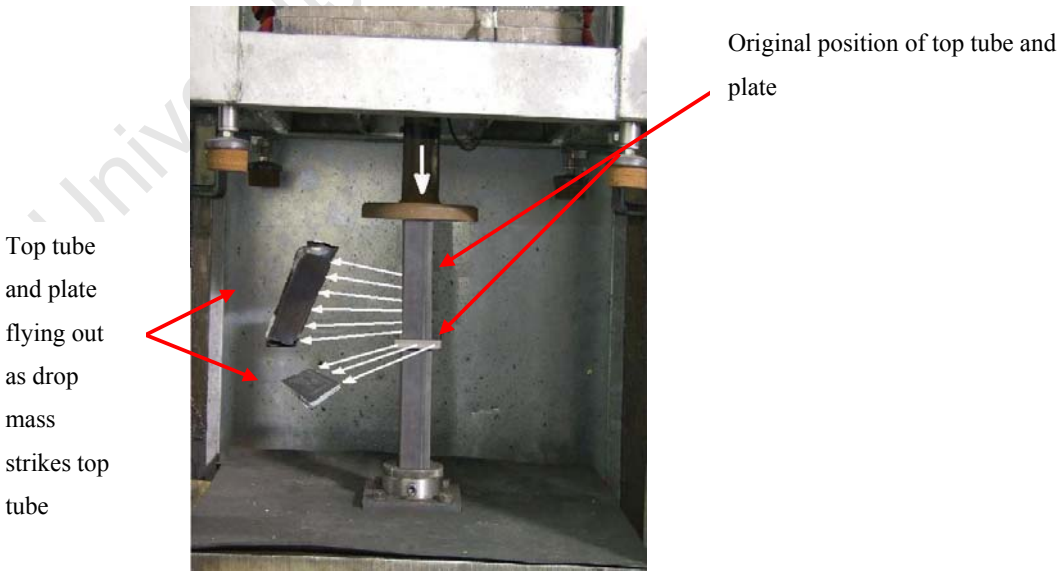

Figure 5.12: Visual representation of fly-out failure of a plate-divided specimen.

As observed in single and welded tube specimens, two plate-divided specimens (325p325A and 350p350) buckled in the progressive buckling mode but were on the verge of global bending as shown in Figure 5.13. Any further crushing of these specimens would probably have caused transition buckling.

Figure 5.13: Initiation of global bending after initial progressive buckling which would have led to transition buckling in specimens (a) 325p325A and (b) 350p350.

Initiation of lobe formation was relatively constant in plate-divided specimens as most specimens started buckling at the top of the top tube as shown in Figure 5.14a. In specimen 275p275 lobe formation initiated at the bottom end of the top tube as shown in Figure 5.14b, while in 350p350, lobe formation started in the bottom tube as shown in Figure 5.14c.

Figure 5.14: (a) Typically lobe formation would start from the top of the top tube but in (b) 275p275 lobe formation initiated at the bottom of the top tube while in (c) 350p350 lobe formation started in the bottom tube.

5.2.4 Progressive Buckling at Different Drop Heights

Short single and welded tube specimens from **Group C** (presented in Table 4.4) that buckled in the progressive buckling mode are compared to plate-divided specimens from **Group A** (see Table 4.2). Crushed distances of these specimens are shown in the chart in Figure 5.15. Although the cross sectional areas of all the specimens were the same, the single and welded specimens were cut from a different set of tubes than the tubes used for the plate divided specimens in 2006 so it is quite likely that the tubes had different material properties such as yield stress. The chart shows that for a certain drop height, single tube specimens were the most efficient as they crushed by the larger amount with the welded specimen always crushing slightly less. The plate-divided specimens (tested almost a year before the single and welded tubes) crushed significantly less for the same drop height. The single and welded specimens were measured again and it was found that the wall thickness varied from 1.5mm to 1.6mm in most specimens. Even though this difference in thickness was very small, it could have had a significant effect on the crush distance. Wall thickness and crush distance are inversely proportional. This will be revisited in Chapter 7.

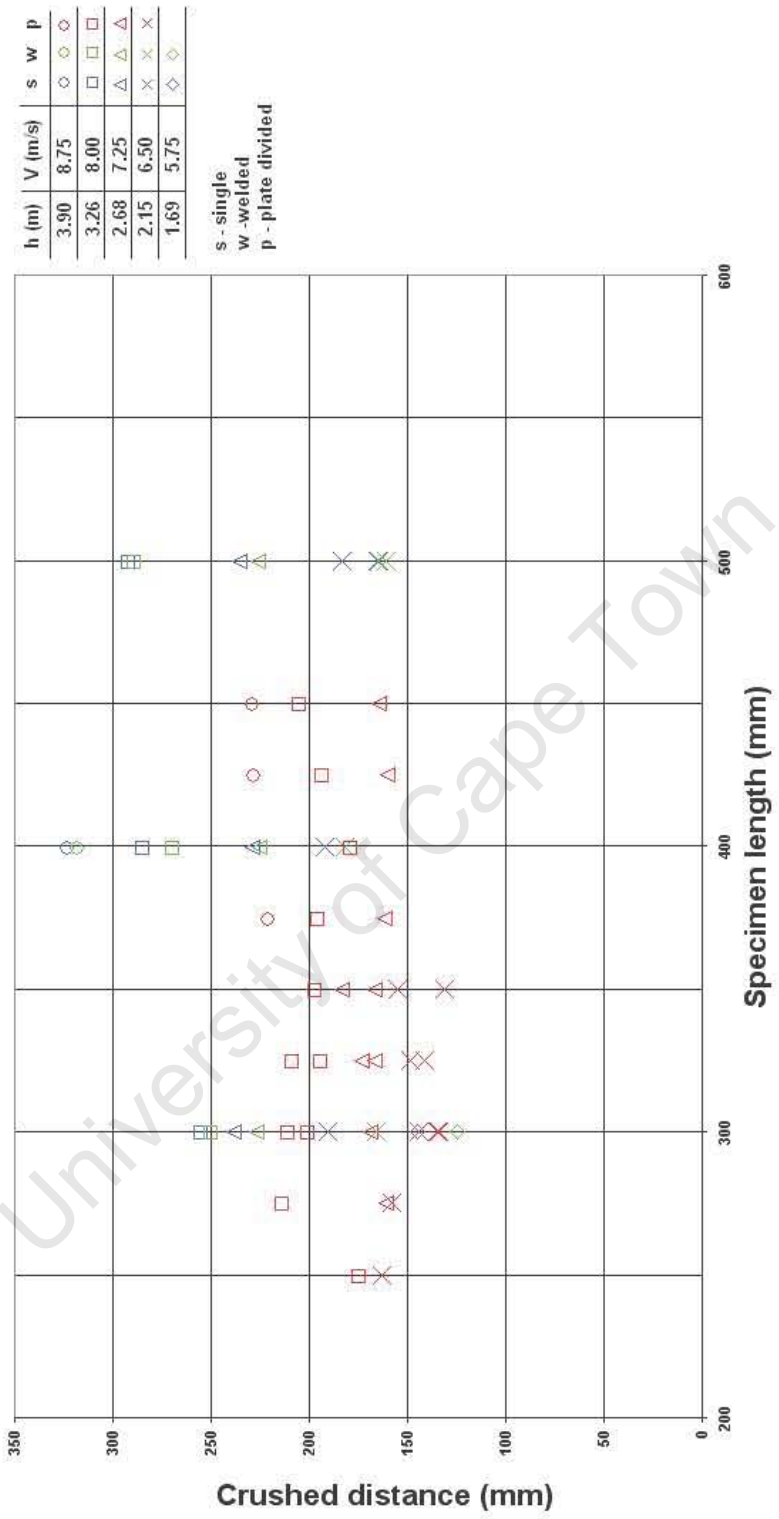

Figure 5.15: Crushed distance chart of shorter specimens that buckled in the progressive buckling region with drop heights of 3.90m, 3.26m, 2.68m, 2.15m and 1.69m. The red data points are specimens that were tested in Group A.

5.2.5 Transition Buckling

Although transition buckling was not observed in quasi-static tests, it was certainly seen in dynamic tests. This behaviour is consistent with the experimental observations of Abramowicz and Jones [12]. Eq. (2.19) and (2.20) refer to empirically derived formulae for the critical lengths under dynamic loading and are given by

$$\left(\frac{L}{C}\right)_{cr} = 2.453e^{\left(0.08\frac{C}{H}\right)} \tag{2.19}$$

and

$$\left(\frac{L}{C}\right)_{cr} = 3.423e^{\left(0.04\frac{C}{H}\right)} \tag{2.20}$$

Abramowicz and Jones [12] found that in general the transition from progressive to global bending for a given thickness, the critical length-to-width ratio given by the value $(L/C)_{cr}$ was larger under dynamic loading than for quasi-static loading. Results confirmed this tendency as only one specimen in the entire test matrix exhibited purely global bending (800w800). This welded specimen had a $(L/C)_{cr}$ of 32 while in quasi-static tests welded specimen displayed global bending at a ratio $(L/C)_{cr}$ of 15. Purely global bending did not occur in single and plate-divided specimens. Figure 5.16 is a length-to-width versus width-to thickness chart plotting all data points from **Group A, B** and **C** and these points are compared with Equations 2.19 and 2.20.

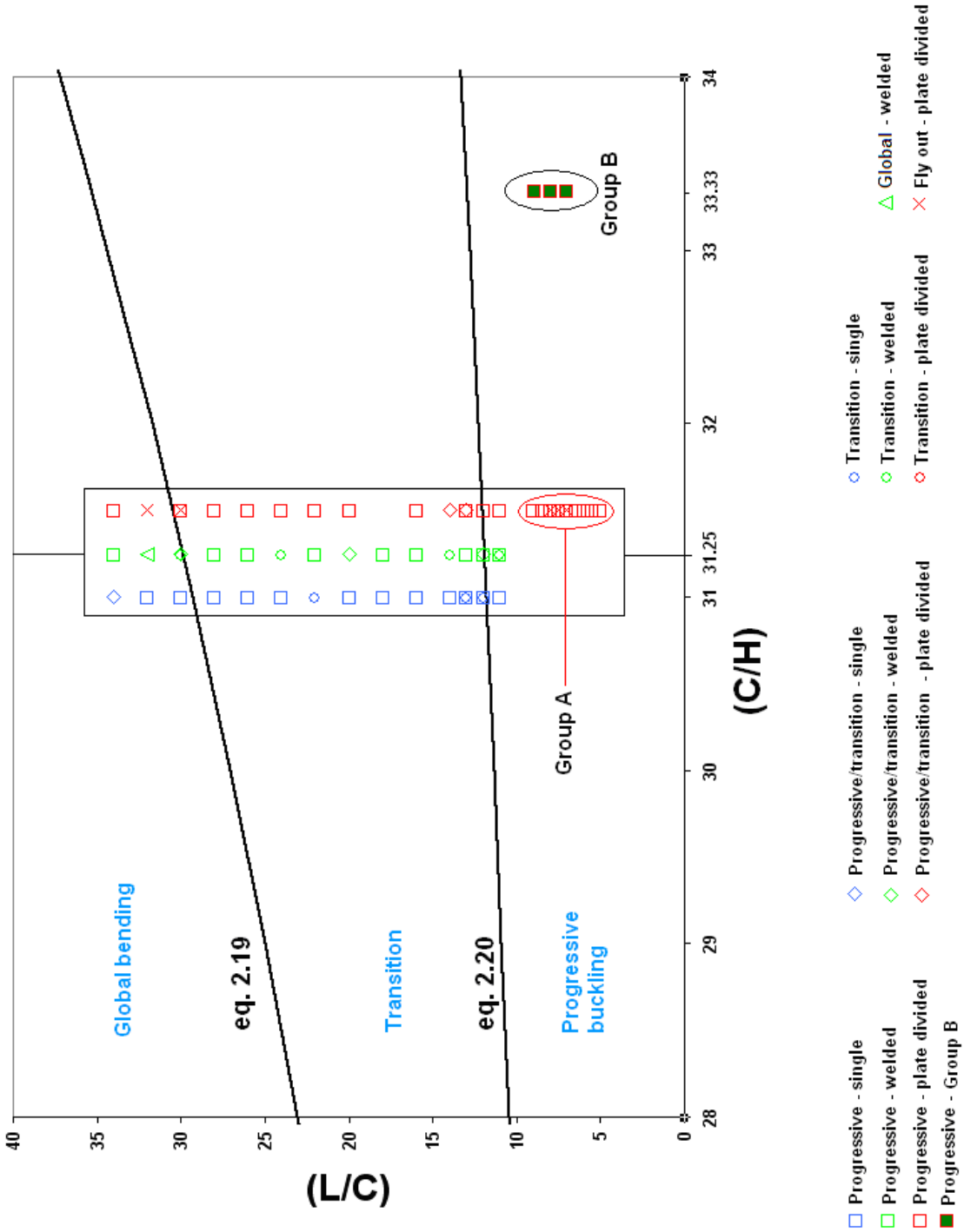

Figure 5.16: Length-to-width ratio versus width-to-thickness ratio graph showing dynamic test data (C/H = 31.25) compared to lines separating global plastic bending and local buckling (progressive buckling) obtained by Abramowicz and Jones [12].

6. FINITE ELEMENT MODELLING

This chapter outlines the finite element method for the numerical simulation of the different tube configurations.

6.1 Finite Element Analysis Method

The aim of this chapter is to produce 3-dimensional models of the dynamcic test specimens and to analyse the response of these models using a finite element program, namely ABAQUS. More specifically, ABAQUS/*Explicit* is used as it is the most efficient manner of analysing models with short dynamic response times such as in the case of dynamic axial tests. ABAQUS/*Explicit* takes into account non-linear geometry, strain rates, material and temperature effects when analysing. ABAQUS/*Explicit* solves governing equations by using an explicit integration scheme as opposed to direct integration scheme which is used in ABAQUS/*Standard*.

6.2 Element Types used in Finite Element Model

ABAQUS contains an element library to create complete geometric modeling irrespective of the size or shape of the objects being modeled. Any combination of models can be used to make up a model. User-defined elements can also be created and implemented. However, for modeling of square tubes, the elements available in the library are adequate. The tube models were created using the S4R element type as shown in Figure 6.1 is a quadrilateral 4-node doubly-curved thin or thick shell. It has reduced integration, hourglass control and finite membrane strains. The clamp and mass were modelled using the R3D4 element type which is a 4-node 3-D bilinear rigid quadrilateral as shown in Figure 6.2. The rigid plate was modelled using the C3D8R element type which is an 8-noded linear brick, 3-d continuum element as shown in Figure 6.3 that has reduced integration and hourglass control.

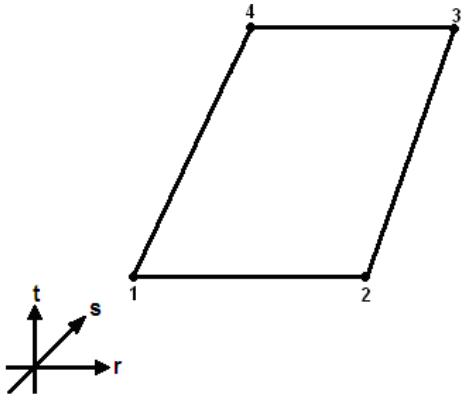

Figure 6.1: A schematic of S4R element showing node numbering and co-ordinate system.

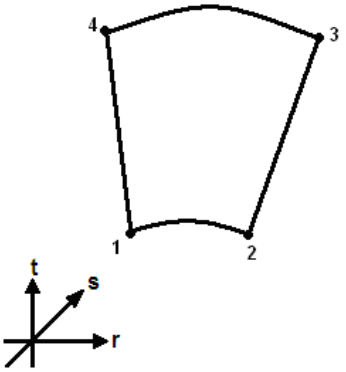

Figure 6.2: A schematic of R3D4 element showing node numbering and co-ordinate system.

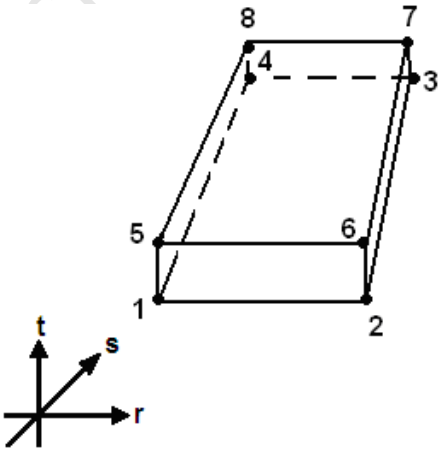

Figure 6.3: A schematic of C3D8R element showing node numbering and co-ordinate system.

6.3 Time Stepping and Integration Scheme

High speed footage was attained for welded tube specimens in **Group B**. Analyses of the footage revealed that for a drop height of 3.26m (V = 8m/s), it took a 50mm×50mm tube with a wall thickness of 1.6mm roughly 70ms to completely stop a drop mass of 340kg. Based on this observation, the simulations were run with a real time of 100ms. Visualisation outputs were divided into 100 time steps of 1ms each so as to give a realistic visualisation output of the simulation. The time dependant central difference method is used in the explicit integration scheme, thus making the integration conditionally stable whereby the stability depends primarily on the time step used. Time stepping in the explicit scheme can be made extremely small to maintain accuracy.

6.4 Finite Element Model Meshing

The finite element analysis is largely dependant on the number of elements used in a model. As the number of elements approach infinity in the finite element formulation, so the solution approaches the exact solution of the governing equations, provided the element formulation appropriately captures the physical phenomenon occurring. Therefore, an adequate number of elements must be used to ensure that an acceptable representation of the exact solution is found. However, as the number of elements increases so does the computational expense. Thus one must sacrifice accuracy for time or vice-versa. For this reason a reasonable balance should be attained between the two. An ideal model must have sufficient elements to accurately represent the model solution but also to maintain computational time to a suitable level.

Aspect ratio is another restrictive factor of a model. The aspect ratio is the ratio between the longer and shorter dimensions of an element. ABAQUS will terminate an analysis if the aspect ratio of an element is exceeded by a factor of more than 4 since the element will be considered excessively distorted. A small element can afford less expansion in a single direction than a larger element due to it having a smaller adjacent side.

Symmetry conditions were initially applied to the models. Symmetry conditions reduce computational time and file sizes of an analysis and also assist with reducing the potential of numerical round-off errors (which are critical for global bending/progressive folding type simulations). Quarter-symmetry was initially used as this cut computational time by a factor of four. Symmetrical boundaries were imposed about the x-z and y-z planes as shown in Figure 6.4. Elements were assigned a global size of 2mm. This meant that each element had a side length of approximately 2mm. It would make sense to have used symmetry if tubes were expected to crush in the progressive symmetric buckling mode. However, since most of the tubes lengths tested were expected to buckle in the transition or global bending zone, the final crushed shape of a tube may not have been axis-symmetric. Furthermore it was expected that if the tubes did buckle progressively it would have been in an asymmetric mixed mode, which would not have necessarily been axis-symmetric. A simulation of a quarter-symmetry model of a plate-divided specimen is shown in Figure 6.5. Although the simulation exhibited promising progressive buckling, unwanted deformation of the tube occurred at the very bottom of the model. This posed a difficulty in that symmetry could not be used to minimise computational time as a whole model approach had to be used. To compensate for the loss in computational time that was imposed, element size was increased slightly to a global size of 3mm as shown in Figure 6.6. Element sizes of 4mm and 5mm were also implemented but although this cut computational time, accuracy was compromised. As already mentioned, 4-noded 2-dimensional shell elements were used to model the tubes to further decrease computational time. The shells were then assigned a thickness of 1.6mm.

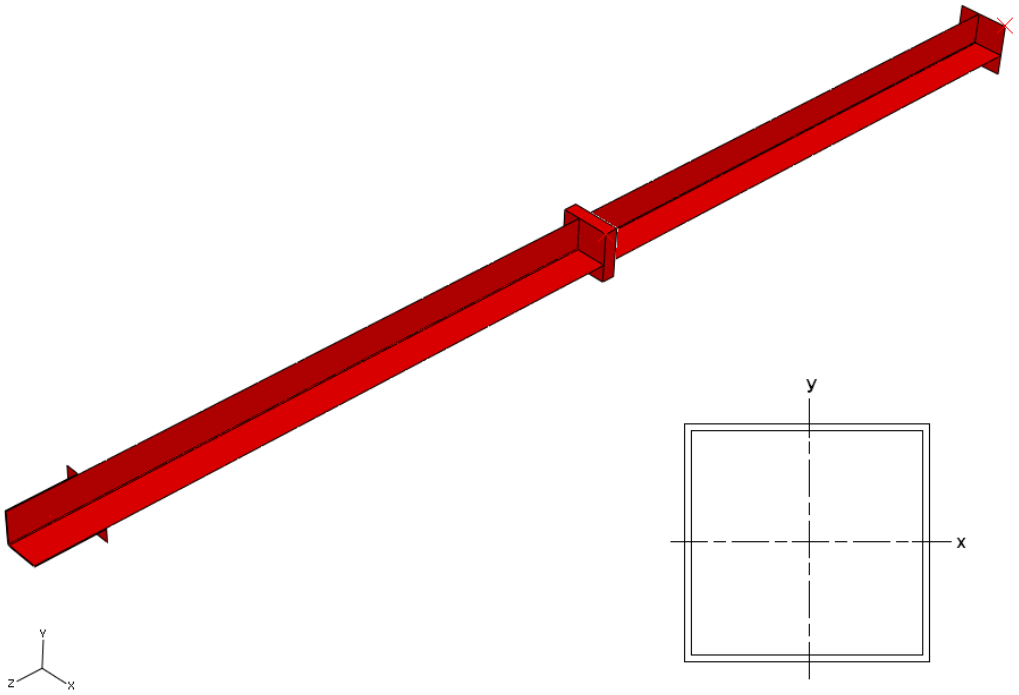

Figure 6.4: Quarter-symmetry model of plate-divided specimen.

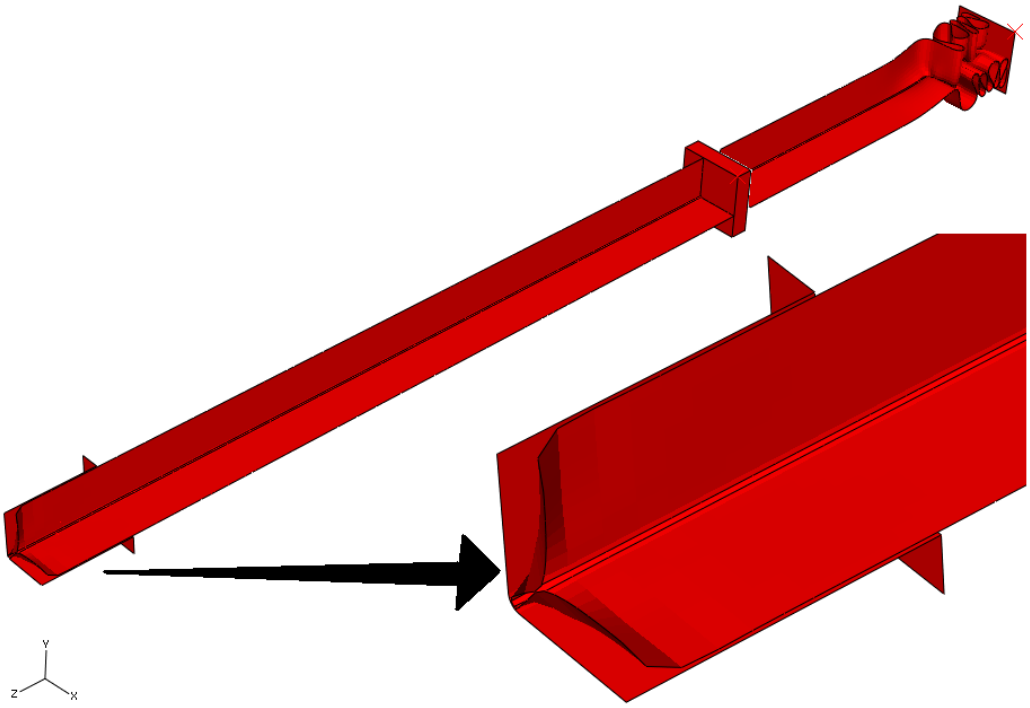

Figure 6.5: Quarter-symmetry simulation of plate-divided model that was rejected due to the deformation at the bottom of the bottom tube.

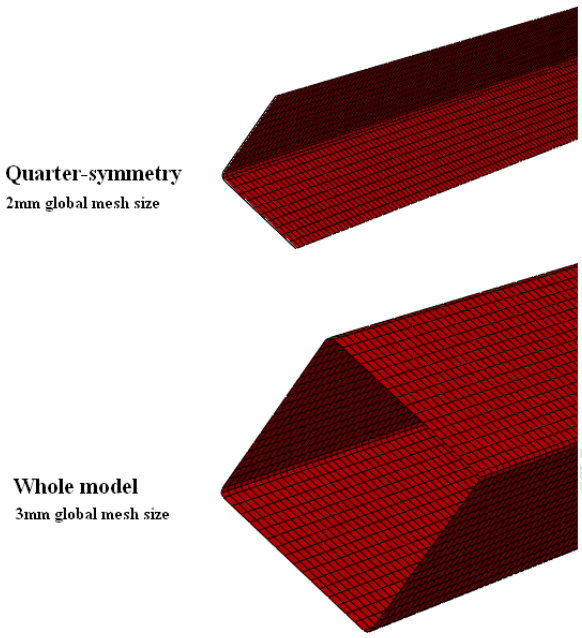

Figure 6.6: Meshes of quarter-symmetry and whole model tube.

6.5 Geometric Properties of Model Parts

Models of the three square tube specimen configurations were created. The models aimed to be simple while maintaining a level of good accuracy. In terms of geometry, the dimensions of the models were identical to the experimental specimens. They were also created so as to be easily modified. One parameter that was changed for every simulation was the lengths of the tubes. In order to simulate the boundary produced by the clamp and the likely movement of the plate and impact mass, boundary constraints were introduced into the models. Figure 6.7 is a labeled illustration of the single, welded and plate-divided models. Detailed descriptions of each part of the models are presented in the sub-sections 6.5.1-6.5.5.

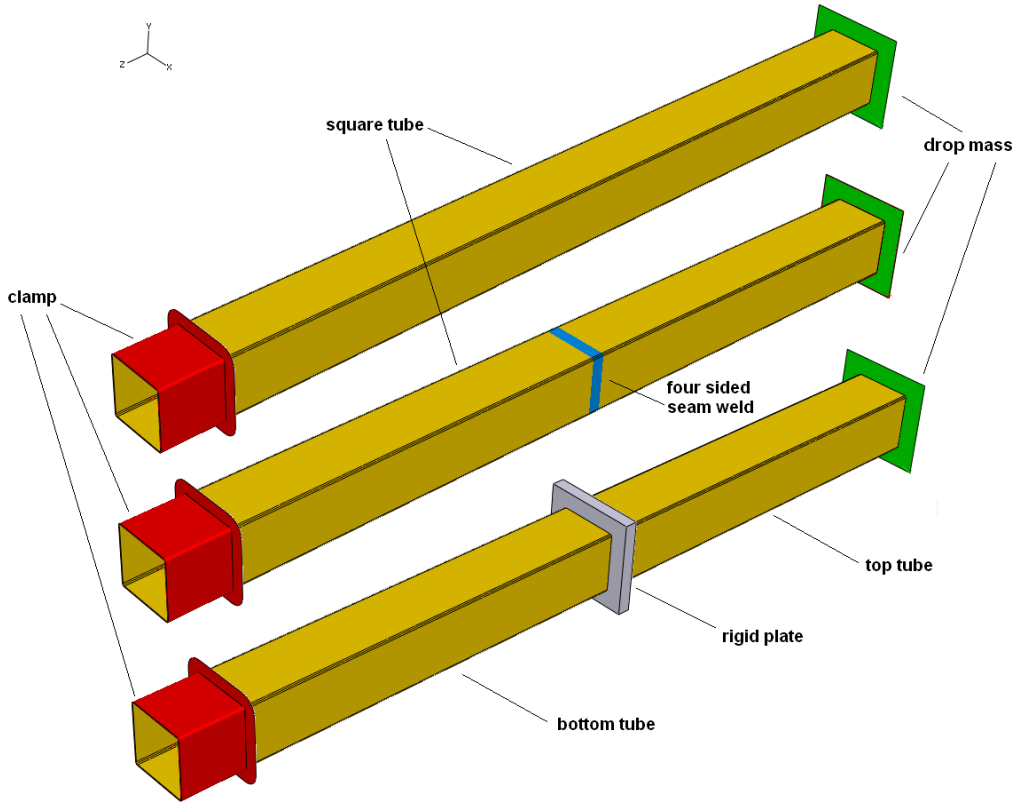

Figure 6.7: Labelled models of single, welded and plate divided specimens.

6.5.1 Clamp

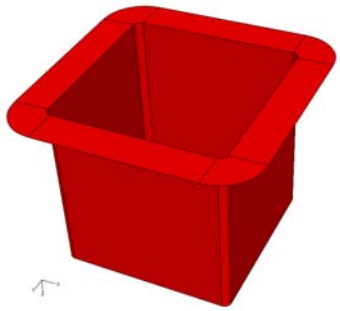

Figure 6.8: Clamp model

The clamp is common to all three configurations. It is modeled as a 3D rigid body (not deformable) and it is encastred which means that the rotational and lateral degrees of freedom fixed (not able to move in any direction).

6.5.2 Drop Mass

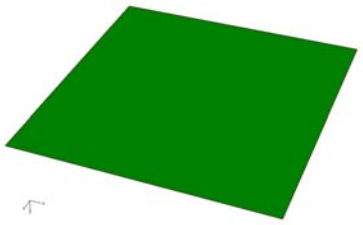

Figure 6.9: Drop mass model

The drop mass is common to all three configurations. It is modeled as a 2D rigid square body with a mass of 340kg. Although the actual drop mass is circular, the shape of the modelled drop mass is square. This is not a problem since the area of contact during impact remains the same regardless of the shape of the drop mass and because the model is rigid. Its Starting position is 0.01mm above specimen and it is given an initial velocity of 8m/s. It is influenced by gravitational acceleration of 9.81m/s^2. It is only able to move in z-direction and is unable to rotate.

6.5.3 Rigid plate

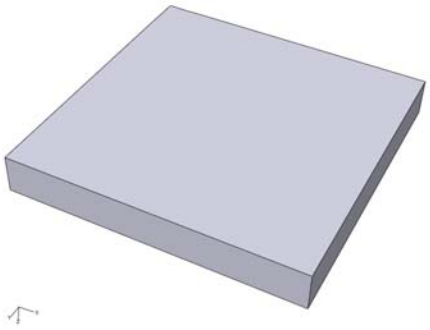

Figure 6.10: Rigid plate model

The rigid plate is only applicable to plate-divided models. It is modelled as a 3D rigid body with a mass of 0.44kg and dimensions 75mm × 75mm and a thickness of 10mm thickness. It is influenced by gravitational acceleration of 9.81m/s^2. It is only able to move in z-direction and is unable to rotate. When rotational degrees of freedom were assigned, irregular crushing and fly-out failures occurred in simulations.

6.5.4 Tube

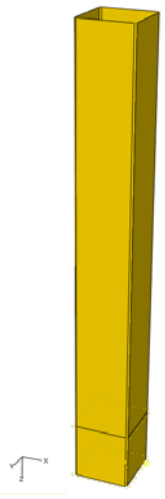

Figure 6.11: Tube model

The tube model is common to all three configurations. Two tubes are used in plate divided models. Each tube is modeled as a deformable, homogenous shell structure. The lengths of the tubes vary from 150mm to 1700mm and each tube model has a wall thickness of 1.6mm. The bottom 50mm of each tube model is for clamping with the clamp model. The tubes are assigned mild steel properties. The tube models have rotational and translational degrees of freedom in all directions.

6.5.5 Weld

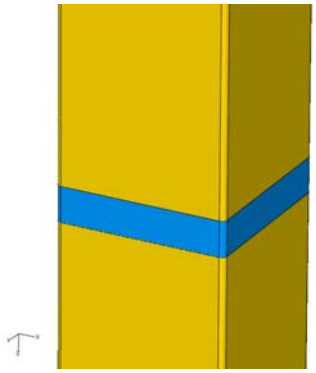

Figure 6.12: Weld model

The weld model only is only used in welded tube simulations. It is a simplified model, essentially it is modelled as a thicker part of a single tube. It is modelled as as a deformable, homogenous shell structure with a thickness of 2mm and a width of 10mm. It covers all four sides of a tube in welded tube simulations and it is assigned the same material properties of mild steel. The weld region is a partitioned section of a single tube half way along the crushable length of a single tube. It is not two tubes welded together as in experimental specimens. It is assigned rotational and translational degrees of freedom in all directions (as with tube).

6.6 Material properties of tube

Mild steel square tubes undergoing impact loading conditions deform at relatively high strain rates causing a slight increase in temperature due to the strain rate. Some material properties such as yield strength can change as a result of a change in temperature and strain rate. Two models that can be used to model high strain rate deformations are the *Johnson-Cook plasticity model* and *the Classical metal plasticity model.* The Johnson-Cook plasticity model is a particular type of Mises plasticity model with analytical forms of the hardening law and rate dependence. It is a particular type of isotropic hardening and is typically used in adiabatic transient dynamic simulations. The Johnson-Cook model is only valid up to the melting temperature. However, the Johnson-Cook model requires extensive information describing the material constants that depend on the transitional temperature. By touching the crushed region of a tube directly after a test it is noticeably warmer than the non-deformed part of the tube. During tube crushing temperature in the crushed region increases but not by a very significant amount. The Johnson-Cook model was not included in the scope of this study as it is better suited for dealing with models with large temperature differences.

The classical metal plasticity model was used for this study. It uses standard Mises yield surfaces associated with plastic flow, which allow for isotropic and anisotropic yield respectively. It involves using stress-strain data from uni-axial tensile tests that are modified for strain hardening, strain rate and temperature dependencies.

6.6.1 Strain Hardening

In most materials elastic or Young's modulus describes the elastic region while, for the plastic region, true stress and true (logarithmic plastic) strain data are required. Mild steel is an isotropic material and engineering stress-strain data obtained from tensile tests is converted to true stress-strain by

$$\sigma_{true} = \sigma_{nom}\left(1 + \varepsilon_{nom}\right) \tag{6.1}$$

$$\varepsilon_{true} = \ln\left(1 + \varepsilon_{nom}\right) \tag{6.2}$$

where σ_{true} : true stress; σ_{nom} : nominal stress; ε_{nom} : nominal strain: ε_{true} : true strain

Figure 6.13 shows the true stress-true strain graph for mild steel.

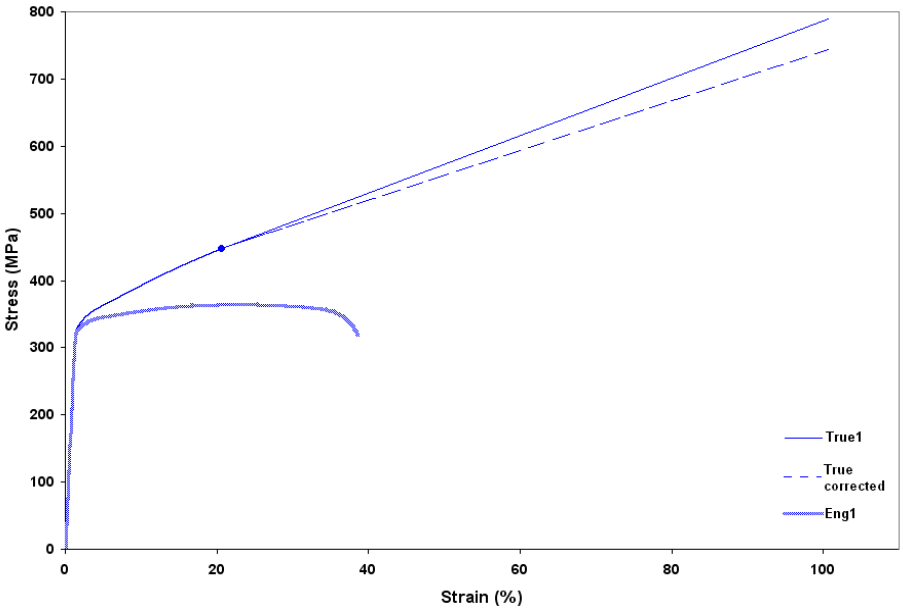

Figure 6.13: True stress – true strain curve and corrected stress using Mirone correction [48, 49].

6.6.2 Strain Rate Dependence

The von Mises yield criterion with isotropic hardening is a suitable model to characterise the plastic properties of the mild steel tubes since mild steel typically exhibits linear elastic and isotropic strain hardening plastic behaviour. Strain rate hardening is modelled using the Cowper-Symonds relation:

$$\sigma_y^d / \sigma_y = 1 + \left(\dot{\varepsilon}/D\right)^{1/q} \tag{6.3}$$

where σ_y^d : dynamic yield stress; σ_y : static yield stress; $\dot{\varepsilon}$: strain rate; $D = 844s^{-1}$ and $q = 2.207$ (these are values obtained for South African mild steel from Hopkinson bar tests [25]).

6.6.3 Temperature Dependence

Because heat, generated during tube crushing as a result of plastic work, may cause changes in material properties but not significantly alter the overall behaviour of the tube, temperature dependency was incorporated in the material model using Masui's model [50]. The temperature rise due to the plastic strain is computed using the specific heat of the metal while the Young's Modulus and the true stress-logarithmic plastic strain data are put in tabular form for different temperatures. ABAQUS/Explicit determines the exact Young's Modulus and strain by linearly interpolation of the tabulated values. The initial temperature was chosen to be 293K (20°C). Table 6.1 summarises the material properties of mild steel at a temperature of 293K.

Table 6.1 Summary of material properties of the test tube used in FEM (Temp = 293K or 20°C)

Property	*Symbol*	*Value*
Young's Modulus	E	210 GPa
Poisson's Ratio	ν	0.3
Static Yield Stress	σ_y	328 MPa
Density	ρ	7850 kg/m^3
Specific Heat	c	450 J/kg/K

6.6.4 Contact modelling

In order to simulate the interactions between the tube walls and the rigid drop mass, contact in the form of "self-contact" is defined for the whole model to allow both the inside and outside walls of the tubes to interact with each other and the drop mass with the tube.

Self contact is generally available in the context of a surface folding and touching itself in ABAQUS/*Explicit.* Contact elements are internally generated for each node on the contact surfaces to allow contact of all surface segments. A penalty is used to avoid over-constraining that will occur, for example, if the meshes on both sides of the interface match exactly since a node is simultaneously a master and a slave. The penalty contact algorithm has a weaker enforcement of contact constraints but allows for treatment of more general types of contact. The algorithm, nevertheless, conserves momentum between the contacting bodies.

Self-contact between all bodies was applied in the model. Contact surfaces that are taken into consideration are the contact between tubes and the plate surfaces in plate divided models, and between tubes and the drop mass in all models. Although there is a contact surface between the bottom 50mm of each tube and the clamp, these two surfaces do not move relative to each other. A dynamic coefficient of 0.3 was used in simulations.

7. SIMULATION RESULTS AND ANALYSIS

The results obtained from the numerical simulations of the impact loading of mild steel square tubes, including single, welded and plate-divided configurations from **Group C** are presented in this chapter. Finite element results include time response, final crushed distances, energy absorption and force/displacement graphs. Buckling modes are analysed and simulations are compared to experimental results in terms of geometric efficiency and specific energy. While force/displacement graphs would be ideal to correlate FEM with experiments, experimental data on forces was not available due to limitations in instrumentation. A typical ABAQUS input deck of a plate-divided model is included in Appendix A.

7.1 Time Response

To ascertain the accuracy of the simulations and their correlation with experimental results, time response was analysed. High-speed footage of dynamic tests on some welded square tube specimens in **Group B** was obtained. Using software provided with the high-speed camera, snapshots of the high-speed footage could be obtained and displacement of a specimen at various time points could be measured. The progressive buckling sequence obtained from high-speed camera footage of a 400mm (200w200) seam welded specimen is shown in Figure 7.1. The equivalent FEM simulation sequence is shown below it. The displacement history of the experimental specimen and FEM model is shown in Figure 7.2. The individual snapshots in the two sequences are lettered (a) – (j) and these points are also shown in the displacement histories. Although there was a difference in final displacement between the experimental specimen and numerical model, the time taken to crush the specimen to a maximum was the same in both methods. The time taken to crush the specimen from when the drop mass came into contact with it, was 70ms. The good correlation between these results for the time response indicated that the numerical simulations were capable of making accurate predictions of the behaviour of square tubes during dynamic axial loading.

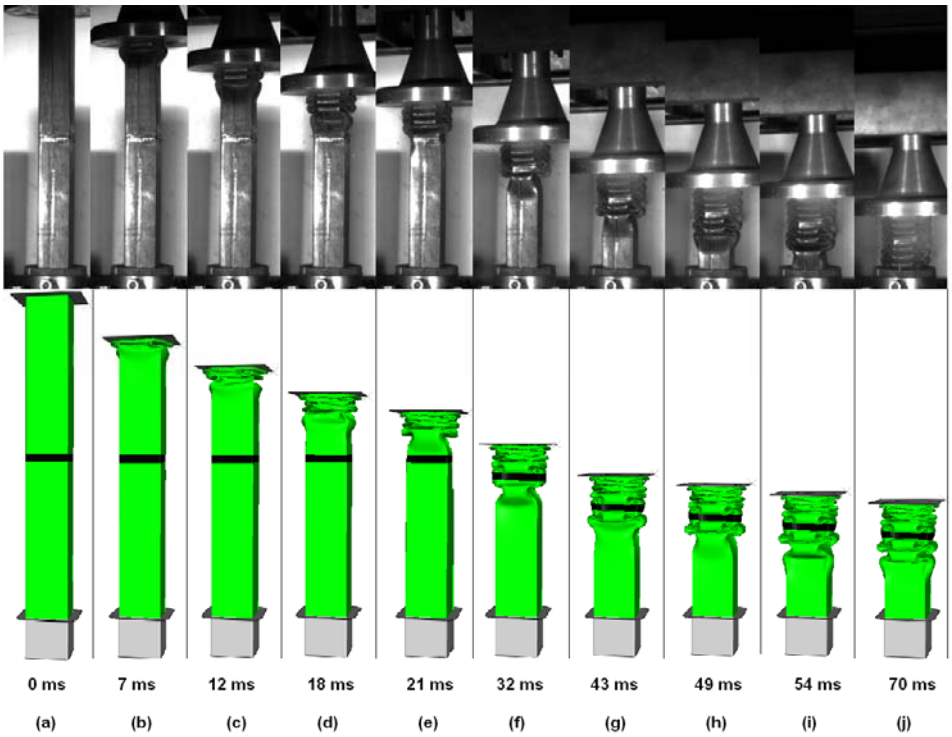

Figure 7.1: High-speed camera footage and FEM simulation showing progressive buckling of a 400mm (200w200) welded specimen. Drop height = 3.26m (V = 8m/s).

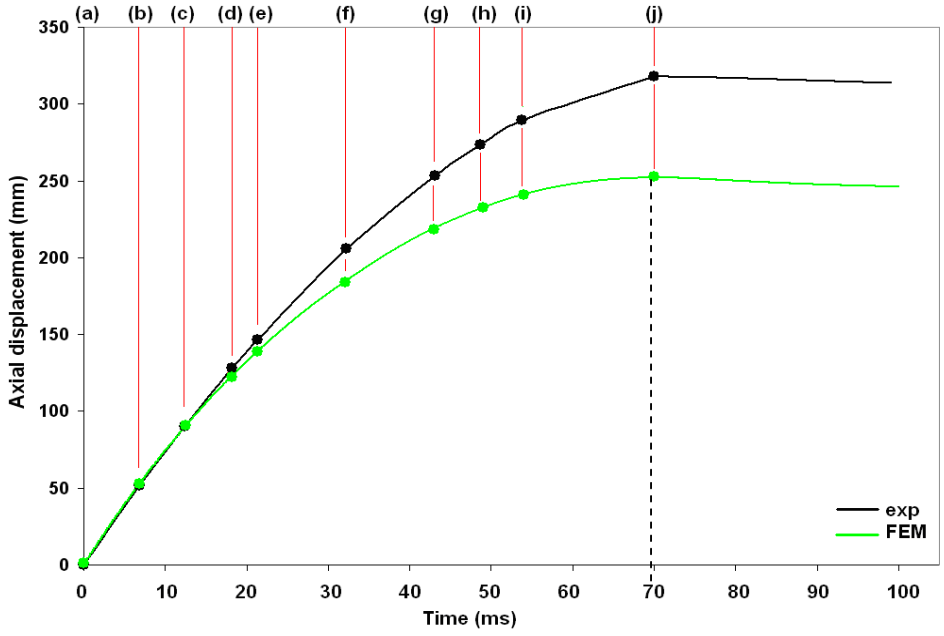

Figure 7.2: Displacement history of experimental specimen acquired using high-speed footage and FEM simulation model of 200w200. Drop height = 3.26m (V = 8m/s).

Observation of the output visualisation of the crushing process in numerical models revealed that after the tube had been crushed to a maximum, the tube would exhibit elastic or spring-like behaviour causing the drop mass to bounce back a bit. This was also observed in high-speed footage. This behaviour can also be seen in the displacement-time graphs shown in Figure 7.3 which shows the displacement histories of 600mm and 1600mm single, welded and plate-divided numerical simulations. The maximum displacement of a tube is not necessarily the final displacement. For the 600mm simulations the models were crushed to a maximum between 55ms and 60ms and then the displacement oscillated slightly as the models sprung back slightly. The 1600mm simulations revealed the same behaviour after a maximum displacement was reached at 65ms.

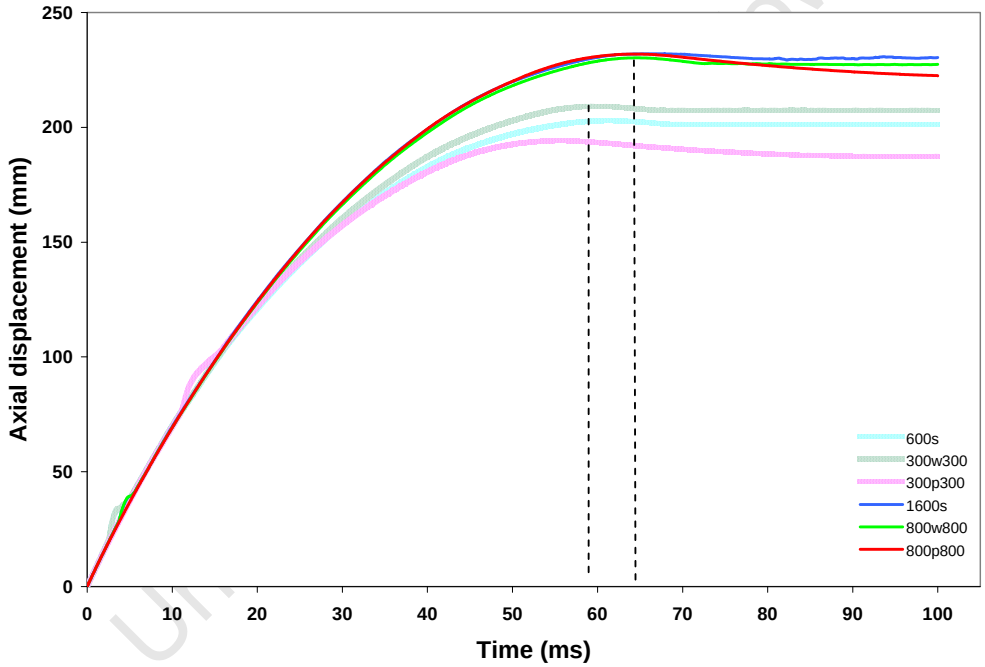

Figure 7.3: Displacement history of 600mm and 1600mm single, welded and plate-divided specimens with dashed lines indicating maximum displacement.

7.2 Comparison of Experimental and Numerical Results

Table 7.1 shows the results of final displacement and energy absorption in experimental tests and numerical modeling. Errors in terms of percentage are also shown.

8. CONCLUSIONS

The crushing of axially loaded single, welded and plate-divided square tube specimens were investigated experimentally and numerically. Based on the findings of this investigation, the following conclusions may be drawn:

Quasi-Static Tests

Single, welded and plate-divided specimens with lengths ranging from 400mm to 800mm were quasi-statically axially loaded. The tubes all had width-to-thickness ratios of 31.25. For this width-to-thickness ratio Abramowicz and Jones [12] predicted that buckling would change from progressive to global bending in single tubes at a critical length-to-width aspect ratio of 6.49. Their experimental data yielded an increase of this ratio to 8.91. Results showed that for single tubes global bending first occurred in single tubes at 800mm (critical length-to-width aspect ratio of 16). For welded and plate-divided tube specimens, global bending occurred at 750mm (critical length-to-width aspect ratio of 15). No transition buckling was observed, confirming findings by Abramowicz and Jones [12]. **Force-displacement curves revealed that welded tubes behaved very similarly to single tubes in that they exhibited one peak load**. **In plate-divided specimens, however, two ultimate peak loads were observed and in turn this slightly increased the mean load (about 1kN) experienced by the specimens compared to single and welded tube specimens.**

Dynamic Tests

The focus of dynamic axial testing lay on single, welded and plate-divided specimens with lengths ranging from 550mm to 1700mm. These tests were all performed with a drop mass of 340kg and a drop height of 3.26m (V = 8m/s). As with quasi-static specimens, the tubes all had width-to-thickness ratios of 31.25. For this width-to-thickness ratio Abramowicz and Jones [12] predicted that transition buckling would occur in single tubes at about 600mm while global bending would occur at about 1500mm. As predicted by Abramowicz and Jones [12] in single tube specimens, transition buckling was first observed in a 600mm specimen. In welded specimens,

transition buckling was first observed in a 550mm specimen. Global bending only occurred in one welded specimen, 800w800 (1600mm). Global bending was not observed in single tube specimens. In plate-divided specimens, transition and global bending did not occur as all the specimens buckled in a progressive manner. In 1500mm (750p750) and 1600mm (800p800) plate-divided specimens, fly-outs occurred after progressive buckling occurred. In general the axial displacements did not vary much between the three configurations and there was no consistency in terms of which configuration crushed more for a specific length, but holistically, plate divided specimens could be considered the most reliable configuration as they did not exhibit transition and global bending. **The frictional forces at the tubes and plate contact interfaces were not enough to overcome slight lateral movement of the plate and upper tube. It is this lateral degree of freedom in plate-divided specimens which hindered the onset of transition or global bending and allowed progressive buckling to take place**. Of the three tube configurations, welded specimens performed the worse as irregular folding and transition buckling occurred more often in these specimens. Any slight inaccuracy in lining up the tubes when welded would cause buckling in the weld region or transition buckling to occur as a result of the geometric instability.

In addition, single and welded tubes with lengths of 300mm, 400mm and 500mm were tested at different drop heights and compared with plate-divided specimens in **Group A**. Results showed that for these lengths single tubes were slightly more efficient than welded tubes with a maximum difference in axial displacement of 24mm observed in 300mm specimens with a drop height of 1.69m. Plate-divided specimens, however, were considerably less efficient with axial displacement differing from 50mm to 100mm for various drop heights. The difference in axial displacement could also have been attributed to the fact that the plate-divided specimens were made from a different set of mild steel tubes than the single and welded tube specimens. Thus different material properties may have existed for the two batches of mild steel tubes. Furthermore, re-measurement of the specimens showed that the wall thicknesses of the single and welded tubes were closer to 1.5mm than 1.6mm as measured for the plate-divided specimens. **The difference in wall thickness had a significant effect on crush distance.**

Finite Element Results

ABAQUS/*Explicit* was used in the analysis of single, welded and plate-divided square tubes subjected to axial impact loading and it accurately predicted the axial displacements, forces and energy required in crushing these tubes. The success of the simulations can be attributed to appropriate use of parameters such as material properties, element types, mesh sizes and whole modeling instead of axis-symmetric modeling. Axis-symmetric modeling is useful in short tube specimens where it is known that square tubes will buckle in a progressive manner but when it comes to simulating transition or global bending, whole modeling needs to be used. The results obtained are very promising, especially with concern to plate-divided specimens, as these type of specimens had never been modelled before.

Time Response

Finite element simulations produced remarkable correlation with high-speed footage in terms of time response. **The time taken to crush a mild steel 50mm×50mm×1.6mm square tube with a drop mass of 340kg and a drop height of 3.26m is between 65 and 70ms.** The finite element simulations predicted this time exactly in all cases and this served as a verification of the accuracy of the finite element model.

Buckling Modes

Apart from symmetric and extensional lobe layers observed in progressive buckling, behaviour such as fly-out failures and transition buckling were accurately predicted by the finite element models. Even though in experimental tests transition buckling occurred in some shorter specimens, progressive buckling was observed even in the longest specimens of 1700mm. The numerical model of 1400s was the only simulation that exhibited transition buckling characterised by progressive buckling and global bending. All single and welded tube simulations with lengths of 1300mm onwards exhibited a large amount of lateral movement or sway, suggesting that transition buckling may have occurred if drop height or drop mass had been increased. A simple trigger introduced into a 1700mm model showed that a small deviation in

thickness on the one side of a tube was enough to initiate global bending after initial progressive buckling, thus creating a good example of transition buckling. As with experimental findings, plate-divided simulations did not exhibit any transition or global bending.

Although the modelling of the weld region was simplified and did not account for the slight changes in material properties that would be found in the heat affected zone, the simulations of welded tubes produced adequate results. Simulations showed that as in experimental findings, **lobe layers at the weld region would be slightly larger than lobe layers elsewhere along a specimen since the effective thickness at this point was slightly larger.**

Of particular interest were the fly-out failures that occurred in simulations of plate-divided specimens with lengths of 550mm (275p275) and less. This behaviour was consistent with observations in **Group A** tests in which fly-out failures were common occurrence in short plate-divided specimens. To avoid fly-out failures in plate-divided specimens, further constraints had to be applied to the top tube.

Change in Wall Thickness

Simulations on 300mm, 400mm and 500mm single and welded tubes showed that **by changing the wall thickness from 1.6mm to 1.5mm, and keeping load conditions the same, crush distance would increase significantly (by 31% in the most extreme case) while peak and mean loads would decrease by a considerable amount (about 9kN for peak loads and between 6kN and 8kN for mean loads).**

9. RECOMMENDATIONS

As a result of the findings and conclusions of this dissertation, the following recommendations are made:

- Additional tests should be carried out on single, welded and plate-divided tube specimens with 50mm×50mm×1.6mm cross-sections at different drop heights and different drop masses to observe the affect on buckling modes as a result of different loading conditions.

- More tests with different width-to-thickness ratios (C/H) should be performed to confirm or disprove the trends established by Abramowicz and Jones [12] and possibly obtain similar empirical equations for transition buckling behaviour in quasi-static and dynamic tests.

- Single square tube specimens that are likely to buckle in the global bending mode should be tested along with two axially stacked plate-divided tube specimens that individually are likely to buckle in the progressive region but whose combined length is in the global bending region. This would establish whether two axially stacked plate-divided tube specimens can feasibly be used to replace single tubes in structural applications.

- The finite element model should be altered for welded tube simulations to take into account the slightly different material properties associated with the HAZ and weld metal.

- Transition and global bending should be further investigated in finite element simulations to ascertain whether these buckling modes emerge on their own accord without the assistance of thermal or geometric triggers.

8. REFERENCES

[1] Wikipedia online encyclopedia. *Car accident.* http://en.wikipedia.org/wiki/Car_accident

Last accessed 17 November 2008

[2] Jones, N. *Structural Impact.* Cambridge University Press. (1989) 333-519.

[3] Jones, N. *Several phenomena in structural impact and structural crashworthiness.* European Journal of Mechanics A/Solids 22 (2003) 693-707.

[4] Shin, K.C., Lee, J.J., Kim, K.H., Song, M.C. and Huh, J.S. *Axial crush and bending collapse of an aluminium/GFRP hybrid square tube and its energy absorption capability.* Composite Structures 57 (2002) 279-287.

[5] Kim, D.K., Lee, S., and Rhee, *M. Dynamic crushing and impact energy absorption of extruded aluminium square tubes.* Material and Design 19 (1998) 179-185.

[6] Tarigopula, V., Langseth, M., Hopperstad, O.S., and Clausen, A.H. *Axial crushing of thin-walled high-strength steel sections.* International Journal of Impact Engineering 32 (2006) 847-882.

[7] Abramowicz, W. and Jones, N. *Dynamic progressive buckling of circular and square tubes.* International Journal of Impact Engineering 4.4 (1986) 243-270.

[8] Arnold, B. and Altenhof, W. *Experimental observations on the crush characteristics of AA6061 T4 and T6 structural square tubes with and without circular discontinuities.* International Journal of Crashworthiness 9.1 (2004) 73-87.

[9] Jensen, Ø., Langseth, M. and Hopperstad, O.S. *Experimental investigations on the behaviour of short to long square aluminium tubes subjected to axial loading*. International Journal of Impact Engineering 30 (2004) 973-1003.

[10] Chung Kim Yuen S. and Nurick G.N. *The energy absorbing characteristics of tubular structures with geometric and material modifications: an overview.* Applied Mechanics Reviews 61 (2008) 1-15.

[11] Andrews, K.R.F., England, G.L. and Ghani, E. *Classification of the axial collapse of cylindrical tubes under quasi-static loading.* International Journal of Mechanical Sciences 25 (1983) 687-696.

[12] Abramowicz, W. and Jones, N. *Transition from global bending to progressive buckling of tubes loaded statically and dynamically.* International Journal of Impact Engineering 19.5 (1997) 415-37.

[13] Jensen, O., Hopperstad, O. S. and Langseth, M. *Transition from progressive to global buckling of aluminium extrusions – a numerical study.* IJCrash (2005) 601-620.

[14] Karagiozova, D. and Alves, M. *Transition from progressive buckling to global bending of circular shells under axial impact—Part I: Experimental and numerical observations*. International Journal of Solids and Structures 41 (2004) 1565-1580.

[15] Karagiozova, D. and Alves, M. *Transition from progressive buckling to global bending of circular shells under axial impact—Part II: Theoretical analysis*. International Journal of Solids and Structures 41 (2004) 1581-1604.

[16] Tan, P. *New R56 MINI Cooper Crash Test - 5 Stars!* http://paultan.org/archives/2007/04/20/new-r56-mini-cooper-crash-test-5-stars/

[17] US department of transport. *Train to train impact test of crash energy management passenger rail equipment.* www.fra.dot.gov/downloads/Research/rr0705.pdf

[18] Alghamdi, A.A.A. *Collapsible impact energy absorbers: an overview.* Thin-walled structures 39 (2001) 189-213.

[19] Starbuck, J.M and Boeman, R.G. *Crash Analysis of Adhesively Bonded Structures.* Automotive Lightweighting Materials. FY 2004 Progress Report. 221-228.

[20] White, M.D. and Jones, N. *Experimental quasi-static axial crushing of top-hat and double-hat thin-walled sections.* International Journal of Mechanical Sciences 41 (1999) 179-208.

[21] White, M.D. and Jones, N. *A theoretical analysis for the quasi-static axial crushing of top-hat and double-hat thin-walled sections*. International Journal of Mechanical Sciences 41 (1999) 209-233.

[22] Kim, T.H and Reid, S.R. *Bending collapse of thin-walled rectangular section columns.* Computers & Structures 79 (2001) 1897-1911.

[23] Morris, E., Olabi, A.G. and Hashmi, M.S.J. *Lateral crushing of circular and non-circular tube systems under quasi-static conditions.* Journal of Materials Processing Technology 191 (2007) 132-135.

[24] Abramowicz, W. *Thin-walled structures as impact energy absorbers.* Thin-Walled structures 41 (2003) 91-107.

[25] Marais, S.T., Tait, R.B., Cloete, T.J. and Nurick, G.N. *Material testing at high strain rate using the split Hopkinson pressure bar.* Latin American Journal of Solids and Structures**,** 1(3) (2004) 319-338.

[26] Filippov, S.B., Haseganu, E.M., and Smirnov, A.L. *Free vibrations of square elastic tubes with a free end.* Mechanics Research Communications 27 (2000) 457-464.

[27] Karagiozova, D. *Dynamic buckling of elastic-plastic square tubes under axial impact-I: Stress wave propagation phenomenon.* International Journal of Impact Engineering 30 (2004) 143-166.

[28] Karagiozova, D. and Jones, N. *Dynamic buckling of elastic-plastic square tubes under axial impact-II: Structural Response.* International Journal of Impact Engineering 30 (2004) 167-192.

[29] Langseth, M., Berstad, T., Hopperstad, O.S. and Clausen, A.H. *Energy absorption in axially loaded square thin-walled aluminium extrusions.* Structures Under Shock Impact III, CMP, Southampton (1994) 401-410.

[30] Abah, L., Limam, A. and Dejeammes, M. *Effects of cutouts on static and dynamic behaviour of square aluminium extrusions.* Fifth International Conference on Structures under Shock and Impact, (SUSI V), Computational Mechanics, Southampton (1998) 133-142.

[31] Marshall, N. and Nurick, G.N. *The effect of induced imperfections on the formation of the first lobe of symmetric progressive buckling of thin-waled square tubes*. Structures Under Shock and Impact, (SUSI V), Computational Mechanics, Southampton (1998) 155-168.

[32] Gupta, N.K. and Gupta, S.K. *Effect of annealing, size and cut-outs on axial collapse behaviour of circular tubes.* International Journal of Mechanical Sciences 35 (1993) 597-613.

[33] Lee, S., Hahn, C., Rhee, M. and Oh, J.E. *Effect of triggering on the energy absorption capacity of axially compressed aluminum tubes*. Materials & Design, Volume 20 (1999) 31-40.

[34] DiPaolo, B.P., Monteiro, P.J.M. and Gronsky, R. *Quasi-static axial crush response of a thin-wall, stainless steel box component*. International Journal of Solids and Structures 41 (2004) 3707-3733.

[35] Mamalis, A.G., Manolakos, D.E., Viegelahn, G.L., Vaxevanidis, N.M. and Johnson, W. *The inextensional collapse of grooved thin-walled cylinders of PVC under axial loading.* International Journal of Impact Engineering 4 (1986) 41-56.

[36] Chung Kim Yuen S. and Nurick G.N. *The crushing charateristics of square tubes with blast-induced imperfections - Part I: Experiments.* Journal of Applied Mechanics – To appear 2009.

[37] Seitzberger, M., Rammerstorfer, F.G., Gradinger, R., Degischer, H.P., Blaimschein, M. and Walch, C. *Experimental studies on the quasi-static axial crushing of steel columns filled with aluminium foam.* International Journal of Solids and Structures 37.30 (2000) 4125-47.

[38] Hanssen, A. G., M. Langseth, and O. S. Hopperstad. *Static and dynamic crushing of square aluminium extrusions with aluminium foam filler*. International Journal of Impact Engineering 24.4 (2000) 347-83.

[39] Reddy, T. Y. and S. T. S. Al-Hassani. *Axial crushing of wood-filled square metal tubes.* International Journal of Mechanical Sciences 35.3/4 (1993) 231-246.

[40] Theobald, M. D. and G. N. Nurick. *Numerical investigation of the response of sandwich-type panels using thin-walled tubes subject to blast loads.* International Journal of Impact Engineering 34.1 (2007) 134-56.

[41] Rodrigues, D.M., Menezes, L.F., Loureiro, A. and Fernandes, J.V. *Numerical study of the plastic behaviour in tension of welds in high strength steels*. International Journal of Plasticity 20 (2004) 1-18.

[42] Kim, J., Kim, Y.W., Kang, B.S. and Hwang, S.M. *Finite element analysis for bursting failure prediction in bulge forming of a seamed tube*. Finite Elements in Analysis and Design 40 (2004) 953-966.

[43] Zhao, K.M., Chun, B.K. and Lee, J.K. *Finite element analysis of tailor-welded blanks*. Finite Elements in Analysis and Design 37 (2001) 117-130.

[44] Abdullah, K., Wild, P.M., Jeswiet, J.J. and Ghasempoor, A. *Tensile testing for weld deformation properties in similar gage tailor welded blanks using the rule of mixtures*. Journal of Materials Processing Technology (2001) 91-97.

[45] Cam, G., Erim, S., Yeni, C. and Kocak, M. *Determination of mechanical and fracture properties of laser beam welded steel joints.* Technical report, American Welding Society and the Welding Research Council (1999). Supplement to the Welding Journal.

[46] Shigley, J.E., Mischke, C.R., and Budynas, R.G. *Mechanical Engineering Design.* McGraw-Hill. (2004) 72-75.

[47] Bonorchis, D. *Analysis and simulation of welded plates subjected to blast loading*. PhD thesis, University of Cape Town (2007).

[48] Mirone, G. *A new model for the elastoplastic characterization and the stress-strain determination on the necking section of a tensile specimen.* International Journal of Solids and Structures 41 (2004) 3545-3564.

[49] Mirone, G. *Approximate model of the necking behaviour and application to the void growth prediction.* International Journal of Damage Mechanics 13 (2004) 241-261.

[50] Masui, T., Nunokawa, T. and Hiramatsu, T. *Shape correction of hot rolled steel using an on line leveler.* Journal of Japan Society for Technology of Plasticity 1, 1987.

APPENDIX A

Typical Input Deck in FEM

Plate-divided tube model 350p350

```
*Heading
 Deformation of 700mm plate-divided specimen (whole)
** Job name: Job-350p350wholeFINAL Model name: Model-1
*Preprint, echo=NO, model=NO, history=NO, contact=NO
**
** PARTS
*Part, name=Clamp
*Node
      1, -0.0250000004, 0.00200000009,           0.
      2, -0.0350000001, 0.00200000009,           0.
      3,        -0.023, -0.00999999978,          0.
      4,        -0.023,           0.,          0.
      5, 0.0250000004, 0.00200000009,           0.
      6, 0.0350000001, 0.00200000009,           0.
      7,         0.023, -0.00999999978,          0.
      8,         0.023,           0.,          0.
      •
      •
      •
      100, 0.0245636627,  0.049246978, 0.0500000007
      101, 0.0248019379, 0.0488677658, 0.0500000007
      102, 0.0249498561, 0.0484450422, 0.0500000007
      103, 0.0249498561, 0.00155495817, 0.0500000007
      104, 0.0248019379, 0.00113223249, 0.0500000007
      105, 0.0245636627, 0.000753020402, 0.0500000007
      106, 0.0242469795, 0.000436337024, 0.0500000007
      107, 0.0238677673, 0.000198062262, 0.0500000007
      108, 0.0234450419,  5.01441755e-05, 0.0500000007

**Generation of elements
*Element, type=R3D4
      1,  1,  2, 37, 48
      2, 48, 37, 38, 47
      3, 47, 38, 39, 46
      4, 46, 39, 40, 45
```

```
      5, 45, 40, 41, 44
      6, 44, 41, 42, 43
      7, 43, 42,  3,  4
      8,  5,  6, 49, 60
      •
      •
      •
      65, 36, 21, 13, 34
      66,  35, 103,  60,   5
      67, 103, 104,  59,  60
      68, 104, 105,  58,  59
      69, 105, 106,  57,  58
      70, 106, 107,  56,  57
      71, 107, 108,  55,  56
      72, 108,  27,   8,  55
*Node
    109,       -0.023,           0., 0.0250000004
*Nset, nset=Clamp-RefPt_, internal
109,
*Nset, nset=_PickedSet4, internal
 109,
*Nset, nset=RP_Clamp
 109,
*Nset, nset=Clamp, generate
   1,  109,    1
*Elset, elset=Clamp, generate
  1,  72,   1
*Elset, elset=Clamp, generate
  1,  72,   1
*Element, type=MASS, elset=_PickedSet4_Clamp_
*Mass, elset=_PickedSet4_Clamp_
1.,
*End Part
**
*Part, name=Mass
*Node
      1, -0.0359999985, -0.0260000005,           0.
      2, 0.00400000019, -0.0260000005,           0.
      3, 0.0439999998, -0.0260000005,           0.
      4, -0.0359999985, 0.0140000004,           0.
      5, 0.00400000019, 0.0140000004,           0.
      6, 0.0439999998, 0.0140000004,           0.
      7, -0.0359999985, 0.0540000014,           0.
      8, 0.00400000019, 0.0540000014,           0.
      9, 0.0439999998, 0.0540000014,           0.
*Element, type=R3D4
1, 1, 2, 5, 4
2, 2, 3, 6, 5
3, 4, 5, 8, 7
4, 5, 6, 9, 8
*Node
     10, 0.0439999998, -0.0260000005,  -4.89842545e-18
*Nset, nset=Mass-RefPt_, internal
10,
*Nset, nset=Mass, generate
 1, 10,  1
```

```
*Elset, elset=Mass, generate
 1,  4,  1
*Nset, nset=RP_Mass
10,
*Elset, elset=Mass, generate
 1,  4,  1
*Element, type=MASS, elset=RP_Mass_Mass_
5, 10
*Mass, elset=RP_Mass_Mass_
340.,
*End Part
**
*Part, name="rigid plate"
*Node
      1,           0.,  0.075000003, 0.00999999978
      2,           0.,  0.075000003,           0.
      3,           0., 0.0375000015, 0.00999999978
      4,           0., 0.0375000015,           0.
      5,           0.,           0., 0.00999999978
      6,           0.,           0.,           0.
      7, 0.0375000015,  0.075000003, 0.00999999978
      8, 0.0375000015,  0.075000003,           0.
      9, 0.0375000015, 0.0375000015, 0.00999999978
     10, 0.0375000015, 0.0375000015,           0.
     11, 0.0375000015,           0., 0.00999999978
     12, 0.0375000015,           0.,           0.
     13,  0.075000003,  0.075000003, 0.00999999978
     14,  0.075000003,  0.075000003,           0.
     15,  0.075000003, 0.0375000015, 0.00999999978
     16,  0.075000003, 0.0375000015,           0.
     17,  0.075000003,           0., 0.00999999978
     18,  0.075000003,           0.,           0.
*Element, type=C3D8R
1,  7,  8, 10,  9,  1,  2,  4,  3
2,  9, 10, 12, 11,  3,  4,  6,  5
3, 13, 14, 16, 15,  7,  8, 10,  9
4, 15, 16, 18, 17,  9, 10, 12, 11
*Node
     19,           0.,           0.,           0.
*Nset, nset="rigid plate-RefPt_", internal
19,
*Nset, nset=_PickedSet11, internal
 6,
*Nset, nset=RP_Plate
 19,
*Nset, nset=_PickedSet26, internal
 19,
*Nset, nset=Plate, generate
  1,  19,   1
*Elset, elset=Plate, generate
 1,  4,  1
*Nset, nset=_PickedSet29, internal, generate
  1,  18,   1
*Elset, elset=_PickedSet29, internal, generate
 1,  4,  1
** Section: Plate
*Solid Section, elset=_PickedSet29, material=Steel
1.,
*Element, type=MASS, elset=_PickedSet26_Mass_plate_
5, 19
```

```
*Mass, elset=_PickedSet26_Mass_plate_
0.44,
*End Part
**
*Part, name="tube (bottom)"
*Node
      1, 0.0227000006, 0.0483999997,  0.349999994
      2, 0.0241999999, 0.0469000004,  0.349999994
      3, 0.0241999999, 0.0469000004,           0.
      4, 0.0227000006, 0.0483999997,           0.
      5, -0.0227000006, 0.0483999997,  0.349999994
      6,           0., 0.0483999997,  0.400000006
      7, -0.0227000006, 0.0483999997,  0.400000006
      8, 0.0227000006, 0.0483999997,  0.400000006

      .

      .

      .

      9712, 0.0237606596, 0.00043933955,  0.373529404
      9713, 0.0237606596, 0.00043933955,  0.376470596
      9714, 0.0237606596, 0.00043933955,  0.379411757
      9715, 0.0237606596, 0.00043933955,  0.382352948
      9716, 0.0237606596, 0.00043933955,   0.38529411
      9717, 0.0237606596, 0.00043933955,  0.388235301
      9718, 0.0237606596, 0.00043933955,  0.391176462
      9719, 0.0237606596, 0.00043933955,  0.394117653
      9720, 0.0237606596, 0.00043933955,  0.397058815
*Element, type=S4R
      1,    1,   33, 1273,  266
      2,   33,    2,   34, 1273
      3,  266, 1273, 1274,  265
      4, 1273,   34,   35, 1274
      5,  265, 1274, 1275,  264
      6, 1274,   35,   36, 1275
      7,  264, 1275, 1276,  263
      8, 1275,   36,   37, 1276

      .

      .

      .

      9640, 9716, 1260, 1259, 9717
      9641,  829, 9717, 9718,  830
      9642, 9717, 1259, 1258, 9718
      9643,  830, 9718, 9719,  831
      9644, 9718, 1258, 1257, 9719
      9645,  831, 9719, 9720,  832
      9646, 9719, 1257, 1256, 9720
      9647,  832, 9720, 1272,   24
      9648, 9720, 1256,   32, 1272
*Node
   9721,           0., 0.0241999999,  0.400000006
*Nset, nset="tube (bottom)-RefPt_", internal
9721,
*Nset, nset=Monitor
 21,
*Nset, nset=tube_base
```

```
    6,    7,    8,   10,   15,   16,   20,   22,   23,   24,   25,
30,   31,   32,  298,  299
  300,  301,  302,  303,  304,  305,  306,  307,  308,  309,  310,
311,  345,  522,  523,  524
  525,  526,  527,  528,  529,  530,  531,  532,  533,  534,  535,
671,  833,  834,  835,  836
  837,  838,  839,  840,  841,  842,  843,  844,  845,  846,  963,
1225, 1242, 1243, 1244, 1245
 1246, 1247, 1248, 1249, 1250, 1251, 1252, 1253, 1254, 1255, 1272
*Elset, elset=tube_base
  491,  492,  493,  494,  495,  496,  497,  498,  499,  500,  501,
502,  503,  504,  505,  506
  539,  540, 2669, 2670, 2671, 2672, 2673, 2674, 2675, 2676, 2677,
2678, 2679, 2680, 2681, 2682
 2683, 2684, 2951, 2952, 5081, 5082, 5083, 5084, 5085, 5086, 5087,
5088, 5089, 5090, 5091, 5092
 5093, 5094, 5095, 5096, 5329, 5330, 9341, 9342, 9599, 9600, 9601,
9602, 9603, 9604, 9605, 9606
 9607, 9608, 9609, 9610, 9611, 9612, 9613, 9614, 9647, 9648
*Nset, nset=Tube, generate
    1,  9720,     1
*Elset, elset=Tube, generate
    1,  9648,     1
*Nset, nset=clamp
    1,    2,    5,    6,    7,    8,    9,   10,   11,   14,   15,
16,   17,   19,   20,   23
   24,   30,   31,   32,   33,  267,  268,  269,  270,  271,  272,
273,  274,  275,  276,  277
  278,  279,  280,  281,  282,  283,  284,  285,  286,  287,  288,
289,  290,  291,  292,  293
  294,  295,  296,  297,  298,  299,  300,  301,  302,  303,  304,
305,  306,  307,  308,  309
  310,  311,  312,  313,  314,  315,  316,  317,  318,  319,  320,
321,  322,  323,  324,  325
```

•

•

•

```
9641, 9642, 9643, 9644, 9645, 9646, 9647, 9648, 9649, 9650, 9651,
9652, 9653, 9654, 9655, 9656
 9657, 9658, 9659, 9660, 9661, 9662, 9663, 9664, 9665, 9666, 9667,
9668, 9669, 9670, 9671, 9672
 9673, 9674, 9675, 9676, 9677, 9678, 9679, 9680, 9681, 9682, 9683,
9684, 9685, 9686, 9687, 9688
 9689, 9690, 9691, 9692, 9693, 9694, 9695, 9696, 9697, 9698, 9699,
9700, 9701, 9702, 9703, 9704
 9705, 9706, 9707, 9708, 9709, 9710, 9711, 9712, 9713, 9714, 9715,
9716, 9717, 9718, 9719, 9720
*Elset, elset=clamp
  235,  236,  237,  238,  239,  240,  241,  242,  243,  244,  245,
246,  247,  248,  249,  250
  251,  252,  253,  254,  255,  256,  257,  258,  259,  260,  261,
262,  263,  264,  265,  266
  267,  268,  269,  270,  271,  272,  273,  274,  275,  276,  277,
278,  279,  280,  281,  282
  283,  284,  285,  286,  287,  288,  289,  290,  291,  292,  293,
294,  295,  296,  297,  298
```

•

•

•

```
9593, 9594, 9595, 9596, 9597, 9598, 9599, 9600, 9601, 9602, 9603,
9604, 9605, 9606, 9607, 9608
 9609, 9610, 9611, 9612, 9613, 9614, 9615, 9616, 9617, 9618, 9619,
9620, 9621, 9622, 9623, 9624
 9625, 9626, 9627, 9628, 9629, 9630, 9631, 9632, 9633, 9634, 9635,
9636, 9637, 9638, 9639, 9640
 9641, 9642, 9643, 9644, 9645, 9646, 9647, 9648
*Nset, nset=Mid
   1,   2,   5,   9,  11,  14,  17,  19,  33, 267, 268, 269, 270,
271, 272, 273
 274, 275, 276, 277, 278, 279, 280, 281, 328, 346, 347, 348, 349,
350, 351, 352
 353, 354, 355, 356, 357, 358, 359, 360, 491, 492, 493, 494, 495,
496, 497, 498
 499, 500, 501, 502, 503, 504, 505, 536, 654, 672, 673, 674, 675,
676, 677, 678
 679, 680, 681, 682, 683, 684, 685, 686
*Elset, elset=Mid
    1,    2,  235,  236,  237,  238,  239,  240,  241,  242,  243,
244,  245,  246,  247,  248
  249,  250,  507,  508,  541,  542,  543,  544,  545,  546,  547,
548,  549,  550,  551,  552
  553,  554,  555,  556, 2413, 2414, 2415, 2416, 2417, 2418, 2419,
2420, 2421, 2422, 2423, 2424
 2425, 2426, 2427, 2428, 2685, 2686, 2919, 2920, 2953, 2954, 2955,
2956, 2957, 2958, 2959, 2960
 2961, 2962, 2963, 2964, 2965, 2966, 2967, 2968, 4825, 4826, 4827,
4828, 4829, 4830, 4831, 4832
 4833, 4834, 4835, 4836, 4837, 4838, 4839, 4840, 5097, 5098, 5331,
5332, 5333, 5334, 5335, 5336
 5337, 5338, 5339, 5340, 5341, 5342, 5343, 5344, 5345, 5346, 7203,
7204, 7437, 7438, 7439, 7440
 7441, 7442, 7443, 7444, 7445, 7446, 7447, 7448, 7449, 7450, 7451,
7452, 9309, 9310, 9343, 9344
 9345, 9346, 9347, 9348, 9349, 9350, 9351, 9352, 9353, 9354, 9355,
9356, 9357, 9358, 9615, 9616
** Region: (Tube:Tube), (Controls:Default)
*Elset, elset=_I1, internal
    1,    2,    3,    4,    5,    6,    7,    8,    9,   10,   11,
12,   13,   14,   15,   16
   17,   18,   19,   20,   21,   22,   23,   24,   25,   26,   27,
28,   29,   30,   31,   32
   33,   34,   35,   36,   37,   38,   39,   40,   41,   42,   43,
44,   45,   46,   47,   48
   49,   50,   51,   52,   53,   54,   55,   56,   57,   58,   59,
60,   61,   62,   63,   64
```

•

•

•

```
9597, 9598, 9599, 9600, 9601, 9602, 9603, 9604, 9605, 9606, 9607,
9608, 9609, 9610, 9611, 9612
 9613, 9614, 9615, 9616, 9617, 9618, 9619, 9620, 9621, 9622, 9623,
9624, 9625, 9626, 9627, 9628
 9629, 9630, 9631, 9632, 9633, 9634, 9635, 9636, 9637, 9638, 9639,
9640, 9641, 9642, 9643, 9644
 9645, 9646, 9647, 9648
** Section: Tube
*Shell Section, elset=_I1, material=Steel
0.0016, 5
** Region: (Tube:Tube), (Controls:EC-1)
*Elset, elset=_I2, internal
  235,  236,  237,  238,  239,  240,  241,  242,  243,  244,  245,
246,  247,  248,  249,  250
  251,  252,  253,  254,  255,  256,  257,  258,  259,  260,  261,
262,  263,  264,  265,  266
  267,  268,  269,  270,  271,  272,  273,  274,  275,  276,  277,
278,  279,  280,  281,  282
  283,  284,  285,  286,  287,  288,  289,  290,  291,  292,  293,
294,  295,  296,  297,  298
  299,  300,  301,  302,  303,  304,  305,  306,  307,  308,  309,
310,  311,  312,  313,  314
```

•

•

•

```
9249, 9250, 9251, 9252, 9253, 9254, 9255, 9256, 9257, 9258, 9259,
9260, 9261, 9262, 9263, 9264
 9265, 9266, 9267, 9268, 9269, 9270, 9271, 9272, 9273, 9274, 9275,
9276, 9277, 9278, 9279, 9280
 9281, 9282, 9283, 9284, 9285, 9286, 9287, 9288, 9289, 9290, 9291,
9292, 9293, 9294, 9295, 9296
 9297, 9298, 9299, 9300, 9301, 9302, 9303, 9304, 9305, 9306, 9307,
9308
** Section: Tube
*Shell Section, elset=_I2, controls=EC-1, material=Steel
0.0016, 5
*End Part
**
*Part, name="tube (top)"
*Node
      1, -0.0227000006,           0.,  0.349999994
      2, -0.0227000006,           0.,           0.
      3,           0.,           0.,           0.
      4, 0.0227000006,           0.,           0.
      5,           0.,           0.,  0.349999994
      6, 0.0227000006,           0.,  0.349999994
      7, -0.0241999999, 0.00150000001,  0.349999994
      8, -0.0241999999, 0.00150000001,           0.
```

•

•

•

```
      8492, 0.0237606596, 0.00043933955,  0.014957265
```

```
      8493, 0.0237606596, 0.00043933955, 0.0119658122
      8494, 0.0237606596, 0.00043933955, 0.00897435937
      8495, 0.0237606596, 0.00043933955, 0.00598290609
      8496, 0.0237606596, 0.00043933955, 0.00299145305
*Element, type=S4R
      1,    1,   25, 1073,  277
      2,   25,   26, 1074, 1073
      3,   26,   27, 1075, 1074
      4,   27,   28, 1076, 1075
      5,   28,   29, 1077, 1076
      6,   29,   30, 1078, 1077
      7,   30,   31, 1079, 1078
      8,   31,   32, 1080, 1079
      •
      •
      •
8419, 1040, 8494, 8495, 1041
8420, 8494,  157,  156, 8495
8421, 1041, 8495, 8496, 1042
8422, 8495,  156,  155, 8496
8423, 1042, 8496, 1072,   22
8424, 8496,  155,    4, 1072
*Nset, nset=Monitor
 3,
*Nset, nset=tube_base
    1,    5,    6,    7,    9,   12,   13,   15,   18,   19,   21,
24,  271,  272,  273,  274
  275,  276,  277,  278,  279,  280,  281,  282,  283,  284,  285,
533,  534,  535,  536,  537
  538,  539,  540,  541,  542,  543,  544,  545,  546,  547,  795,
796,  797,  798,  799,  800
  801,  802,  803,  804,  805,  806,  807,  808,  809, 1057, 1058,
1059, 1060, 1061, 1062, 1063
 1064, 1065, 1066, 1067, 1068, 1069, 1070, 1071
*Elset, elset=tube_base
    1,  118,  235,  352,  469,  586,  703,  820,  937, 1054, 1171,
1288, 1405, 1522, 1639, 1756
 1873, 1874, 2107, 2224, 2341, 2458, 2575, 2692, 2809, 2926, 3043,
3160, 3277, 3394, 3511, 3628
 3745, 3862, 3979, 3980, 4213, 4330, 4447, 4564, 4681, 4798, 4915,
5032, 5149, 5266, 5383, 5500
 5617, 5734, 5851, 5968, 6085, 6086, 6319, 6436, 6553, 6670, 6787,
6904, 7021, 7138, 7255, 7372
 7489, 7606, 7723, 7840, 7957, 8074, 8191, 8192
*Nset, nset=Tube, generate
    1,  8496,     1
*Elset, elset=Tube, generate
    1,  8424,     1
*Nset, nset=Mid
    1,    5,    6,    7,    9,   12,   13,   15,   18,   19,   21,
24,  271,  272,  273,  274
  275,  276,  277,  278,  279,  280,  281,  282,  283,  284,  285,
533,  534,  535,  536,  537
  538,  539,  540,  541,  542,  543,  544,  545,  546,  547,  795,
796,  797,  798,  799,  800
  801,  802,  803,  804,  805,  806,  807,  808,  809, 1057, 1058,
```

```
1059, 1060, 1061, 1062, 1063
 1064, 1065, 1066, 1067, 1068, 1069, 1070, 1071
*Elset, elset=Mid
    1,  118,  235,  352,  469,  586,  703,  820,  937, 1054, 1171,
1288, 1405, 1522, 1639, 1756
 1873, 1874, 2107, 2224, 2341, 2458, 2575, 2692, 2809, 2926, 3043,
3160, 3277, 3394, 3511, 3628
 3745, 3862, 3979, 3980, 4213, 4330, 4447, 4564, 4681, 4798, 4915,
5032, 5149, 5266, 5383, 5500
 5617, 5734, 5851, 5968, 6085, 6086, 6319, 6436, 6553, 6670, 6787,
6904, 7021, 7138, 7255, 7372
 7489, 7606, 7723, 7840, 7957, 8074, 8191, 8192
** Section: Tube
*Shell Section, elset=Tube, material=Steel
0.0016, 5
*End Part
**
**
** ASSEMBLY
**
*Assembly, name=Assembly
**
*Instance, name=tube-1, part="tube (bottom)"
 1.14629304579965e-18,       -0.015,          0.5
*End Instance
**
*Instance, name=Clamp-1, part=Clamp
 1.40946282423116e-18,      -0.0158, 0.849999999999999
*End Instance
**
*Instance, name="tube (top)-1", part="tube (top)"
          0.,       -0.015,         0.14
*End Instance
**
*Instance, name="rigid plate-1", part="rigid plate"
     -0.0375,      -0.0283,          0.49
*End Instance
**
*Instance, name=Mass-1, part=Mass
-0.00399999999999999,      -0.0048,         0.14
*End Instance
**
*Node
      1, -0.0399999991, -0.0307999998,  0.140000001
*Nset, nset=_PickedSet64, internal, instance=tube-1
    6,    7,    8,   10,   15,   16,   20,   23,   24,   30,   31,
32,  298,  299,  300,  301
  302,  303,  304,  305,  306,  307,  308,  309,  310,  311,  345,
522,  523,  524,  525,  526
  527,  528,  529,  530,  531,  532,  533,  534,  535,  671,  833,
834,  835,  836,  837,  838
  839,  840,  841,  842,  843,  844,  845,  846, 1225, 1242, 1243,
1244, 1245, 1246, 1247, 1248
 1249, 1250, 1251, 1252, 1253, 1254, 1255, 1272
*Elset, elset=_PickedSet64, internal, instance=tube-1
  491,  492,  493,  494,  495,  496,  497,  498,  499,  500,  501,
502,  503,  504,  505,  506
  539,  540, 2669, 2670, 2671, 2672, 2673, 2674, 2675, 2676, 2677,
2678, 2679, 2680, 2681, 2682
 2683, 2684, 2951, 2952, 5081, 5082, 5083, 5084, 5085, 5086, 5087,
```

```
5088, 5089, 5090, 5091, 5092
 5093, 5094, 5095, 5096, 9341, 9342, 9599, 9600, 9601, 9602, 9603,
9604, 9605, 9606, 9607, 9608
 9609, 9610, 9611, 9612, 9613, 9614, 9647, 9648
*Nset, nset=_PickedSet65, internal, instance=tube-1
 9721,
*Nset, nset=RP_earth, instance=tube-1
 9721,
*Nset, nset=_PickedSet68, internal, instance=tube-1
    6,    7,    8,   10,   15,   16,   20,   23,   24,   30,   31,
32,  298,  299,  300,  301
  302,  303,  304,  305,  306,  307,  308,  309,  310,  311,  345,
522,  523,  524,  525,  526
  527,  528,  529,  530,  531,  532,  533,  534,  535,  671,  833,
834,  835,  836,  837,  838
  839,  840,  841,  842,  843,  844,  845,  846, 1225, 1242, 1243,
1244, 1245, 1246, 1247, 1248
 1249, 1250, 1251, 1252, 1253, 1254, 1255, 1272
*Elset, elset=_PickedSet68, internal, instance=tube-1
  491,  492,  493,  494,  495,  496,  497,  498,  499,  500,  501,
502,  503,  504,  505,  506
  539,  540, 2669, 2670, 2671, 2672, 2673, 2674, 2675, 2676, 2677,
2678, 2679, 2680, 2681, 2682
 2683, 2684, 2951, 2952, 5081, 5082, 5083, 5084, 5085, 5086, 5087,
5088, 5089, 5090, 5091, 5092
 5093, 5094, 5095, 5096, 9341, 9342, 9599, 9600, 9601, 9602, 9603,
9604, 9605, 9606, 9607, 9608
 9609, 9610, 9611, 9612, 9613, 9614, 9647, 9648
*Surface, type=NODE, name=_PickedSet64_CNS_, internal
_PickedSet64, 1.
*Rigid Body, ref node=Clamp-1.Clamp-RefPt_, elset=Clamp-1.Clamp
*Rigid Body, ref node=Mass-1.Mass-RefPt_, elset=Mass-1.Mass
** Constraint: Constraint-1
*Coupling, constraint name=Constraint-1, ref node=_PickedSet65,
surface=_PickedSet64_CNS_
*Kinematic
3, 3
** Constraint: rigid
*Rigid Body, ref node="rigid plate-1".RP_Plate, elset="rigid plate-
1".Plate, position=CENTER OF MASS
*End Assembly
**
** ELEMENT CONTROLS
**
*Section Controls, name=EC-1, hourglass=RELAX STIFFNESS
1., 1., 1.
**
** MATERIALS
**
*Material, name=Steel
*Density
7850.,
*Elastic
    2.1e+11,  0.3, 273.
 2.0708e+11,  0.3, 323.
 2.0417e+11,  0.3, 373.
 1.9833e+11,  0.3, 473.
  1.925e+11,  0.3, 573.
 1.8666e+11,  0.3, 673.
 1.8083e+11,  0.3, 773.
```

```
   1.75e+11,  0.3, 873.
 1.7143e+11,  0.3, 883.
  1.466e+11,  0.3, 973.
  1.249e+11,  0.3,1073.
  1.094e+11,  0.3,1173.
  1.001e+11,  0.3,1273.
    9.7e+10,  0.3,1373.
*Inelastic Heat Fraction
        0.9,
*Plastic
  3.28e+08,      0.,    273.
 3.353e+08, 0.00102,    273.
 3.503e+08, 0.00498,    273.
 3.606e+08, 0.01019,    273.
 3.743e+08, 0.02039,    273.
 3.858e+08, 0.03011,    273.
 3.947e+08,  0.0401,    273.
  4.02e+08, 0.05026,    273.
 4.087e+08, 0.06003,    273.
 4.145e+08, 0.07018,    273.
```

•

•

•

```
8.203e+06, 0.29811,   1273.
 8.369e+06, 0.39811,   1273.
 8.375e+06, 0.49811,   1273.
 8.294e+06, 0.59811,   1273.
 8.235e+06, 0.68254,   1273.
*Rate Dependent
844., 2.207
*Specific Heat
450.,
**
** INTERACTION PROPERTIES
**
*Surface Interaction, name=Contact
*Friction
0.,
*Surface Behavior, pressure-overclosure=HARD
*Surface Interaction, name="Friction contact"
*Friction
 0.3,
**
** BOUNDARY CONDITIONS
**
** Name: Clamp Type: Symmetry/Antisymmetry/Encastre
*Boundary
Clamp-1.RP_Clamp, ENCASTRE
** Name: Mass Type: Displacement/Rotation
*Boundary
Mass-1.RP_Mass, 1, 1
Mass-1.RP_Mass, 2, 2
Mass-1.RP_Mass, 4, 4
Mass-1.RP_Mass, 5, 5
Mass-1.RP_Mass, 6, 6
** Name: Plate Type: Displacement/Rotation
```

```
*Boundary
"rigid plate-1".RP_Plate, 1, 1
"rigid plate-1".RP_Plate, 2, 2
"rigid plate-1".RP_Plate, 4, 4
"rigid plate-1".RP_Plate, 5, 5
"rigid plate-1".RP_Plate, 6, 6
** Name: base Type: Symmetry/Antisymmetry/Encastre
*Boundary
_PickedSet68, ENCASTRE
**
** PREDEFINED FIELDS
**
** Name: Temp_toptube   Type: Temperature
*Initial Conditions, type=TEMPERATURE
"tube (top)-1".Tube, 293.
** Name: Temperature   Type: Temperature
*Initial Conditions, type=TEMPERATURE
tube-1.Tube, 293.
** Name: Velocity   Type: Velocity
*Initial Conditions, type=VELOCITY
Mass-1.Mass, 1, 0.
Mass-1.Mass, 2, 0.
Mass-1.Mass, 3, 8.
**
** INTERACTIONS
**
** Interaction: Interaction
*Contact, op=NEW
*Contact Inclusions, ALL EXTERIOR
*Contact property assignment
 ,  , Contact
** ----------------------------------------------------------------
**
** STEP: Crush
**
*Step, name=Crush
*Dynamic, Explicit, adiabatic
, 0.1
*Bulk Viscosity
0.06, 1.2
**
** LOADS
**
** Name: Gravity   Type: Gravity
*Dload
, GRAV, 9.81, 0., 0., 1.
**
** OUTPUT REQUESTS
**
*Restart, write, overlay, number interval=100, time marks=NO
**
** FIELD OUTPUT: F-Output-1
**
*Output, field, number interval=100
*Node Output
A, U, V
*Element Output, directions=YES
MISESMAX,
**
** HISTORY OUTPUT: Mass
```

```
**
*Output, history, time interval=5e-05
*Node Output, nset=Mass-1.Mass
A3, U3, V3
**
** HISTORY OUTPUT: Monitor
**
*Node Output, nset=tube-1.Monitor
A3, U3, V3
**
** HISTORY OUTPUT: Monitor_top
**
*Node Output, nset="tube (top)-1".Monitor
A3, U3, V3
**
** HISTORY OUTPUT: Force
**
*Node Output, nset=RP_earth
RF3,
**
** HISTORY OUTPUT: Energy
**
*Output, history, time interval=0.0001
*Energy Output, elset=tube-1.Tube
ALLIE, ALLKE, ALLPD
**
** HISTORY OUTPUT: Energy_top
**
*Energy Output, elset="tube (top)-1".Tube
ALLIE, ALLKE, ALLPD
*End Step
```